# Tutorial on Remote Sensing Using GNSS Bistatic Radar of Opportunity

**VALERY U. ZAVOROTNY**
National Oceanic and Atmospheric Administration,
Boulder, CO 80305 USA

**SCOTT GLEASON**
Southwest Research Institute,
Boulder, CO 80303 USA

**ESTEL CARDELLACH**
ICE-CSIC/IEEC, Barcelona, Spain

**ADRIANO CAMPS**
Universitat Politècnica de Catalunya-Barcelona Tech,
08034, Barcelona, Spain

***Abstract*—In traditional GNSS applications, signals arriving at a receiver's antenna from nearby reflecting surfaces (multipath) interfere with the signals received directly from the satellites which can often result in a reduction of positioning accuracy. About two decades ago researchers produced an idea to use reflected GNSS signals for remote-sensing applications. In this new concept a GNSS transmitter together with a receiver capable of processing GNSS scattered signals of opportunity becomes bistatic radar. By properly processing the scattered signal, this system can be configured either as an altimeter, or a scatterometer allowing us to estimate such characteristics of land or ocean surface as height, roughness, or dielectric properties of the underlying media. From there, using various methods the geophysical parameters can be estimated such as mesoscale ocean topography, ocean surface winds, soil moisture, vegetation, snowpack, and sea ice. Depending on the platform of the GNSS receiver (stationary, airborne, or spaceborne), the capabilities of this technique and specific methods for processing of the reflected signals may vary. In this tutorial, we describe this new remote-sensing technique, discuss some of the interesting results that have been already obtained, and give an overview of current and planned spacecraft missions.

*Digital Object Identifier 10.1109/MGRS.2014.2374220*
*Date of publication: 26 January 2015*

EARTH PHOTO—© STOCKBYTE, SATELLITE IMAGE—UNIVERSITAT POLITÈCNICA DE CATALUNYA—BARCELONA TECH

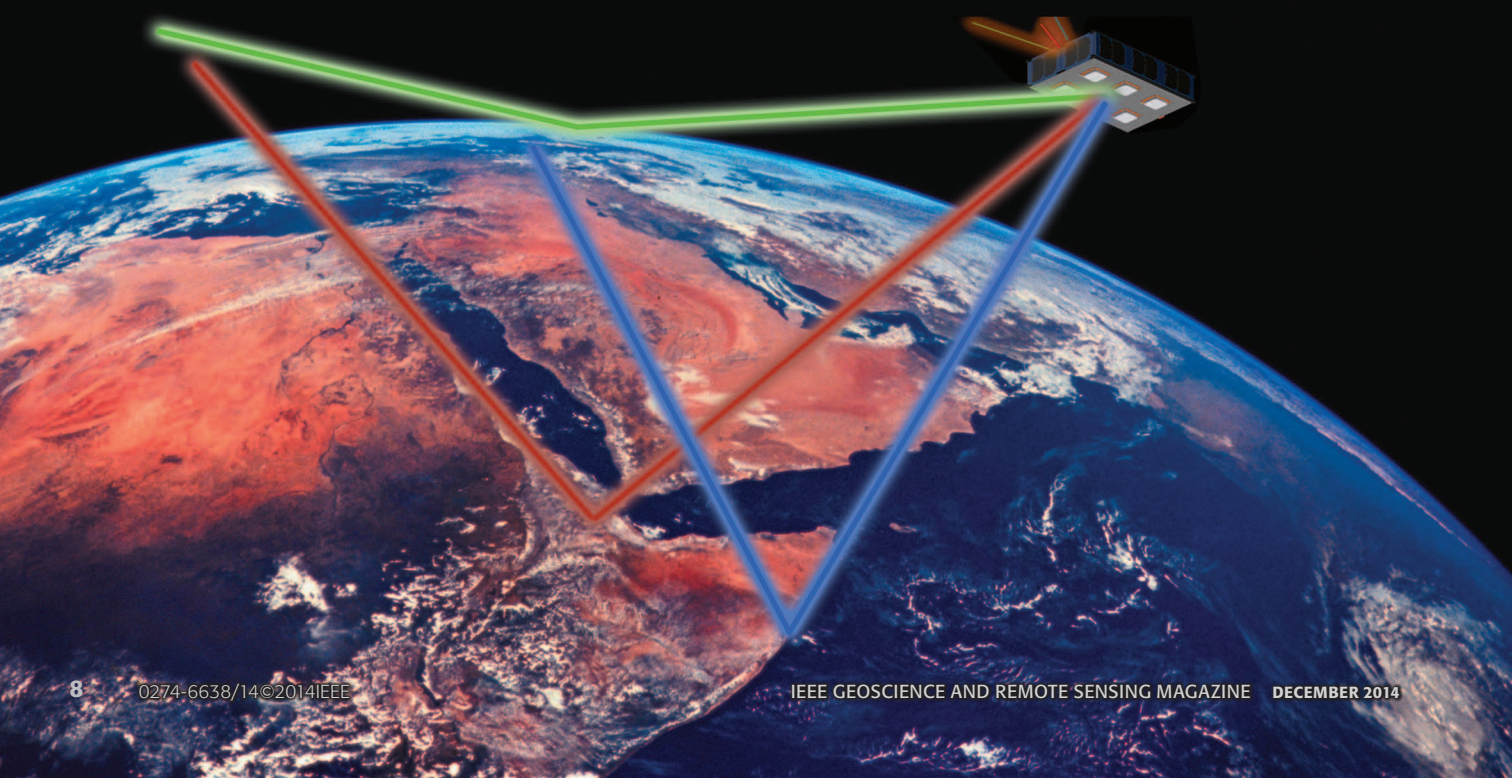

## I. INTRODUCTION

The Global Positioning System (GPS) was created about 25 years ago solely for global navigation purposes. However, soon it became clear that signals from GPS and other Global Navigation Satellite Systems (GNSS) can be used for a large variety of applications, and, particularly, for Earth remote sensing. In late 1980s GNSS signals were proposed for remote sensing of the Earth's atmosphere by performing radio occultation measurements [1, 2]. The first observations and processing of the radio occultation data were performed in a GPS/MET experiment [3, 4]. About the same time, the idea of using GNSS signals reflected off the Earth's surface for scatterometry purposes was discussed by Hall and Cordey [5]. Martin-Neira first proposed to use them for ocean altimetry [6]. It is worth mentioning that a similar approach based on communication signals emitted by satellites and planetary probes was exploited in [7–9]. In 1998, Garrison and Katzberg demonstrated from an aircraft experiment that the GNSS signal reflections can sense ocean surface roughness and related wind [10], [11]. The GNSS signal reflections from a low Earth orbit at very low grazing angles were occasionally observed during radio occultation experiments [12], [13]. The first GNSS signal reflections at steep incidence were serendipitously found in calibration data during the SIR-C radar experiment onboard the U.S. Space Shuttle [14].

Similar to traditional radar remote sensing, the GNSS reflectometry technique can be applied to remote sensing of various types of natural covers, such as ocean, land, ice, snow, vegetation. The GNSS signals reside at frequencies commonly called L-band, which are capable of penetrating cloud cover and are particularly sensitive to soil moisture, sea-ice salinity and snow water content.

The most important difference between the GNSS reflectometer and traditional radar is that the latter represents a monostatic, backscatter sensor, whereas the GNSS reflectometer represents non-cooperative bistatic (or, rather multi-static) radar of opportunity. That means that the non-cooperative transmitter and the receiver are separated by a significant distance. An illustration of the bistatic configuration, with the receiver in a low Earth orbit, is shown in Fig. 1. It can be said that GNSS bistatic radar of opportunity consists, in fact, only of a receiver of a small form-factor while the multiple transmitters are always in the sky and provide continuous illumination signals for free.

Measuring a delay between the direct signal and the reflected one from the Earth's surface and recalculating the temporal delay into the spatial intervals turns GNSS bistatic radar into an altimeter. Conventional radar altimetery is monostatic. It provides altimetric measurement at the spacecraft nadir and only along a single ground track. The GNSS altimeter can perform altitude measurements along multiple widely spaced ground tracks acquiring signals simultaneously from several satellites. Measuring the peak power of the scattered GNSS signal and widening of its waveform and retrieving from these parameters the surface roughness and dielectric properties of the probed media makes GNSS bistatic radar a multi-beam scatterometer.

The constraints of GNSS reflectometry are related to the relatively low power of the signal, and a fixed set of L-band frequencies and bandwidths. Since the transmitted GNSS signals of opportunity are relatively weak, the scattered signal is received only from the area around the nominal specular point on the surface called a glistening zone. The location of this point is predetermined by the relative positions of both the transmitter and the receiver with respect to the Earth's surface. Therefore, it cannot be changed at will as in the case of monostatic mapping radar where scanning beams can create a rather large and continuous swath. On the other hand, specialized monostatic radars are significantly more expensive, massive, require large antennas and high power supply which means large solar panels. So, for the price of one heavy and expensive radar satellite a constellation of small GNSS-R satellites spread over an orbit can be utilized. Such a constellation can compensate for a sparse swath of a single satellite and will increase the global coverage by decreasing the repeat time compared to a single satellite.

Soon after the first trial field experiments, more elaborate aircraft campaigns with GNSS-R bistatic radars measured various geophysical parameters of Earth environment. This includes the retrieval of wind speed and later wind vector above rough seas using reflected signals from multiple GPS satellites [15]–[18]. The retrieval algorithm used a theoretical model in the form of a bistatic radar equation which related the reflected waveforms to mean-square slopes, and from there, to wind speed [19]. A significant body of GPS reflection data obtained with a NASA Langley GPS receiver was collected during multiple flights on the NOAA P-3 "hurricane hunter" aircraft through tropical cyclones [20]–[21]. This enabled building an empirical model which related mean-square slope of waves to wind speed over a large range of wind speeds [22].

Along with scatterometric wind measurements, GNSS-R altimetry was pursued as well. The ability to make altimetry measurements of the reflecting surface has been demonstrated repeatedly during various aircraft campaigns by researchers in the U.S. and Europe (see, e.g., [23]–[29]). Knowledge of the near-surface soil

moisture content also can be inferred from GNSS-R measurements. Promising results were obtained using measurements both from tower and aircraft [30]–[34]. Sea-ice sensing with GNSS-R airborne bistatic radar was shown to be possible [35]–[37].

It was determined that not only the GNSS signals themselves present an opportunity, but also GNSS-R receivers of opportunity exist and can be used for remote sensing. It was found that data obtained from existing networks of ground-based geodetic GNSS instruments at low elevation angles can be used to infer soil moisture, snow depth and vegetation growth from the change in the interference pattern created by multipath propagation [38]–[45]. A similar method of GNSS-R interference pattern can be used with linearly polarized antennas exploiting the high sensitivity of the interference signal to soil moisture at the pseudo-Brewster angle [46].

The first remote-sensing measurements using GNSS signal reflections from space were performed during the UK Disaster Monitoring Constellation mission in 2004. Dozens of GPS reflections have been observed from the UK-DMC satellite [47]. The feasibility of this technique for global ocean, land and ice sensing at spacecraft altitudes was demonstrated in [48]–[51], with a validation of ocean wind sensing from satellites published in [52].

Finally, the technology is rapidly gaining in momentum as demonstrated by the launch of TechDemoSat-1 in July 2014 (which carries a GNSS-R instrument) [53], and with the selection in 2012 by NASA of the eight-satellite constellation Cyclone GNSS (CYGNSS) mission [54]. This development is accompanied by increased activity in Europe with the planned 3Cat-2 and GEROS missions [55]–[57]. All of the current and future GNSS-R missions will be discussed briefly later.

All of this work taken together makes a promising case for the future of this technology, which despite being nearly two decades old is still in need of much further study.

## II. MULTI-STATIC COVERAGE

### A. SUMMARY OF AVAILABLE GNSS SIGNALS FOR REMOTE SENSING

GNSS are constellations of satellites designed to provide position, velocity, and timing information for use on Earth and, to some extent, in space. Currently, the most widely used operational GNSS is the Global Positioning System (GPS). It consists of nominally 24 Medium Earth Orbit (MEO) satellites arranged in six orbital planes with approximately a 12-hour orbital period (even though currently there are more than 24 in operation) [58]. The system was designed and realized by the United States Department of Defense and since being commissioned, the user base of the GPS constellation has expanded in ways that few would have predicted. In addition to its traditional applications, GPS and generally GNSS satellites are now valid alternatives for Earth and atmospheric remote sensing.

In addition to GPS, another GNSS that was fully operational in the recent past is the Russian Federation's GLONASS, which consists of at least 24 MEO satellites in three orbital planes, with an 11-hour and 15-min orbital period. The GLONASS system has made a welcomed comeback in recent years, and in 2011 re-achieved an operational constellation of 24 satellites [58].

Despite the popularity of GPS, many users are interested in alternative systems. Additionally, multiple GNSS provide more available transmission signals which are greatly improving the coverage and revisit times of space-based GNSS remote sensing. The Galileo constellation is the European Union's effort to provide both an alternative and a complement to GPS [58]. It will consist of 30 MEO satellites in three orbital planes, with approximately a 14-hour orbital period. The first Galileo satellite was launched in December 2005, which was followed by the launch of a four-satellite in-orbit validation mini-constellation over the next decade. Full completion of the 30-satellite Galileo system is expected by 2019.

In addition to GPS, GLONASS and Galileo, there are other GNSS currently in development, such as the People's Republic of China's Beidou-2 or COMPASS constellation which is planned to achieve a full satellite constellation operational by 2020. It will consist of 35 satellites: 27 MEO satellites, three inclined geosynchronous orbit satellites, and five geostationary satellites [59]. Japan's proposed Quasi-Zenith Satellite System (QZSS) is a constellation of four Space Based Augmentation System (SBAS) satellites, including three satellites in Tundra orbits and one in a geosynchronous orbit, which will provide additional coverage in the West Pacific region [60]. This is in addition to the existing SBAS systems of WAAS and EGNOS operating over North America and Europe, respectively. Finally, India's Regional Navigation Satellite System (IRNSS) is a system of seven satellites in lower inclination which are intended to provide a navigation capability for the Indian subcontinent, but will also have the potential to be used for remote-sensing applications [61].

### B. GNSS-R COVERAGE AND REVISIT TIME

In theory, all of the above-listed GNSS constellations, as well as numerous other signals of opportunity not discussed in this tutorial (see [62]–[64] for examples of using non-GNSS signals for bistatic remote sensing) can be used for Earth remote sensing. One of the most attractive benefits of GNSS-R is its general simplicity and low-cost passive instrumentation, which enables smaller instruments, smaller satellites, and larger constellations. The actual coverage statistics of the GNSS-R CYGNSS missions has been simulated and is presented below. Additionally, an example of a "future" constellation that utilizes both the GPS and Galileo constellations is shown to demonstrate the impressive coverage and revisit statistics achievable using constellations of GNSS-R remote-sensing satellites. GNSS-R measurements are traditionally taken in "tracks"

or "arcs" across the surface as the bistatic specular reflection points between the GNSS transmitters and receiving satellites move across the surface (imagine the reflection points shown in Fig. 1 tracking out paths as both the receiving satellite and transmitter orbit). Over time these tracks slowly cover large regions of the globe depending on the receiver and transmitter orbits.

Fig. 2 shows an illustration of the coverage and revisit time statistics that eight satellites in 35 degree inclination equatorial orbits (i.e. CYGNSS) can achieve using only four parallel measurements from the GPS constellation only. CYGNSS' primary mission is the study of ocean winds and waves in tropical cyclones (hence, its low inclination orbit). However, in the future it is expected that GNSS-R will be used to sense ocean, land, and ice features globally using larger constellations. Fig. 3 shows a coverage and revisit time simulation for a possible GNSS-R constellation which consists of 24 polar orbiting satellites in three orbit planes, each tracking up to 10 parallel reflections from both the GPS and Galileo constellations. The results clearly demonstrate the coverage potential of GNSS-R, with complete global coverage achieved with an average revisit time of less than two hours globally.

## III. GNSS SIGNAL STRUCTURE

The GPS was the first fully operational Global Navigation Satellite System. Its signal structure was designed to allow multiple transmitters using the same frequency band, and to have a certain tolerance to multipath and jamming, a serious issue for military applications, and increasingly more often to civilian applications as well. It was also conceived to have a low power spectral density to avoid mutual interference with other microwave systems, and to allow the estimation of the ionospheric delay for accurate range determination. These features are achieved by means of spread spectrum techniques. In short, this implies spreading the bandwidth of the navigation signal (a bi-phase modulation with a symbol rate of 50 Hz) by mixing it with a pseudo-random rectangular pulse train that has a much higher frequency than the data. The higher the spreading frequency, the higher the power spectral density decrease for a given total radiated power. The spreading sequences are known as pseudo-random noise (PRN), since they have auto-correlation and cross-correlation properties similar to those of Gaussian noise, but with the advantage that they can be precisely generated and regenerated, since they are in essence deterministic. Each GPS satellite has its own PRN code that not only allows discriminating between transmitters, but also grants the required jamming and multipath resilience, and provides range estimations to determine the user position by triangulation.

To understand the structure and properties of the PRN codes, it is useful to consider first the case of a pure random sequence of pulses of width $\tau_c$ (Fig. 4):

$$P(t) = \sum_{n=-\infty}^{+\infty} x_n \cdot \Pi\left(\frac{t - n \cdot \tau_c}{\tau_c}\right), \quad (1)$$

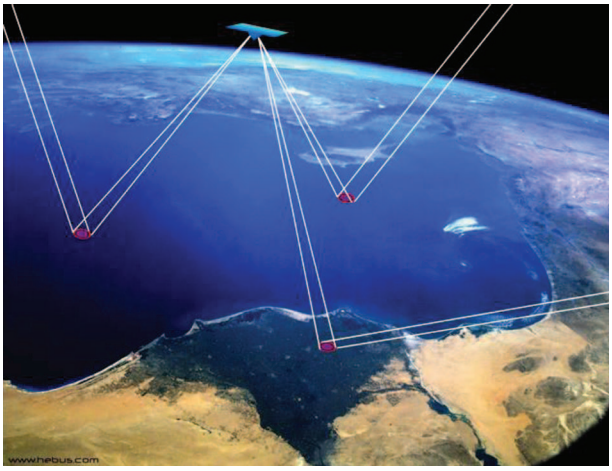


**FIGURE 1.** Depiction of GNSS bistatic remote sensing concept.

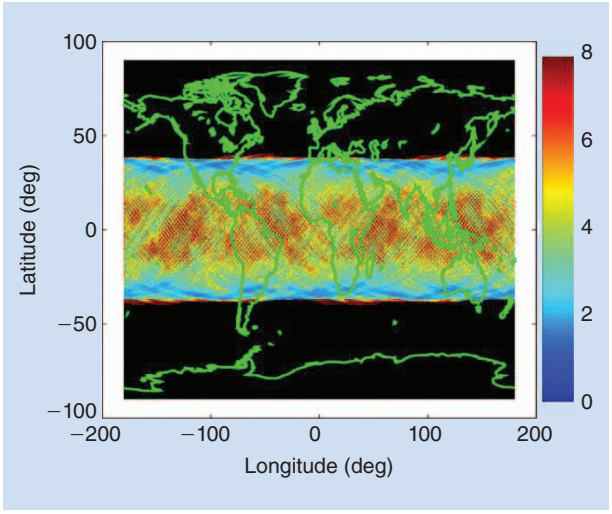


**FIGURE 2.** Simulated coverage and revisit time map for the CYGNSS constellation. Mean revisit time over equatorial regions between approximately ± 38° latitude is approximately five hours.

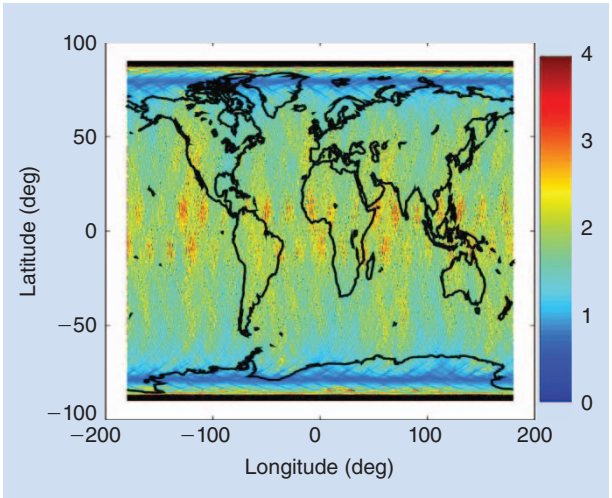


**FIGURE 3.** Simulated coverage and revisit time map for a 24-satellite polar orbiting constellation, with each satellite tracking up to 10 GPS and Galileo measurements. Mean revisit time over entire globe is less than two hours.

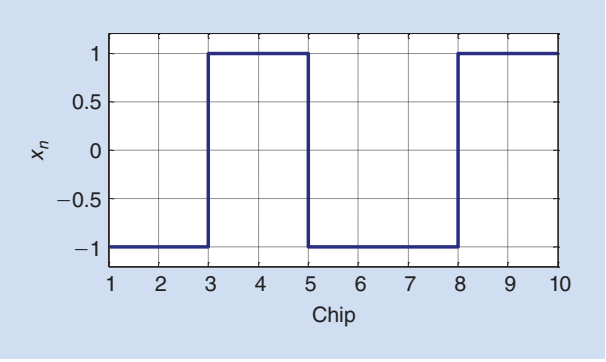


**FIGURE 4.** Sample random sequence of pulses $x_n = \{-1, -1, +1, +1, -1, -1, -1, +1, +1 \ldots\}$. Chip duration $= \tau_c$.

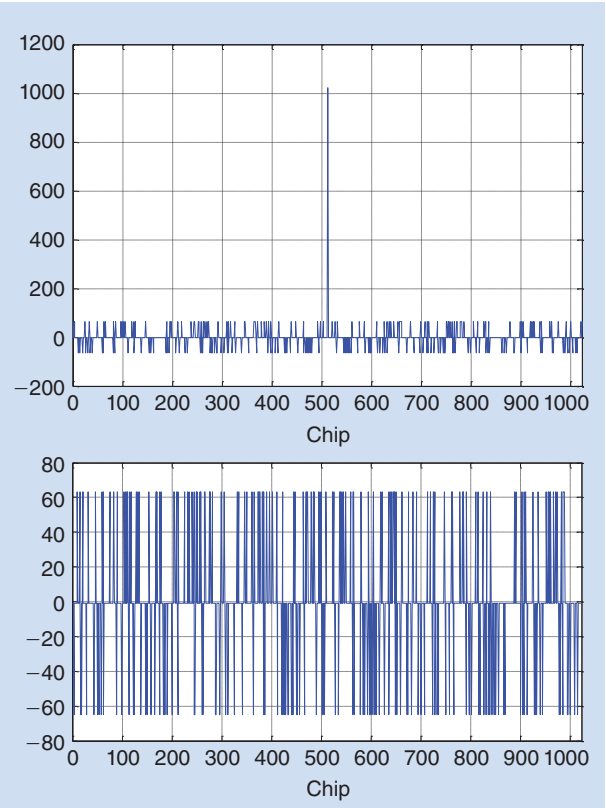


**FIGURE 5.** Auto-correlation of C/A code 1 (top) and cross-correlation of C/A codes 1 and 2 (bottom).

where $x_n$ takes the values ±1 with equal probability.

Each individual pulse that composes the sequence is known as a "chip" in opposition to a "bit", since it does not carry any information. The auto-correlation of $P(t)$ is approximately a triangular function given by:

$$R_p(\tau) \approx \Lambda_{T_c}(\tau) = \begin{cases} 1 - \dfrac{|\tau|}{T_c}, & |\tau| < \tau_c \\ 0, & \text{elsewhere} \end{cases}, \tag{2}$$

where $\tau$ is the time lag. For the L1 C/A code $\tau_c = 0.977$ µs, which corresponds to 293 m. As compared to conventional radar altimeters, this value is too large to ensure a satisfactory range resolution for altimetry applications. Higher signal-to-noise ratios (SNR), and larger bandwidth codes with narrower auto-correlation functions are required. The actual PRN codes cannot be, strictly speaking, random, since it is necessary to regenerate the spreading sequence used by the transmitter at the receiver to decode the navigation signal and retrieve the pseudo-range observable. Therefore, the PRN codes will be deterministic and periodic sequences, but with auto-correlation properties similar to those of a pure random sequence.

The Coarse Acquisition (C/A) codes are used for open-access civil service. They have a period of 1 ms to allow quick signal acquisition, and a length of 1023 chips. This implies a chip rate of 1023 MHz, and a bandwidth of 2.46 MHz. The resulting C/A codes have high autocorrelation peaks to clearly identify an acquired satellite and low cross-correlation peaks so that the signals from different satellites do not interfere between each other (Fig. 5). In order to discriminate a weak signal surrounded by strong ones, it is necessary for the autocorrelation peak of the weak signal to be higher than the cross-correlation peaks of the stronger signals. In an ideal case of using random sequences, the codes would be orthogonal and the cross-correlations zero. The PRN codes used are almost orthogonal, and the cross-correlation values are as low as −65/1.023 (12.5% of the time), −1/1.023 (75% of the time), or 63/1.023 (12.5% of the time).

There is also a precise code (P) used for the restricted military signal. It has a chipping rate ten times faster than the C/A code (10.23 MHz) that results in a tenfold increase of the pseudo-range observable accuracy. The code period is one week, so that the direct acquisition of the code (i.e., the estimation of the code offset) is pretty cumbersome. Therefore, to acquire the P code special data fields of the navigation frames are used (Z-count and Time of Week (TOW)). To increase the code robustness even more it is possible to switch the system operation to use an encrypted version of the P code, noted as P(Y) [65]. The C/A and P codes are modulated in-phase and quadrature on the L1 carrier as shown in (3):

$$\begin{aligned} S_1(t) = &\sqrt{2 \cdot P_{C/A_1}} D(t) \cdot CA(t) \cdot \cos(\omega_1 \cdot t + \phi_1) \\ &+ \sqrt{2 \cdot P_{P_1}} D(t) \cdot P(t) \cdot \sin(\omega_1 \cdot t + \phi_1), \end{aligned} \tag{3}$$

where $S_1(t)$ is the signal transmitted by a given GPS satellite $P_{C/A_1}$ is the transmitted power for the civil signal at L1, and $P_{P_1}$ is the transmitted power for the restricted signal at L1. On L2, for a long time, only the $P$ code was broadcast:

$$S_2(t) = \sqrt{2 \cdot P_{P_2}} \cdot P(t) \cdot \cos(\omega_2 \cdot t + \phi_1). \tag{4}$$

On April 28, 2014, the U.S. Air Force began broadcasting civil navigation (CNAV) messages on the L2C and L5 signals. Prior to that, L2C and L5 provided a default message (Message Type 0) containing no data. The L2 signal began with the launch in 2005 of GPS Block IIR(M). As of June 25, 2014, 13 GPS satellites are broadcasting this signal, and by 2018 all 24 GPS satellites will be broadcasting it.

The LC2 sequence has the same chip rate of the C/A signal, but it is composed of two PRN codes of different length. On one side the moderate length code (CM) is 10230 chips long, repeats every 20 ms, and it is modulated with navigation data. On the other side, the long code (CL) has 767250 chips, repeats every 1.5 s, and has no data modulation. Each code is generated at 511.5 MHz and then multiplexed on a chip-by-chip basis to obtain the composite signal at a rate of 1.023 chips/s. A detailed description can be found in [66].

Navigation information such as ephemeris, almanacs, or corrections and constellation health are conveyed by the 50 Hz bi-phase code $D(t)$. All the bit/chip transitions in the C/A, P, and D codes are synchronous, since they are all driven by the same clock. These various signals are broadcast at L-band, thus suffering low atmospheric and rain attenuations. The carrier frequencies are all multiples of 10.23 MHz: $f_{L1} = 154 \cdot 10.23\,\text{MHz} = 1575.42\,\text{MHz}$; $f_{L2} = 120 \cdot 10.23\,\text{MHz} = 1227.60\,\text{MHz}$; and $f_{L5} = 115 \cdot 10.23\,\text{MHz} = 1176.45\,\text{MHz}$.

The frequency spacing between L1 and L2 allows estimation of the ionospheric delay as:

$$\Delta t_1 = \frac{f_2^2}{f_1^2 - f_2^2} \cdot \delta(\Delta t), \tag{5}$$

where $\Delta t_1$ is the time delay at the frequency L1 due to the ionosphere, $f_1$ and $f_2$ are the L1 and L2 frequencies and $\delta(\Delta t)$ is the measured time difference between frequencies $f_1$ and $f_2$.

The minimum received power for the L1 P signal is on the order of −133 dBm for a 0 dBic right-hand circularly polarized (RHCP) antenna. At L1 the C/A signal is 3 dB higher than the P signal. At L2 the P code is transmitted 3 dB below the L1 P signal. The SNR for the direct signal ranges between 39 dBHz and 52 dBHz, depending on the geometry, the actual transmitted power, and the instrumental and propagation losses [67]. Within the GPS satellite antenna field of view (FOV), the different signal attenuation due to different propagation losses and atmospheric absorption is compensated with the pattern itself of the transmitting antenna. More specifically, the edge of the Earth is 14° off the antenna boresight, and therefore the pattern maximum is located at this angle.

The transmitted signal is RHCP, and so it is immune to the ionospheric Faraday rotation and the receiving antenna does not have to be pointing to the transmitting satellite to avoid polarization mismatch.

The new L5 signal designed for Safety of Life (SoL) applications is broadcast in a radio band reserved exclusively for aviation safety services. It features higher power, larger bandwidth, and an advanced signal design including two in-phase and quadrature multiplexed signals: a navigation data channel and a data-free channel to allow more robust carrier phase tracking. It began in 2010 with GPS Block IIF. As of June 25, 2014, six GPS satellites are broadcasting this signal, and it will be available for all 24 GPS satellites by 2021 [68].

Other satellite navigation systems such as Galileo share the same frequency bands, as illustrated by Fig. 6 (see also [69]). The PRN sequences are not necessarily generated using shift registers, but instead using look-up tables. Also, advanced modulation techniques (Binary Offset Carrier Signals or BOC) are used to increase the achievable accuracy with the same bandwidth [70]. The BOC modulation is the result of multiplying the PRN code with a sub-carrier which is equal to the sign of a sine or a cosine waveform, yielding so-called sine-phased or cosine-phased BOC signals, respectively, as shown in [71]. The BOC signal is commonly referred to as BOC $(m,n)$ where $f_s = m \cdot 1.023\text{MHz}$ MHz and $f_c = n \cdot 1.023\text{MHz}$, and unless indicated in a different way, when talking about BOC signals, it will always be understood as the sine-phased variant. For the sine-phased BOC signals (i.e. L1M, E1B and E1C), the autocorrelation function (ACF) can be expressed as an addition of triangles [72]:

$$R_{\text{BOC}_s(\alpha m,m)}(\tau) = \Lambda_{t_c}(\tau) * \sum_{k=-\alpha+1}^{\alpha-1} (\alpha - |k|)[2 \cdot \delta(\tau - 2k) - \delta(\tau - 2k - 1) - \delta(t - 2k + 1)], \tag{6}$$

where $\alpha = n/m$ is the symbol ratio and $t_c = \tau_c/\alpha$ For the cosine-phased BOC signals (i.e. E1A), the ACF is given by:

$$R_{\text{BOC}_c(\alpha m,m)}(\tau) = \Lambda_{t_c}(\tau) * \sum_{k=-\alpha+1}^{\alpha-1} (\alpha - |k|)[6\delta(\tau - 2k) + \delta(\tau - 2k - 1) + \delta(\tau - 2k + 1) - 4\delta(\tau - 2k - 1/2) - 4\delta(\tau - 2k + 1\backslash 2)]. \tag{7}$$

Finally, the ACF for the E5 signal can be closely approximated using the general expression of a CDBOC modulation:

$$R_1(\tau) = \Lambda_{T_{B12}}(\tau) * \sum_{i=0}^{N_1-1} \sum_{k=0}^{N_2-1} \sum_{i_1=0}^{N_1-1} \sum_{k_1=0}^{N_2-1} (-1)^{i+i_1+k+k_1} \cdot \delta(\tau - (i - i_1)T_{B_1} - (k - k_1)T_{B12}), \tag{8}$$

$$R_2(\tau) = \Lambda_{T_{B12}}(\tau) * \sum_{l=0}^{N_3-1} \sum_{m=0}^{N_4-1} \sum_{l_1=0}^{N_3-1} \sum_{m_1=0}^{N_4-1} \sum_{p=0}^{N_{res}-1} \sum_{p_1=0}^{N_{res}-1} (-1)^{l+l_1+m+m_1} \cdot \delta(\tau - (l - l_1)T_{B_3} - (m - m_1)T_{B34} - (p - p_1)T_{B12}), \tag{9}$$

$$R_{\text{AltBOC}(a\frac{N_1}{2},a)}(\tau) = R_1(\tau) + R_2(\tau), \tag{10}$$

where $T_{B_i} = \tau_c/N_i$, $T_{B_{ij}} = \tau_c/N_i N_j$, and $N_{\text{res}} = N_1 N_2/N_3 N_4$.

Fig. 7 shows the ACF's absolute value for infinite bandwidth signals. As an example, Fig. 7a is the composition of three functions: a triangle of base [−1, +1] C/A code chips (corresponding to the L1 C/A signal), another triangle of base [−0.1, +0.1] C/A code chips (corresponding to the P code), and two side peaks (corresponding to the M code, if available, depending on the satellite).

Table 1 shows the main signal characteristics for the GPS L1 and L5 and for the Galileo E1 and E5 bands. The carrier


**FIGURE 6.** GNSS signal spectra and modulations (from http://www.navipedia.net/index.php/GNSS_signal).

frequency is denoted by $F_c$ and the chipping rate and the BOC sub-carrier frequency are named as $f_c$ and $f_s$, respectively. The bandwidths and the received powers are the ones defined in the GPS Interface Specification (IS) documents [73], and the Galileo Interface Control Document [70], except for the L1M power, for which [74] is used as a reference, and for the E1A power which is assumed to be equally distributed within the E1 band.

These documents describe the minimum received power, and therefore may lead to pessimistic performance

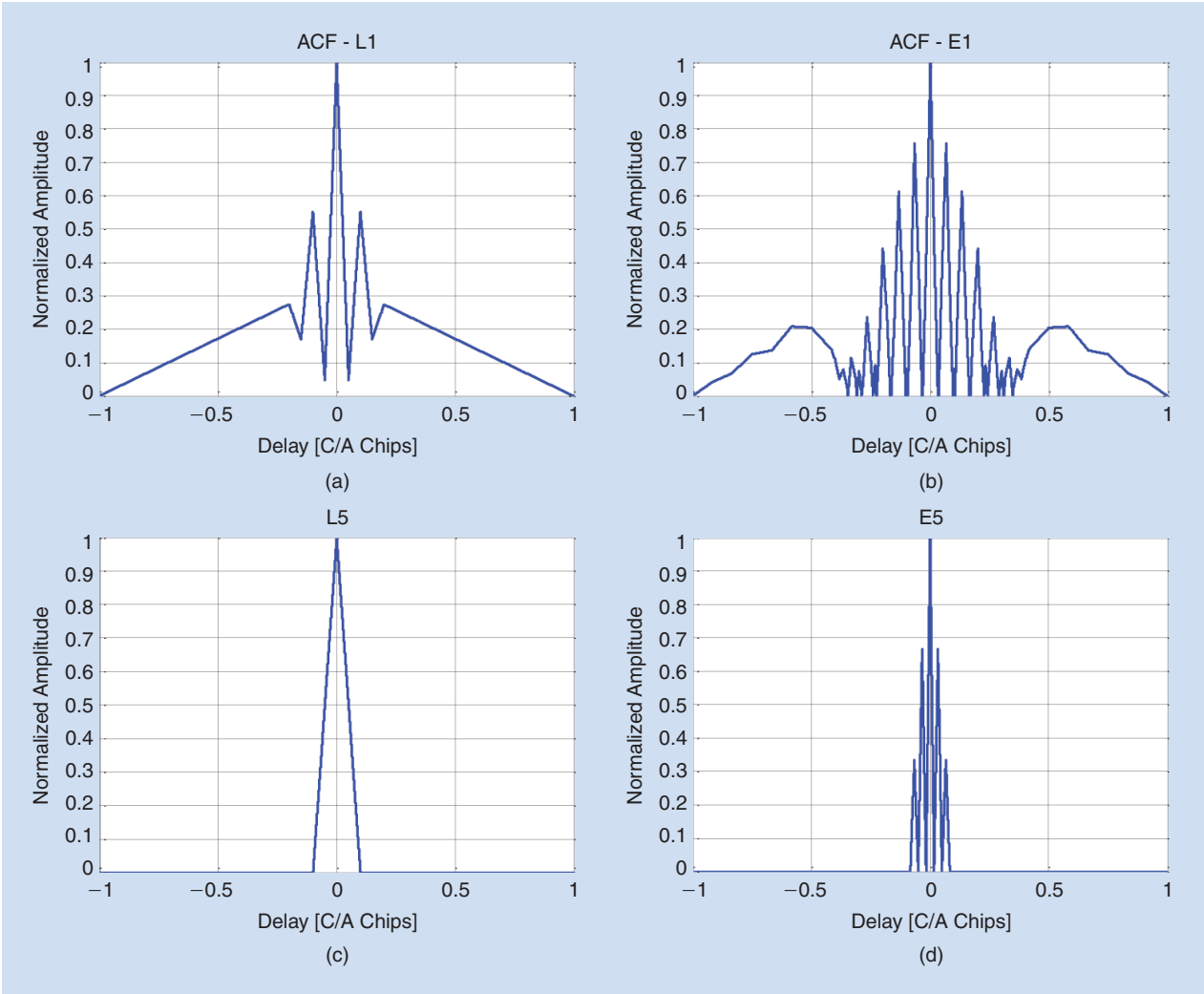


**FIGURE 7.** ACF's absolute value for infinite bandwidth signals (L1, L5, E1 and E5).

estimates. It is known that, actually, typical power values for the GPS signals are about 3 dB higher than the specified minimum.

## IV. BASIC PRINCIPLES

The main product of GNSS bistatic radar is the so-called Delay-Doppler map (DDM) of the scattered signal. In order to obtain the DDM the processing consists of cross-correlating the recorded signal from the down-looking antenna with a replica of the PRN code of the GNSS satellite for a set of different time lags and different carrier frequency offsets (see, e.g. [19, 50, 75]). This procedure is similar to the so-called match-filter signal processing known in conventional radar signal processing. This cross-correlation is obtained over a time interval, called a coherent integration time which should be shorter than the coherence time of the noisy scattered signal. To better explain how bistatic radar deals with such signals we will, for a moment, turn our attention to the surface scattering mechanisms involved, with more details available in [76].

### *A. DIFFUSIVE AND COHERENT SCATTERING*

The GNSS signal illuminating the Earth's surface is relatively weak, so acquiring the scattered signal is a challenge. Because of this, GNSS bistatic radars often only receive the scattered signal from a limited angular zone around the nominal specular direction where the scattered signal is the strongest. The size of this zone depends on the roughness of the surface. Let us assume that the surface extends over many sizes of the first Fresnel zone, and is practically flat and smooth. This means that typical heights $h$ of roughness are much smaller than the wavelength $\lambda$ of the signal. More accurately, accounting for the angle of incidence, $\theta$, we require that the Rayleigh parameter, $2\pi h \cos\theta/\lambda$, will be smaller than 1. Then, we deal with specular, spatially coherent, reflection from a mirror-like surface. In this case, the reflected signal can be treated as a proxy for the direct signal where the complex amplitude should be factored by the Fresnel reflection coefficient. Since the illuminating signal is temporally coherent within the chip duration,

**TABLE 1. GNSS SIGNALS MAIN PARAMETERS [72].**

| GNSS | BAND [MHz] | SERVICE | COMPONENT | MODULATION | $f_c$ [MHz] | $f_s$ [MHz] | POWER [dBW][3,4,6] | MAIN LOBE BANDWIDTH [MHz][7] |
|---|---|---|---|---|---|---|---|---|
| GPS | L1 [1]<br>Fc = 1575.42<br>$BW_1$ = 20.46<br>$BW_2$ = 30.69 | P(Y)[2] | DATA | BPSK-R10 | 10.23 | - | Min: −161.5<br>Typ: −158.5<br>Max: −155.5 | 20.46 |
| | | C/A | DATA | BPSK-R10 | 1.023 | - | Min: −158.5<br>Typ: −155.5<br>Max: −153 | 2.046 |
| | | M[2] | N/A | BOCs(10,5) | 5.115 | 10.23 | Min: −157<br>Typ: −154<br>Max: −150 | 30.69 |
| | L5 [2]<br>Fc = 1176.45<br>BW = 24 | SoL | DATA (L5I) | BPSK-R10 | 10.23 | - | Min: −157.9<br>Typ: −154.9<br>Max: −150 | 20.46 |
| | | | DATA (L5Q) | BPSK-R10 | | | Min: −157.9<br>Typ: −154.9<br>Max: −150 | 20.46 |
| GALILEO [3] | E1<br>Fc = 1575.42<br>BW = 24.552<br>$BW_{assumed}$ = 32 | PRS[2] | DATA (E1A) | BOCc(15,2.5) | 25.575 | 15.345 | Min: −157[5]<br>Typ: −154<br>Max: −150 | 35.805 |
| | | OS,SoL,CS | DATA (E1B) | CBOC(6,1, 1/11) BOCs(1,1) | 1.023 | 1.023 | Min: −157<br>Typ: −154<br>Max: −150 | 4.092 |
| | | | PILOT (E1C) | CBOC(6,1, 1/11) BOCs(6,1) | | 6.138 | | 14.322 |
| | E5<br>Fc = 1191.795<br>BW = 51,15<br>Fca = 1176,45<br>Fcb = 1207,14 | OS | DATA (E5aI)<br>PILOT (E5aQ) | AltBOC(15,10) + Constant Envelope | 10.23 | 15.345 | Min: −155<br>Typ: −152<br>Max: −148 | 51.15 |
| | | OS,SoL,CS | DATA (E5bI)<br>PILOT (E5bQ) | | | | Min: −155<br>Typ: −152<br>Max: −148 | |

[1]IS defined RF bandwidths; [2]Restricted codes; [3]GPS signals: Received minimum RF signal strength on Earth's surface when the Space Vehicle (SV) is above 5-degree user elevation angle with a 3dBi linearly polarized antenna; [4]Galileo signals: Received minimum RF signal strength on Earth's surface when the SV is above 10-degree user elevation angle with an ideally matched and isotropic 0dBi antenna and lossless atmosphere; [5]Equal power distribution assumed; [6]For the GPS signals, the typical value is obtained by increasing the specified minimum by 3dB; [7]for the BOC signals, the bandwidth is defined between the outer nulls of the largest spectral lobes.

the phase of the reflected signal also preserves its coherence. If the roughness heights become comparable to, or larger than the signal's wavelength, diffuse scattering emerges while the specular component disappears. The diffuse scattering is also centered on the nominal specular direction but it comes from an area much larger than the first Fresnel zone. Frequently, this area is called a "glistening" zone.

In the case of wind-driven waves on the sea surface, the diffuse scattering of the GNSS L-band signal is formed by the quasi-specular reflections on curved facets produced by waves. This type of scattering is different from the Bragg resonant scattering typical for a monostatic radar setup. Usually, it is produced by the combined effect of a large number of reflection points within the glistening zone. According to the two-scale (or composite) model, the large-scale (larger than several radio wavelengths) component of the sea surface is responsible for the quasi-specular scattering within the glistening zone. Outside of this region, the quasi-specular scattering decays very fast, yielding to Bragg resonant scattering from a small-scale surface component.

### *B. GNSS-R BISTATIC RADAR EQUATION*

For fully diffuse scattering of the GNSS signal from a rough surface, the following bistatic radar equation holds for the ensemble mean of the correlation power as a function of the time delay and the frequency offset, a.k.a. a delay-Doppler map (DDM) [19]:

$$\langle |Y(\tau,f)|^2 \rangle = \frac{\lambda^2 T_i^2}{(4\pi)^3} P_t G_t \iint \frac{G_r}{R_t^2 R_r^2} \chi^2(\tau,f) \sigma_0 dS, \qquad (11)$$

where:

$T_i$ is the coherent integration time;

$P_t G_t$ is the transmitter's Effective Isotropic Radiated Power;

$G_r$ is the receiver antenna gain pattern;

$R_t$ and $R_r$ are distances between the nominal specular point and the transmitter/ receiver, respectively;

$\chi^2$ is the Woodward Ambiguity Function (WAF), which describes the range and Doppler selectivity of the coherent radar [77];

$\sigma_0$ is the normalized bistatic radar cross section (BRCS) of the rough surface, which gives a portion of the scattered power carried by the outgoing plane wave in a specific

direction, while the unit surface is being illuminated by the unit wave incoming in another direction.

The WAF in (11) can be approximated by the square product of two functions: the triangularly shaped (in the case of GPS L1 signals; see (2)) correlation function $\Lambda(\tau)$ and the sinc-shaped function $S(f)$. The first term determines an equi-range annulus zone, and the second one determines an equi-Doppler-frequency zone. The width of $\Lambda(\tau)$ is determined by two times the PRN chip length, $2\tau_c$, and the width of $S(f)$ is determined by two times the inverse of the coherent integration time, $f_{\mathrm{Dop}} = 2/T_i$. For fixed positions of the transmitter and the receiver, both WAF and BRCS are functions of reference surface coordinates.

In applying this model to new GNSS signals with new modulation schemes such as BOC, it would be necessary to substitute the appropriate delay and Doppler responses for the new signal characteristics. Some of the new characteristics to be found in future GNSS signals were discussed previously in the Section "GNSS Signal Structure."

The normalized bistatic radar cross section (BRCS) $\sigma_0$ describes the strength of the scattered signal originating from a particular point on the rough surface and propagating in the direction of the receiver's antenna. So, in terms of surface coordinates, it describes the glistening zone of the rough surface. In the commonly used geometric-optics limit of the Kirchhoff approximation this term is represented by the following expression [78], [79]:

$$\sigma_0 = \pi |\Re^2| (q/q_z)^4 P(-q_\perp/q_z). \tag{12}$$

Though this value is a function of the scattering vector, $\vec{q}$, for fixed positions of the transmitter and the receiver above a surface, this vector can be expressed as a function of the coordinate $\vec{\rho}$ in the mean surface plane. The value of $\sigma_0$ depends on the complex Fresnel coefficient $\Re$ which in turn depends on the signal polarization state, the complex dielectric constant of the reflecting medium, $\varepsilon$, and the local incidence angle.

Factor $P(\vec{s})$ in (12) is the probability density function (PDF) of the slopes of the large-scale (larger than several radio wavelengths) component of the sea surface which is responsible for the quasi-specular scattering within the glistening zone. Usually, the most probable orientation of surface slopes is parallel to the mean plane, $z = 0$. Then, the PDF has a maximum at $s = 0$, and the bistatic cross-section $\sigma_0$ has a maximum at $\vec{q}_\perp = 0$, i.e., at the nominal specular direction with respect to the mean surface.

There are several limitations associated with the bistatic radar equation in the form presented by (11). First, it is limited to the case of completely diffuse surface scattering; i.e., when the coherent specular component is absent, or can be safely neglected. However, sometimes the coherent component is noticeable, or even dominant in the scattering process. This can be found for forward scattering from calm seas, lakes, relatively flat land, or sea ice characterized by the weak surface roughness (with heights much smaller than the signal wavelength). This situation can be remedied by augmenting (11) with a term describing a coherent reflection. It can be constructed from a product of a mirrored proxy of the direct signal cross-correlation power $|Y_0(\tau,f)|^2$, the absolute value squared of the Fresnel reflection coefficient, and the factor that takes into account the loss of the spatial coherence due to the presence of some relatively weak surface roughness:

$$\langle |Y(\tau,f)|^2 \rangle_{\mathrm{spec}} = |Y_0(\tau,f)|^2 |\Re|^2 \exp(-8\pi^2\sigma_h^2 \cos^2\theta/\lambda^2). \tag{13}$$

This term will describe a sharp peak of the DDM centered at the delay and the frequency offset associated with the nominal specular point on the surface. The same weak surface roughness will be responsible for the rest of the DDM forming a very shallow pedestal described by (11). In most cases, it probably will not be detectible due to thermal noise. The specular component can be incorporated into the bistatic radar equation (placed under the integral) in the form of a so-called coherent BRCS, $\sigma_{\mathrm{coh}}$, added to a diffuse BRCS, $\sigma_0$ (see, for example, [80]). This additional BRCS includes a delta function over spatial coordinates multiplied by the factor that accounts for factors such as a reflection coefficient, antenna pattern and distance. Therefore, the definition of $\sigma_{\mathrm{coh}}$ differs from the diffuse cross section, $\sigma_0$, definition as a characteristic of the scattering object alone.

The factorization of the WAF into a product of a delay-depended $\Lambda$ function and frequency-dependent $S$ function was used in (11). The limitations imposed by it are not obvious. At least, they are of the same nature as in monostatic radar signal processing [77], and to our knowledge, in practice these limitations play no significant role.

Frequently, the bistatic radar equation is used with a BCRS, $\sigma_0$ in the form of the geometric optics limit of the Kirchhoff approximation (12) but it is not a necessary condition. Any other reasonable EM scattering model can be used in (11) for $\sigma_0$.

While (11) describes an ideal ensemble average $\langle |Y(\tau,f)|^2 \rangle$, in practice we deal with an incoherent integration of $|Y(\tau,f)|^2$ over some observation time $T$; i.e., with averaging over a finite number of statistically independent samples. Such limited-sample averaging itself contains residual noise, which might affect our ability to accurately retrieve the ideal average waveform from the measured one.

When a narrow-band GNSS signal is scattered from a rough surface, the carrier phases arriving from individual reflection points sum together in unpredictable ways at the down-looking antenna, resulting in a completely random received phase and amplitude at the receiver. This causes the total received level of $|Y|^2$ to fluctuate over time due to constructive and destructive interference between individual reflections.

This phenomenon is known in traditional remote sensing applications as fading, or speckle noise, and is unavoidable for a diffusely scattering surface and a coherent

illumination. This noise is multiplicative; i.e., it disappears together with the transmitted signal in contrast to an additive thermal noise originating from the observed scene and the receiver. Both the fading signal and the thermal noise are assumed to be uncorrelated, stationary random processes, which obey circular Gaussian statistics, and have different correlation times and different variances, both with zero means.

The analysis shows that the statistics of sample-averaged $\langle |Y|^2 \rangle_N$ obtained by averaging $N$ statistically independent samples can be described by the ensemble average of $\langle |Y|^2 \rangle$, or a mean correlation power, and number $N$, similar to what is derived for traditional monostatic radars [76]. The residual standard deviation of the sample-averaged cross-correlation power $\langle |Y|^2 \rangle_N$ due to speckle noise reduces approximately as $1/\sqrt{N}$.

It is important to know the correlation time $\tau_{cor}$ of the fading signal being received because it determines the choice of the coherent integration time for the matched-filter processing. Choosing a very small coherent integration time $T_i$, will not allow buildup of the correlator output to its full potential, whereas integrating for too long will not be an improvement over incoherent summation of independent samples. Also, knowing $\tau_{cor}$ allows one to estimate number $N$ as $N \approx T/\tau_{cor}$. The correlation time $\tau_{cor}$ can be extracted from complex auto-correlation function $B_Y(\tau) = \langle Y(t) Y^*(t+\tau) \rangle$, or from its power spectrum [81], [82]. A stochastic model for the waveform time series measurements was developed in [82], which was validated by experimental data in [83].

For the case of fast-moving platforms such as aircraft, or satellite, $\tau_{cor}$ can be related to the signal characteristic spatial scale, the correlation radius, $\rho_{cor}$, through the translational velocity of the receiver's platform $v_{rec}: \tau_{cor} = \rho_{cor}/v_{rec}$. The GNSS transmitter motion should also be accounted for. For estimates of $\rho_{cor}$ one can use the van Cittert-Zernike theorem from which it follows that for a spatially incoherent source of size $D$, the scale $\rho_{cor}$ at distance $L$ from the source obeys the classical diffraction formula: $\rho_{cor} \approx \lambda L/D$, where $\lambda$ is the wavelength of the signal's carrier, and D is the scale of the surface footprint associated with the DDM [82].

### C. EM SCATTERING MODELS

The effect of the Earth's surface enters the bistatic radar equation (11) through the normalized bistatic radar cross section (BRCS), $\sigma_0$, which depends on the directions of incoming and outgoing EM waves, and on the properties of the scattering medium. If the diffuse part of the scattering is weak so that the specular reflection prevails, then $\sigma_0$ reduces to the value $\sigma_{coh}$ discussed above. In the opposite case, when $\sigma_{coh}$ can be neglected, one must deal with calculating the diffuse bistatic cross section, $\sigma_0$. The problem of finding $\sigma_0$, due to its complexity, cannot be solved in a general form. If the L-band radiation cannot penetrate the surface (such as for the ocean surface, or bare moist soil), this significantly simplifies the problem. In this case, the BRCS is driven mainly by the surface roughness and by the impedance, or dielectric permittivity of the very top layer of the medium. If radiation penetrates the scattering medium, it might involve volumetric scattering from inhomogeneities, or multiple reflections from the layers inside the medium (as for ice, snowpack, or vegetation canopy). This would significantly complicate the problem of finding the BRCS. Even for the former case of pure surface scattering, calculating the BRCS can be a challenge. This also pertains to regimes of low-grazing angle scattering, or of multiple scattering from a very rough surface.

Here, we limit ourselves to consideration of a much simpler, single-scattering regime. Also, many practical cases allow various simplifying assumptions regarding the surface roughness, so it is possible to determine manageable formulations. There are numerous theoretical models and approaches of that sort in the literature (see, e.g., [84]). We will mention here only the most popular ones. Among them are the Kirchhoff approximation (KA), the Integral Equation Method (IEM), and the Small Slope Approximation (SSA), accompanied by their variants and further approximations [79], [85]–[94]. The difference between them lies in specific limitations applied to wavelength, geometry and parameters describing roughness, so, as a result, some models are more successful than others.

For example, one of the most widely used approaches is the Geometric Optics limit of the Kirchhoff Approximation (KA-GO). It estimates the Kirchhoff diffraction integral by the stationary phase method. Physically, it means that the EM field at the point of reception is determined by contributions from a multitude of specular points distributed over a portion of the rough surface, whereas diffraction effects are neglected. Frequently, this type of scattering is called quasi-specular. The KA-GO works quite well for forward scattering around the nominal specular direction of the linearly polarized and left-hand circularly polarized (LHCP) waves. The difference between the GO and KA approximations in this regime most likely exceeds the accuracy of the KA itself. The GO approximation gives an incorrect prediction for BRCS for out-of-plane scattering, and for the right-hand circular polarization (RHCP). This is due to the fact that for the latter cases, one needs to account for diffraction effects which are neglected in the KA-GO approach.

In principle, the Kirchhoff Approximation accounts for diffraction but only partially because it does not transition into the expression predicted by the small perturbation method for directions away from the nominal specular reflection [88]. This means that it cannot reproduce the Bragg resonant scattering accurately. Let alone, it is still difficult to obtain an analytical solution using the KA without further simplifying assumptions. If the surface slopes are small the Physical Optics approximation of the KA can be used [76]. Some other simplifying ideas are used in alternative formulations of the KA [95], [96]. Overall, the KA (as well as both the GO and PO approximations) is limited to

the cases of large correlation scales and average curvature radii of the surface compared to the radiation wavelength. Also, it works only for incidence well away from grazing.

The early attempt to unify the KA and the small perturbation method, so that both quasi-specular reflections and Bragg scattering are described simultaneously, have been undertaken by the classical two-scale, or composite model [79], [97]. More rigorously, this was done in a set of "advanced" theories which include, among others, the integral equation method [85], the small-slope approximation method [86]–[89], and the reduced local curvature approximation of third order and its versions [90]–[94]. The two-scale method is heuristic by nature. It requires an arbitrary spectral splitting parameter which divides the surface elevation spectrum into two parts: small-scale and large-scale spectral components of roughness. The small-scale component is responsible for the Bragg scattering, whereas the large scales provide a quasi-specular contribution. The dividing wavenumber is established from the comparisons of the model predictions with the measurements [98].

At the same time, the small-scale approximation and similar approaches (like IEM and RLCA3) do not require the dividing wavenumber because it employs the entire elevation spectrum without splitting it on large-scale and small-scale components. It takes into account the above-mentioned diffraction effects. However, similar to the KA-GO approach, it requires the ocean roughness to have small slopes ($< 0.2$–$0.4$).

Since the SSA is a more accurate approximation, it can be used to assess the validity of the KA-GO approximation [99]. There are two approximations of the SSA, the SSA of the 1st order and the more accurate approximation, the SSA of the 2nd order. Practice shows that the SSA of the 1st order, or the SSA1 suffices for calculations of the LHCP BRCS of the L-band signal in the forward-scattering regime. For calculations of the RHCP BRCS and for a wide-angle scattering regime, the more accurate SSA2 is required. The SSA1 gives the expression for the BRCS $\sigma_0$ in the form of a 2D surface integral similar to that obtained in the Kirchhoff approximation but with a more accurate pre-integral factor [87], [88]; generally, the integral cannot be evaluated by the stationary phase method. Some of the above-discussed theoretical models were employed for modeling of the L-band polarimetric bistatic scattering from sea and land surfaces (see, e.g., [100]–[104]).

For the cases when all the above-mentioned analytical methods are not satisfactory, direct numerical simulations are needed. However, for bistatic geometry and wide-spectrum roughness, they might be prohibitively time consuming.

### D. SURFACE MODELS

In most of the models mentioned above, when calculating $\sigma_0$, one needs to make an assumption about the probability distribution of the surface elevations or slopes. Typically, bivariate Gaussian, or normal, distribution is used in the literature for describing the statistics of ocean and land surfaces. The advantage of a Gaussian distribution is that it is fully expressed through the second-order statistical moments of the random field of surface elevations or slopes. In the case of the KA-GO, the BRCS is explicitly expressed through the PDF of surface slopes which, in turn, depends on slope variances along orthogonal axes. The variance of slopes, or mean-square slope (MSS) can be derived from the correlation function $B_h(\vec{\rho})$ of the surface elevations, or equivalently, from its spectrum $\Psi(\vec{\varkappa})$ (which is a Fourier transform of $B_h(\vec{\rho})$) by integrating it over wavenumbers, $\varkappa$, which are smaller than a dividing wavenumber, $\varkappa_*$):

$$\sigma^2_{x,y} = \langle s^2_{x,y} \rangle = \iint\limits_{\varkappa \le \varkappa_*} \varkappa^2_{x,y} \Psi(\vec{\varkappa}) d^2\varkappa, \tag{14}$$

Models such as the IEM, or the SSA employ the full surface spectrum in their formulations directly without retreating to the variances of elevations, or slopes and, therefore, without using the dividing wavenumber.

To describe ocean surface wave spectra, semi-empirical models are frequently used that were designed to explain field observations, particularly, microwave radar data (see, e.g., [105]). Others suggest obtaining sea-surface spectra by solving a wave action balance equation (e.g., [106]). These models describe wind-driven waves in deep water under diverse wave age (often called 'fetch') conditions. For the wind-driven waves, it is convenient to introduce the MSS along wind direction, $\sigma^2_u$, and across it, $\sigma^2_c$. They can be calculated using (14). Under well-developed conditions (i.e. the waves and wind have reached equilibrium), the statistical distribution of surface slopes would connect the wind speed and direction. The stronger the wind, the larger the MSS of slopes. The direction along which the corresponding mean-square slope is maximal indicates the up/down wind direction.

There are situations when wind and waves are not in equilibrium. Such conditions exist in hurricanes where wind and wave propagation directions are not aligned. To our knowledge, there are no analytical spectral models describing hurricane waves, but there are various numerical coupled ocean-atmosphere models for wave fields in hurricanes, (e.g., WAVEWATCH III [107]). However, they are mostly concerned with energy-bearing spatial frequencies at the peak of the wave spectrum, leaving aside smaller scales that contribute significantly to the total MSS of surface waves.

There are some indications that the actual PDF of ocean wave slopes L-band filtered according to (14) does not exactly follow a Gaussian curve at their tails [108]. Accounting for non-Gaussian features in the PDF of surface slopes would require knowledge of third and fourth statistical moments of slopes, skewness, and peakedness, respectively. Unfortunately, in many cases those parameters are not readily available.

The Gaussian statistics is often used to describe the rough soil surface in soil-surface-scattering studies. It is also rather common for these studies to use an exponential

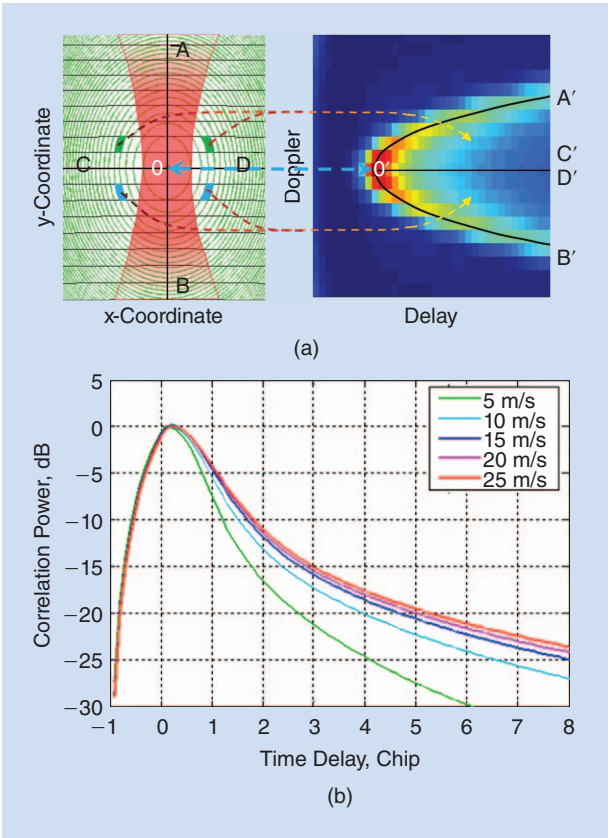


**FIGURE 8.** (a) A concept of delay-Doppler mapping; (b) An example of the 1-D delay waveforms normalized by its peak values for various winds.

correlation function [85]. Such a correlation function is usually associated with "multiscale," or "fractal" surfaces with a wide range of roughness length scales with the smallest ones comparable to, or shorter than, the electromagnetic wavelength. The MSS for such surfaces are often infinite. To regularize this divergence, usually an additional "cutoff wavenumber" parameter is introduced which truncates the surface spectrum at high-frequencies beyond which the contribution to the MSS is neglected [109], [110].

Besides surface roughness, another important parameter enters into analytical scattering models. It is the dielectric permittivity of the lower media such as ocean water, soil, snowpack, or ice. For example, for the KA-GO the dielectric permittivity defines the value of the local Fresnel reflection coefficient, which controls how much energy is reflected back to the upper hemisphere, and how much is transmitted downward into the lower medium. If the lower medium is absorbing (has losses due to conduction and is associated with the imaginary part of the dielectric permittivity), this would limit penetration of the radiation into the lower medium. The penetration depth is an important parameter in soil-surface scattering studies.

There are semi-empirical models for dielectric permittivity for sea water, soil, snow, and sea ice which relate the dielectric permittivity to the temperature and salinity in the case of sea water [111], or to water content and the chemical and physical composition of the medium [112]–[114]. In some cases, the internal structure (layering, or depth profile) within the penetration depth might play an important role in GNSS signal reflection from soil [41] and from snowpack [115].

### *E. THE DELAY-DOPPLER MAP*

From the bistatic radar equation (11), it is seen that the delay-Doppler map emerges as a convolution of the WAF with the BRCS function within the antenna footprint described by its gain pattern. In a sense, delay-Doppler mapping creates an image of the scattering coefficient in the delay-Doppler domain. The WAF is close to unity within an area formed by the annulus zone and the Doppler zone, and tends to zero outside this area. Physically, it means that there are certain contours on the surface for which the scattered signal has the same traveling path length upon arrival to the receiver. Similarly, there are certain surface contours for which the scattered signal acquires the same Doppler frequency shift. Geometrically, the boundaries of annulus zones are formed by the intersection of the equal-delay ellipsoid, formed by GNSS signals, with the Earth's surface. These equi-range lines can be regarded as ellipses if we locally approximate Earth's surface by a plane. The equi-Doppler lines imposed by sinc-function $S(f)$ can be found from the equation

$$\Delta f \equiv f_c \pm \frac{1}{2T_i} = \left[\vec{V}_{\mathrm{TX}} \cdot \vec{m}(\vec{r}) - \vec{V}_{\mathrm{RX}} \cdot \vec{n}(\vec{r})\right]/\lambda, \qquad (15)$$

where $\vec{V}_{\mathrm{TX}}$ and $\vec{V}_{\mathrm{RX}}$ are, accordingly, velocities of the transmitter and the receiver with respect to the Earth's surface. They can be regarded as hyperbolae on the Earth's surface.

At this point, one can notice that the delay-Doppler map created by bistatic GNSS radar has much in common with the delay-Doppler map of unfocused synthetic aperture radar (SAR) [77]. Indeed, in our case, we have the same Doppler frequency/time delay format and pixels formed by the intersection of equi-Doppler and equi-range lines. The differences are that the geometry of these lines is more complex than in the case of SAR due to the bistatic configuration, and that here we have forward bistatic scattering instead of backscattering for SAR.

Fig. 8a depicts an idealized case of the satellite receiver flying at 600-km altitude, in the same plane as the GNSS transmitter, so the equi-Doppler lines (black lines on the left panel) are perpendicular to the AB line, the intersection of the incidence plane with the Earth's surface. The green ellipses are equi-range lines having their common focus at point O. The right panel presents the corresponding DDM which has a characteristic horseshoe shape. Pixels in the surface coordinate domain formed by intersecting equi-range and equi-Doppler lines (on the left) and pixels in the delay-Doppler domain of the DDM (on the right) are connected to each other. The zero-level intensity of the DDM (dark blue area) corresponds to non-intersecting equi-range

and equi-Doppler lines on the left panel. The intensity of every DDM pixel is proportional to scattered power originated from the pair of pixels located symmetrically with respect to line AB. Line AB itself maps into line A′B′ on the right panel, and line COD maps into line O′C′ (or O′D′). One can see that the interior of the DDM is filled with pixels which are a result of scattering from pairs of separated surface pixels. Here we have the so-called ambiguity problem. At the same time, the brightest feature of the DDM lying along the curved line A′O′B′ is formed by the singular pixels aligned along the line AOB without being affected by the ambiguity. Notice that those pixels (shown in pink) become narrower in a radial direction and wider in an azimuthal direction while moving from the center outward. At the same time, the area occupied by those pixels decreases. This explains why the brightness of the DDM decreases while moving from O′ to A′ (or to B′) even when having a uniform scattering coefficient.

Some GNSS reflection receivers are limited to sampling a 1-D waveform which represents a cut of a delay-Doppler map along time delay, $\tau$, while the frequency offset $f$ is fixed and intended to compensate the Doppler shift associated with the nominal specular point on the Earth's surface. An example of the 1-D delay waveform is shown in Fig. 8b. The leading edge of such a waveform, up to the peak value, is produced by the central elliptic annulus zone (filtered by the $S$ function) when it expands from zero to its maximal value. The trailing edge shape of the 1-D waveform is determined by the WAF behavior over time lags, and/or of the BRCS decay along radial directions reflecting the distribution of surface slopes. Therefore, surface roughness affects the shape of the trailing edge and an exact position of the correlation power peak. The trailing edge is more stretched and the peak is more shifted toward later time lags when the surface becomes rougher. In particular, this has implication for accurate GNSS altimetry measurements. The availability of accurate information on surface roughness is important for compensating the bias.

Let us consider in more detail the DDM performance for the case of the satellite-based receiver observing the rough sea surface. As the sea surface roughness changes, the peak of the bistatically reflected power will vary and the shape of the delay-Doppler map will change. In the bistatic scattering case, the relationship between wind speed and peak power detected is the opposite of that of a backscattering geometry. When the wind speed is low, a strong forward reflection results in a very strong received signal. As the wind speed increases, the peak power decreases. See Fig. 9 for an example of a noise-free DDM generated with a 5 m/s wind speed. This DDM was generated using the CYGNSS End-to-End Simulator developed at Ohio State University at an arbitrary spacecraft reflection geometry (500 km altitude, 20 degrees incidence reflection angle, 11 dBi receive antenna gain) with both thermal and speckle noise turned off to allow for better observation of the spreading of the signal in delay and Doppler.

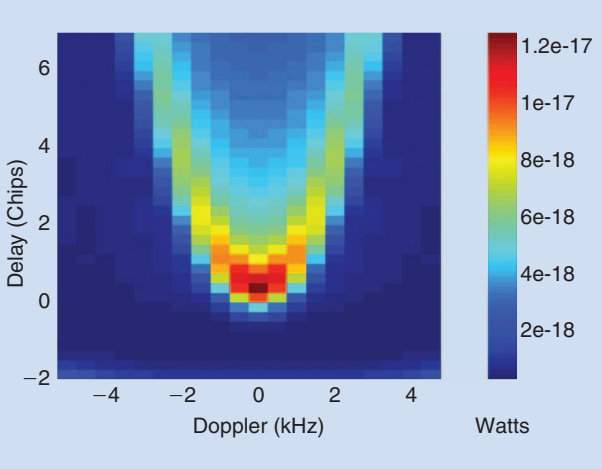


**FIGURE 9.** Example of the noise-free DDM generated using the CYGNSS End to End Simulator (E2ES) under the following conditions: receiver altitude: 500 km, reflection incidence angle: 20°, 11 dBi receiver antenna gain, wind speed: 5 m/s.

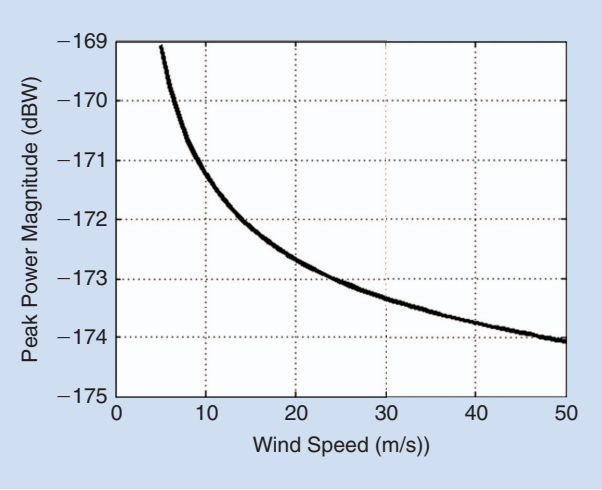


**FIGURE 10.** Changes in DDM peak power as a function of wind speed. Calculated from individual noise-free DDMs generated by the CYGNSS E2ES over a wind range from 5 m/s to 50 m/s.

At this example geometry and constant transmit and receive powers, the signal peak power will fluctuate over a range of approximately 5 dBW from 5 m/s winds to 50 m/s winds (using the wind/wave empirical model based on [21]). The change of the peak as a function of wind speed is illustrated in Fig. 10. In addition to the correlation between the peak power and the sea roughness, there is also information in the leading edge slope. Better than 2 m/s wind-speed retrieval accuracy was achieved from space in [52] using only the magnitude of the estimated scattering cross section, while [116] was able to improve on that result by using both the magnitude and leading edge slope of the signals.

### *F. SPATIAL RESOLUTION*

If the geometry of the problem is such that the Rayleigh parameter of the rough surface is smaller than unity, then the

specular reflection is dominant, and therefore, the spatial resolution of the bistatic GNSS-R radar will be limited to the first Fresnel zone, $l_{Fr} = \sqrt{\lambda R_r}$. For aircraft altitudes of 5 to 10 km, $l_{Fr}$ is several tens of meters. For satellite altitudes of 300 to 600 km, it grows to several hundred meters. That would be a rather good spatial resolution for any radar-type sensor.

Unfortunately, diffuse, quasi-specular scattering is the more frequently occurring process when dealing with natural surfaces. In this case, scattered radio waves arrive from the "glistening" zone, which is much larger than the first Fresnel zone. With the help of the Woodward ambiguity function (see (11)), which acts as a spatial filter, the scattered signal can be transformed into a delay-Doppler map. Ultimately, pixels of that map would determine the spatial resolution of the bistatic GNSS-R radar.

As seen from Fig. 9a, for large time lags, the equi-range zones are getting increasingly closer to each other. So, the pixels created by intersections of those distant equi-range zones with the equi-Doppler lines might seem small. But the power in those small pixels is low (and noisy), and additionally, they are affected by the ambiguity that would significantly diminish the spatial resolution.

In practice, surface pixels which contribute the most to the power of the corresponding DDM pixels have the largest size; so they are most suitable for measurements. They occupy the area near the nominal specular point which corresponds to the maximum in the DDM. The intersection of the first annulus zone with the first Doppler zone creates the pixel with the best spatial resolution. The size of the first annulus zone is proportional to $\sqrt{aR_r}$, where $a$ is the code chip length. The angle of incidence, of course, is also contributing to a more accurate expression for the annulus zone size. It can be found, e.g., in [96]. For 600-km receiver altitude, C/A code, and 1-ms coherent integration time (which determines the size of the Doppler zone), the size of the pixel on the ground will be of the order of 20 to 30 km. For the P(Y), or M code, it will be approximately $\sqrt{10}$ times smaller along the equi-Doppler line. This size would determine the best instantaneous spatial resolution for this configuration.

However, because of the low signal-to-noise ratio, the signal needs to be incoherently accumulated over some time. During that time the receiver and the footprint associated with the considered pixel will move over the surface with a speed of about 2–5 km/s, thus making the resolution lower along the direction of motion. Therefore, finding a resulting spatial resolution would depend on several geometrical, dynamical, and receiver's parameters, with a particular choice of both the coherent and incoherent integration time.

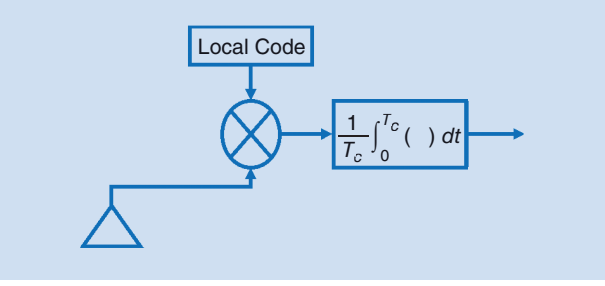


**FIGURE 11.** Basic concept of a conventional GNSS-R instrument.

## V. GNSS-R RECEIVER DATA ACQUISITION TECHNIQUES

As in navigation receivers, the most common GNSS reflectometers' architecture (conventional GNSS-R or "cGNSS-R" in short) correlates coherently during $T_c$ seconds (typically ~1 ms) the reflected signal $s_R(t)$ with a locally generated replica of the transmitted signal $a(t)$ (open C/A codes only) after proper compensation of the Doppler frequency shift $f_d$ or for a number of Doppler frequencies as sketched in Fig. 11 [10]:

$$Y^c(t,\tau,f_d) = \frac{1}{T_c}\int_t^{t+T_C} s_R(t')a^*(t'-\tau)e^{-j2\pi(F_c+f_d)t'}dt', \quad (16)$$

where $t$ is the time when the integration starts. However, since the reflected signal is of even weaker amplitude than the direct one, that is, the signal-to-(thermal) noise ratio is even poorer, and –more important– it usually suffers from speckle noise, a large number of incoherent averages ($N_i$) are required in order to improve the signal-to-noise ratio of $Y^c(t,\tau,f_d)$:

$$\langle |Y^c(\tau,f_d)|^2\rangle \approx \frac{1}{N_i}\sum_{n=1}^{N_i}|Y^c(t_n,\tau,f_d)|^2. \quad (17)$$

As explained in Section III, although the width of the auto-correlation function is not critical for scatterometry applications, for altimetry applications it determines the best achievable time (range) resolution, which, under the assumption of uncorrelated additive white Gaussian noise (AWGN), is given by the Cramer-Rao bound (CRB) [117]:

$$\sigma_\tau^2 \geq \frac{1}{SNR\cdot\beta^2}, \quad (18)$$

where $SNR$ is the signal-to-noise ratio, and $\beta$ is the so-called rms bandwidth, defined as:

$$\beta^2 \triangleq \frac{\int_0^{\min\{B,B_{IS}\}} f^2|S(f)|^2df}{\int_0^B |S(f)|^2df}. \quad (19)$$

In Eq. (19) $B$ and $B_{IS}$ are the baseband bandwidths of the receiver's filter and the transmitted signal according to the Interface Specification documents [70], [73], and $|S(f)|^2$ is its spectrum. Actually, for low SNRs ($< 5$ dB) the Ziv-Zakai bound [117] provides a better indication of the magnitude of the estimation errors, which can be actually much larger than the CRB ones. Therefore, for the same SNR, the larger the rms bandwidth ($\beta$), the better the achievable range resolution.

In principle, one way to overcome the bandwidth limitation is using the so-called interferometric GNSS-R processing [74], or "iGNSS-R", in which the reflected signal is cross-correlated with the direct signal itself $s_D(t)$ after proper Doppler frequency and delay adjustment as sketched in Fig. 12, and formulated in (20) and (21). The ultimate performance of the iGNSS-R will depend not only on $\beta$, but on the SNR (as in (22)), the noise correlation, the width of the tracking window, etc. as discussed in Section VI. However, the value of $\beta$ computed from the waveforms shown in Fig. 15 (top) is $\beta \approx 4.8$ MHz, a much smaller value than the receiver's and the signal's bandwidth, and it will ultimately limit the achievable altimetry resolution improvement by a factor of ~4.8 MHz / 2.2 MHz (rms bandwidth of WF signal with composite signal / bandwidth of C/A code) = 2.18 ($< \sqrt{10}$) [118], [119]. Similar results have been obtained by [120]–[122]. The physical explanation of this result is the smoother shape of the waveform resulting from the convolution of the ACF with the scatterers on the surface, as compared to the ACF itself. The best altimetry performance could only be achieved for quasi-specular reflections, when the WF looks like the ACF.

$$Y^i(t,\tau,f_d) = \frac{1}{T_c}\int_t^{t+T_C} s_R(t')s_D^*(t'-\tau)e^{-j2\pi(F_c+f_d)t'}\,dt', \quad (20)$$

$$\langle |Y^i(\tau,f_d)|^2\rangle \approx \frac{1}{N_i}\sum_{n=1}^{N_i} |Y^i(t_n,\tau,f_d)|^2. \quad (21)$$

The inter-comparison between cGNSS-R and iGNSS-R is not straightforward since there are pros and cons for each method. In cGNSS-R the code replica is generated locally: it allows one to separate signals from different satellites by their code; it inherently has an infinite SNR (small losses can be expected from frequency responses mismatches); smaller size antennas can be employed to track the reflected signals using frequency responses mismatches), and smaller size (directivity) antennas can be used to track the reflected signals. Use of currently available public C/A codes for altimetry is not feasible because of their limited bandwidth which leads to a limited range resolution. Also, the delay and Doppler frequency dynamics for these codes are larger, and these values must be adjusted more frequently for proper operation [123]. In iGNSS-R there is no need to know the code, since the direct signal itself is used instead. It allows not only use of GNSS signals, but satellite radio, satellite television, or any other sources of opportunity with larger transmitted power, larger bandwidth, and better SNR, leading to potentially improved range resolution. In addition, the differential processing produced in the cross-correlation leads to slower delay and Doppler frequency dynamics, which are – in principle– easier to track [123]. The main drawbacks are the large antenna size (directivity) required for the up-looking antenna, even when satellite television signals are used, which leads to the use of beam-steering techniques, and eventually multi-beam antennas if several reflection points are to be tracked, the need to separate different satellites from their signature ("location") in the delay-Doppler map, and the higher susceptibility to radio frequency interference.

To overcome some limitations of the previous techniques, newer approaches have been developed, namely, the reconstructed GNSS-R (rGNSS-R) [124]–[126] and the partial interferometric GNSS-R (piGNSS-R) [127]. The rGNSS-R is similar to the cGNSS-R technique, but semi-codeless techniques are used to reconstruct the P(Y) code which is then correlated with the reflected signal. The piGNSS-R is similar to the iGNSS-R technique, but the P and M codes components of the direct signal are extracted from the reference signal (direct signal) by coherent demodulation, and the interferometric approach is then applied to the reflected signal.

In Fig. 13 (top) the correlation approach used in the down-looking channel (slave: shown) instrument provides P-code processing of encrypted GPS signals without knowledge of the encrypted code, in addition to the C/A code for cGNSS-R, while the up-looking channels (master: not shown) use a similar correlation approach and feed the information to the down-looking channel (slave) [119], [120]. In Fig. 13 (bottom) the direct L1-C/A signal is processed with typical DLLs and PLLs. The locked C/A code model is used to form a L1P model, which is then applied to the direct signal (center left), and after integration over ~0.5 MHz W-chips to estimate their signs, it is combined with the P-code model to form a L1 Y-code model which is used to correlate with the down-looking channel. The advantages of this technique rely mainly on the larger bandwidth of the P(Y) codes, as compared to the C/A ones, and the large SNR, despite the losses of the semi-codeless approach.

Fig. 14 shows the basic approach of the piGNSS-R technique. The advantage of this technique is an even better range resolution as compared to the iGNSS-R one, but at the expense of a 3 dB signal loss (C/A code has been removed), which needs to be compensated by a 3 dB larger antenna directivity.

It is worth mentioning that relative altimetry or scatterometry observations can also be performed by applying the cGNSS-R techniques shown in Fig. 11 to the direct signal as well. This approach is intrinsically more insensitive to errors than absolute measurements performed with the basic scheme shown in Figs. 11 or 12. Alternatively, the

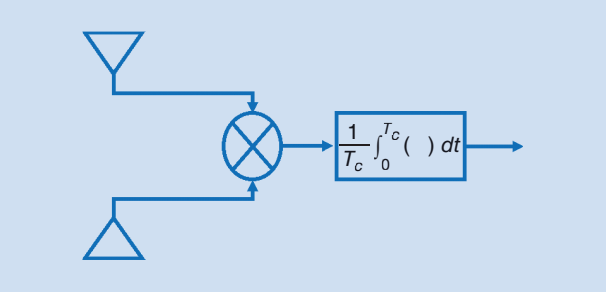


**FIGURE 12.** Basic concept of an interferometric GNSS-R instrument.

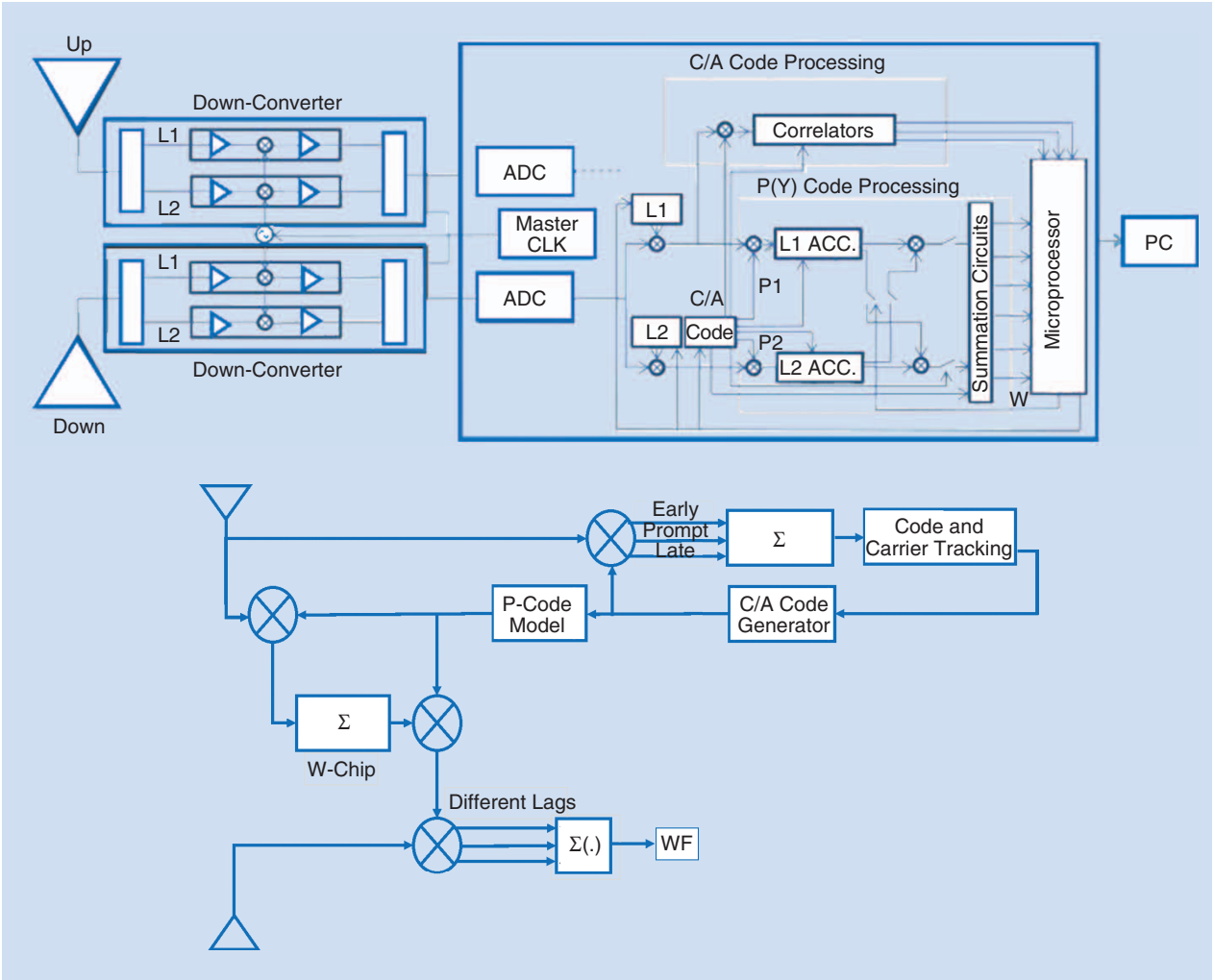


**FIGURE 13.** Basic approaches of the reconstructed GNSS-R technique (adapted from [125], [126]).

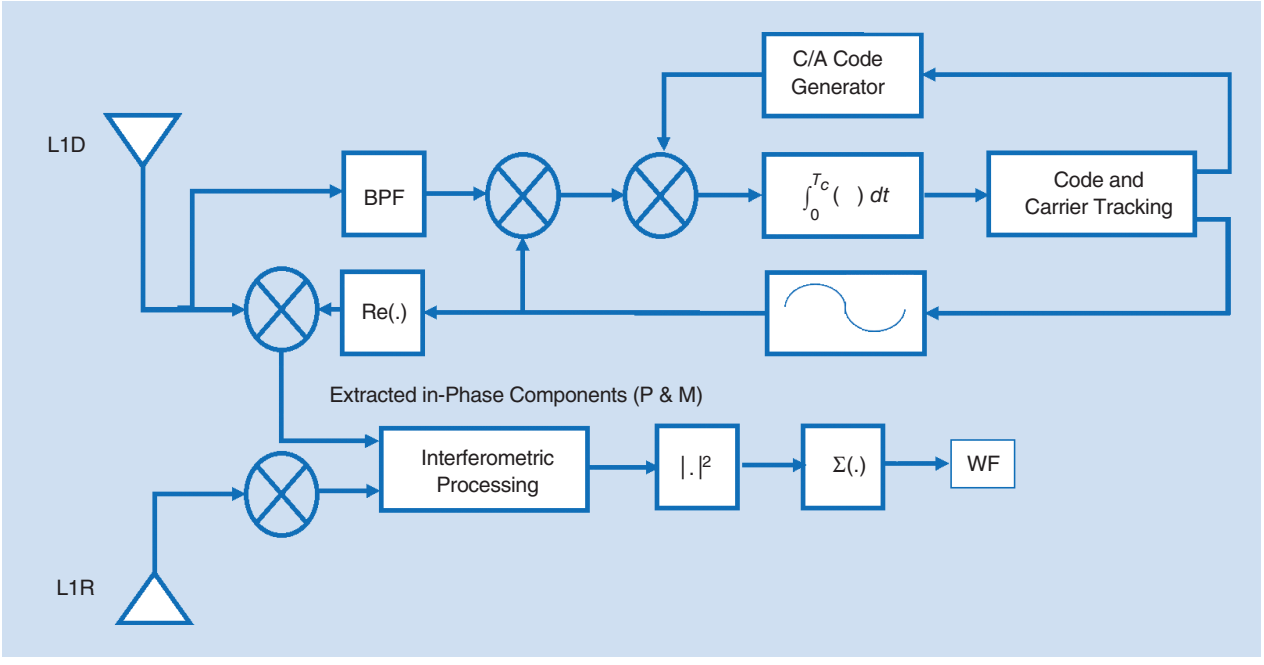


**FIGURE 14.** Basic approach of the partial interferometric GNSS-R technique (adapted from [127]).

second receiving chain can be replaced by a mechanical or electrical beam steering to alternate between the direct and reflected signals.

For static receivers, the fading produced by the constructive/destructive interference between the direct and the reflected signals can also be used to infer geophysical information (Interference Pattern Technique, or IPT), such as soil moisture or vegetation/snow height [46], [128]. For a vertically polarized antenna, the fading disappears at the pseudo-Brewster angle, which depends on the dielectric constant, and the amplitude of the fading fluctuations depends on the magnitude of the reflection coefficient, which depends on the dielectric constant as well. If the relative phase of the fading patterns at vertical and horizontal polarizations is observed, a 90° phase shift occurs at the pseudo-Brewster angle, which is almost insensitive to roughness effects. These applications will be discussed in more detail in Section VII.

Finally, in order to illustrate the relative performance of cGNSS-R and iGNSS-R (and derived techniques), Fig. 15 (from [129]) illustrates the simulated power waveforms for different wind speeds and at $\theta_i = 0°$, normalized to the peak amplitude of the power waveforms for a wind speed of $U_{10} = 3$ m/s, for iGNSS-R (top) and cGNSS-R (bottom). As it can be noted, the scatterometry information is preserved in both techniques (peak amplitude), but the slope of the leading edge of the iGNSS-R waveform is much steeper than that of the cGNSS-R waveform, which should lead to a higher range resolution (depending on the SNR, Section VI).

## VI. THERMAL NOISE, SPECKLE, AND COHERENCE TIME

### A. THE SIMPLIFIED APPROACH

In Section V the altimetry performance was estimated in (18) using the CRB under the assumption of AWGN, and found only to be dependent on the SNR and $\beta$. Also discussed was how to compute $\beta$ for different receiver techniques, and how $\beta$ could be extended beyond the bandwidth of the publicly available codes. The computation of the SNR is now presented. The SNR (thermal noise only) at the input of the correlator is given by:

$$\mathrm{SNR} = \frac{[P_R(\tau, f_d) * |\chi(\tau, f_d)|^2]}{k \cdot T \cdot \min\{B, B_{IS}\}}, \tag{22}$$

where $P_R$ is the total received reflected power, $|\chi|^2$ is the Woodward ambiguity function of the transmitted signal, $k$ is the Boltzmann's constant, $T$ is the equivalent system's noise temperature, and $\min\{B, B_{IS}\}$ is the minimum bandwidth among $B_I$ and $B_{IS}$.

For a cGNSS-R instrument, the *SNR* at correlator's output is also given by (22), but replacing $\min\{B, B_{IS}\}$ by the inverse of the coherent correlation time $(1/T_c)$. For an iGNSS-R instrument, the SNR at correlator's output is given by [74]:

**TABLE 2. PARIS IoD-PREDICTED MINIMUM SNRs (NO SPECKLE) FOR $\theta_I = 0°$ [119].**

| | $\mathrm{SNR}_D$(dB) | $\mathrm{SNR}_R$(dB) | $\mathrm{SNR}_{cr}$(dB) | SNR(dB) |
|---|---|---|---|---|
| L1 | +2.5 | −22.4 | +4.0 | +2.0 |
| L5 | −0.8 | −25.7 | −2.4 | −5.8 |
| E1 | +5.4 | −19.5 | +8.9 | +7.8 |
| E5 | +2.2 | −22.8 | +8.3 | +6.3 |

$$\mathrm{SNR} = \frac{\mathrm{SNR}_{cr}}{1 + \frac{1 + \mathrm{SNR}_R}{\mathrm{SNR}_D}}, \tag{23}$$

where $\mathrm{SNR}_{cr}, \mathrm{SNR}_R$, and $\mathrm{SNR}_D$ are the SNRs of the clean-replica cross-correlation (as in cGNSS-R), reflected and direct signals. If $\mathrm{SNR}_D \gg 1$, then $\mathrm{SNR} \to \mathrm{SNR}_{cr}$, but this requires very large antennas. Table 2 summarizes these values for the PARIS IoD instrument, different bands and signal. It can be noted that for moderate $\mathrm{SNR}_D$ the SNR loss

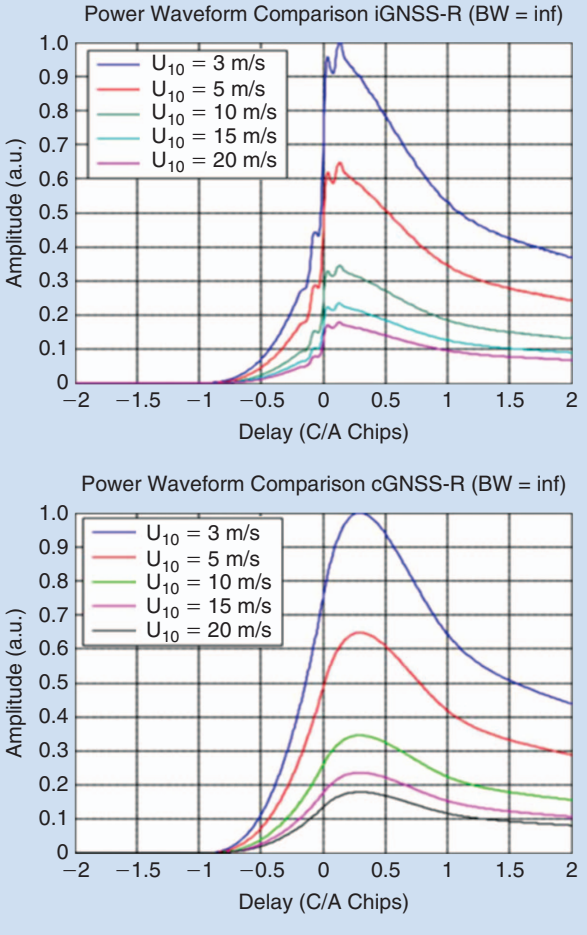


**FIGURE 15.** Normalized power waveforms for different wind speeds normalized to $U_{10} = 3$ m/s, for $h = 700$ km and $\theta_i = 0°$, for iGNSS-R (top) and cGNSS-R (bottom) [131].

as compared to $\mathrm{SNR}_{\mathrm{cr}}$ is $\mathrm{SNR}_{\mathrm{cr}} - \mathrm{SNR} \sim 2$ dB, to be traded off with the increase of $\beta$.

However, the SNR is not only affected by thermal noise, speckle noise can be even dominant. A rough approximation to assess the effect of speckle noise is by adding it to the thermal noise as:

$$\mathrm{NSR}'_{R/\mathrm{cr}} = \mathrm{NSR}_{D/\mathrm{cr}} + \mathrm{NSR}_{\mathrm{speckle}}, \tag{24}$$

where $\mathrm{NSR}_{\mathrm{speckle}} = 1/3.63\,(-5.6\,\mathrm{dB})$, and it is independent on the bandwidth. Finally, the SNR is improved by incoherent averaging as $\sqrt{N_i}$.

### B. THE REALISTIC APPROACH

In Sections V and VI.*A* a crude approximation to the effect of noise was presented. A more precise estimation of the delay is presented here using the Cramér-Rao bound (CRB) including the covariance matrix ($\overline{\overline{C}}$) of the data:

$$\sigma_\tau^2 \geq \frac{1}{\sum_{k,l} \overline{\overline{C}}_{k,l}^{-1} s'(t_k - \tau) s'(t_l - \tau)}, \tag{25}$$

where $s'$ is the waveform's derivative. In the case of AWGN, uncorrelated from sample to sample, (25) reduces to $\sigma_\tau^2 \geq \sigma_n^2 / \Sigma_l \{s'^{(l)}\}^2$, which is equivalent to (18), but in the (discrete) time domain, instead of the frequency domain.

In reality, the ultimate achievable scatterometry or altimetry performance depends on the snap-shot SNR (no incoherent averaging or $N_i = 1$) and bandwidth, and on the cross-correlation of the noise present in consecutive lags $Y^{c,i}(t_n, \tau_m, f_d)$ and $Y^{c,i}(t_n, \tau_{m+1}, f_d)$ (fast time) as well. Additionally, the GNSS-R observable (Eqs. (17) and (21)) was estimated as the average of the square of $N_i$ complex

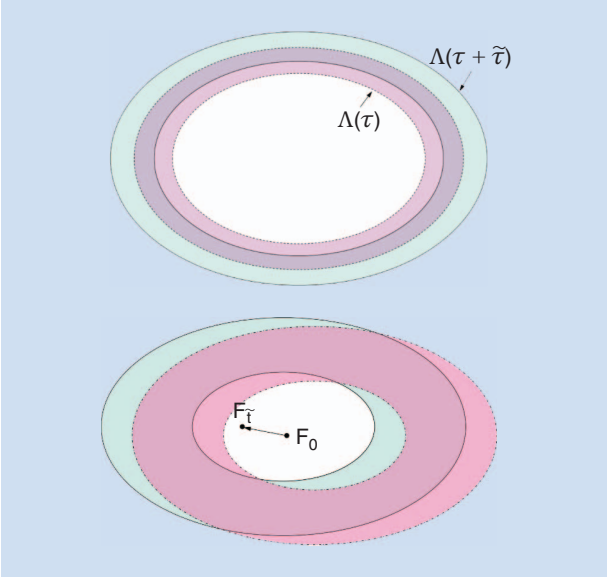


**FIGURE 16.** Physical interpretation of the noise correlation between consecutive lags of the same waveform (top), and between the same waveform lag in consecutive waveforms (bottom) [82].

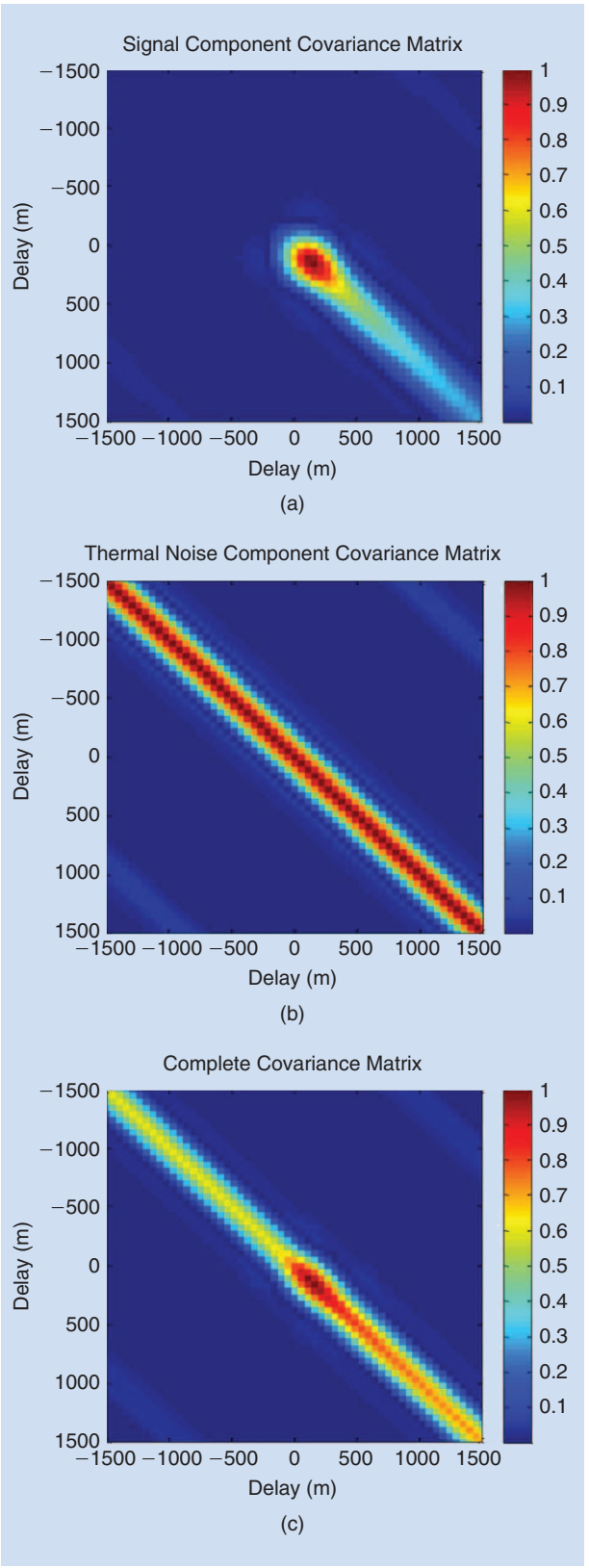


**FIGURE 17.** (a) Signal component covariance matrix (signal statistics). (b) Thermal noise component covariance matrix (noise statistics). (c) Complete covariance matrix (complex cross-correlation statistics, including both signal and noise terms). Simulation parameters: $h = 700$ km, $T_c = 1$ ms, $N_i = 12.000$ (from [131]).

cross-correlations of $Y^c(t,\tau,f_d)$ or $Y^i(t,\tau,f_d)$, as the only way to reduce speckle noise. However, the amount of reduction depends on the correlation between the noise in the same lag $\tau$ in consecutive observables $Y^{c,i}(t_n,\tau,f_d)$ and $Y^{c,i}(t_{n+1},\tau,f_d)$ (slow time). The physical interpretation is presented in Fig. 16.

The analysis of the noise correlation between consecutive lags is performed using the covariance matrices defined as:

$$C(\tau_1,\tau_2)=\left\langle Y^{c,i}(t,\tau_1,f_d=0)\cdot Y^{c,i*}(t,\tau_2,f_d=0)\right\rangle, \qquad (26)$$

which can be understood as the sum of two terms: one corresponding to the signal, and the other one corresponding to the noise. Fig. 17 illustrates this for a spaceborne cGNSS-R instrument. Interested readers are referred to a simulation study for the cGNSS-R case in [130], a detailed analytical study for the cGNSS-R case in [131], and for the iGNSS-R case in [74].

As can be observed from Figs. 17(a) and (b), the noise component is present in all the delays, while clearly this is not the case for the signal term since it is dependent on the backscattered signal. The covariance noise term follows the shape of the auto-correlation function (ACF), and the covariance signal term is dependent on the complex multiplication of the ACF at delays $\tau_1$ and $\tau_2$. This analysis is fundamental to estimate the achievable SNR and the ultimate instrument performance, as well as to specify the instrument in an optimum way in terms of bandwidth [72], sampling frequency, width and central position of the tracking window [129]. In addition, the correlation between consecutive lags is also related to the achievable data compression that can be achieved, for example, using the wavelet transform [118].

Fig. 18 shows consecutive waveforms (cGNSS-R) plotted vs. the correlation lag (x-axis) for up to 1.000 snapshots ($T_i=1$ ms, $N_i=1.000$). As can be observed, the amplitude fluctuations are quite strong, and the correlation between the noise in the same lag $\tau$ in consecutive observables ("bin-to-bin" correlation) limits the effectiveness of the incoherent averaging. The speed of these fluctuations depends on two factors: a) the properties of the surface under observation (i.e., how fast it changes, if it changes at all, for example the ice, the land, or the variable ocean surface under different wind speeds), and b) the relative movement between the transmitter and receiver (i.e., how fast the two coronae move away one from the other).

This effect is better illustrated in Fig. 19, which shows the progress of the waveform estimation using the PIR-A airborne instrument (iGNSS-R) in a field experiment at the Baltic sea on November 11th, 2011. The coherent integration time is $T_i=1$ ms, and the number of incoherent averages increases from 1 up to 10.000. As can be understood, longer integration times are required to achieve a clear waveform due to the higher noise of the interferometric processing. The zoom shows that individual waveforms are formed by the scattering on a few facets only (in particular, the zoom shows one around the specular reflection point), and how the impulse response to that facet is simply the ACF squared (Fig. 7a).

Fig. 20a shows the standard deviation of each correlation lag as a function of the incoherent integration time (as in Fig. 19). It can be recognized that:

a) the standard deviation is higher where the waveform amplitude is higher (speckle noise or "multiplicative" noise), and

b) the standard deviation does not reduce as the squared root of $N_i$, because the corresponding area to the lags associated to higher peaks is smaller and contains fewer scatterers. Before the leading edge, and in the tail, thermal noise dominates and the SNR increases as the square root of $N_i$ (Fig. 20b). This effect can be interpreted as an "effective" number of incoherent averages $N_{i,\text{eff}}$ that depends on the

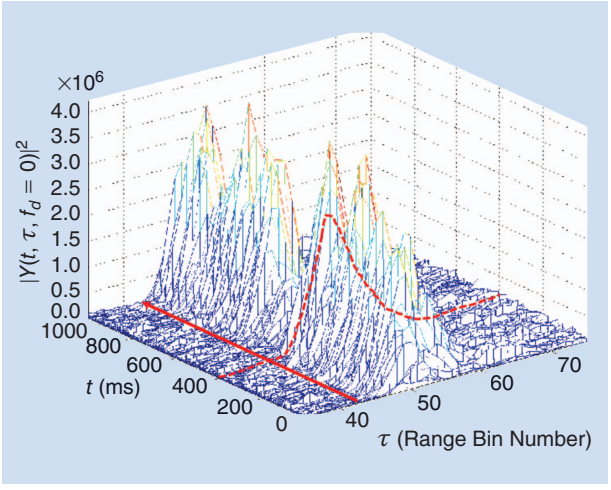


**FIGURE 18.** One thousand consecutive waveforms plotted vs. the fast time (correlation lag: $\tau$) and the slow time ($t$). [118, 131].

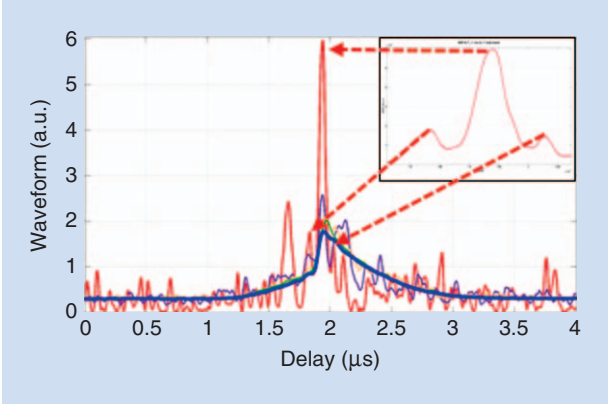


**FIGURE 19.** Sample interferometric waveforms obtained with PIR-A instrument for $T_i=1$ ms, and $N_i=1$ (red), 10 (purple), 100 (orange), 1.000 (green), and 10.000 (blue) waveforms [132]. Zoom for red plot ($N_i=1$) around the main peak compares well with Fig. 7a squared both in the relative amplitude of the side lobes and the location at ±1 P-chips of the main peak.

lag, and that, unfortunately, is smaller where the waveform is larger, where it is carrying the information. Fig. 20c shows the variation of $N_i/N_{i,\mathrm{eff}}$ vs. the lag position for this data set.

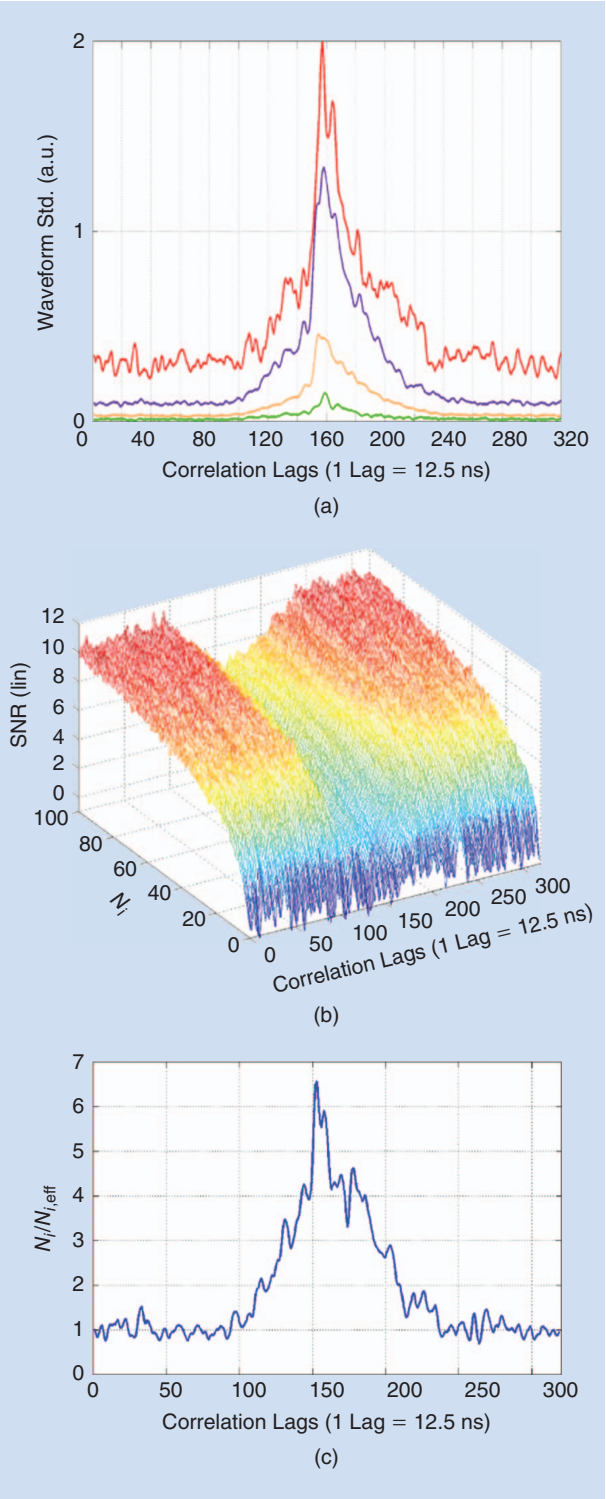


**FIGURE 20.** (a) Standard deviation of each waveform lag as a function of the number of incoherent averages, (b) evolution of the SNR with the number of incoherent averages as a function of the correlation lag, and (c) ratio of the number of incoherent averages and the "effective number" of incoherent averages [132].

This value is actually related to the ratio of the correlation time of the sea surface $\tau_{\mathrm{cor}}$:

$$\tau_{\mathrm{cor}} = \frac{\lambda}{2 \cdot v}\sqrt{\frac{h}{2 \cdot c \cdot \tau_c \cdot \sin(\gamma)}}, \tag{27}$$

and the coherent integration time ($T_i$), which determines roughly the number of consecutive correlated waveforms. In this experiment $\lambda = 0,19$ m, $v = 237$ km/h, $h = 3.000$ m, $\tau_c = 97,7$ ns (P-chips), $\gamma$~70°–77°, and $T_i = 1$ ms, so $\tau_{\mathrm{cor}} = 10,6$ ms, and $\tau_{\mathrm{cor}}/T_i = 10,6$.

Fortunately, for a spaceborne instrument $t_{\mathrm{cor}} = 1$–$2$ ms, and $N_i/N_{i,\mathrm{eff}}$ is much closer to 1, so noise reduction by incoherent averaging becomes more effective.

## VII. APPLICATIONS AND TECHNIQUES

This section compiles a set of remote sensing applications of the GNSS-R technique, some of their retrieval algorithms and performance. Most of these applications have been developed in the last ten years, the ocean altimetric (sea-surface height) and the scatterometric (sea winds and surface roughness) being the first suggested and attempted, more than 15 years ago ([6] and [10], respectively). One can find accounts of various GNSS-R applications in [50], [75], [133], [134].

The section is first organized in five sub-sections, each one devoted to a particular scientific application. For GNSS-R altimetry and ocean scatterometry, several GNSS-R techniques are explained and their performances discussed. Only the basic measurement principles are given for the rest of applications.

Table 3 compiles a summary of the remote sensing applications, and the scenarios from which it is possible to obtain their products. The applications are not fully proven, or those with immature algorithms will not be further detailed, but bibliographical references are provided.

### A. ALTIMETRY

The first application foreseen for GNSS-R was ocean altimetry, that is, determination of the sea-surface height. However, the altimetric measurement principles are quite general and also valid for altimetry over any other surface that can reflect enough power to enable precise observables. For GNSS-R, this is typically ocean and ice.

The product of interest in altimetric applications is the vertical height of the reflecting surface, either in absolute terms (e.g., with respect to the center of the Earth) or in relative terms (e.g., with respect to a given reference surface such as the ellipsoid, geoid, or a well-established spatio-temporal average of the elevation surface). Given that a GNSS-R observation is representative of a certain area over the surface (see Section IV), the GNSS-R measured surface height will be an averaged value across this area.

The way to estimate the vertical component of the surface location is done by measuring it with respect to the receiving system, the position of which must be properly known. The strong point of GNSS-R altimetry is its multi-static capability

that is, being able to solve the surface altitude at each reflection point. This means solving the specular point location using the information from a single GNSS. However, it is well known that the GNSS technique requires at least four GNSS simultaneous radio-link signals to combine their information and properly solve the time-position coordinates of the receiver. Is it feasible to attempt inferring surface height solutions from individual radio links? The answer is yes if both transmitter and receiver positions are known, and good apriori information of the reflecting surface is available. The techniques to precisely position the receiving and transmitting systems are not within the scope of this tutorial, although they also are essentially based on GNSS [50].

Another important aspect to consider is the integration of the GNSS-R observables and their re-tracking: because altimetric measurements require the highest possible SNR, long signal integration times are recommended (the longest possible within the user-required along-track resolution). Before proceeding to integrate the sequential waveforms, they should be re-aligned in time to correct for any possible error introduced by the receiver's open-loop models (for example, intervals for which the receiver does not update the model or it does but in an imprecise way). This procedure is called re-tracking. It must always be based on a deep knowledge of the receiver internal algorithms, and it might change from receiver to receiver. When re-tracking is not properly applied, the integrated waveform blurs, and its leading edge can be significantly distorted (loss of sharpness).

### 1) GROUP-DELAY ALTIMETRIC OBSERVABLES

The observable of interest for altimetric retrievals is the delay of the reflected signal. Delay here can be understood as (1) the time lapse between the transmission of the signal at the GNSS satellite and its reception at the GNSS receiver platform; or (2) the time lapse between the arrival of the reflected radio link and the arrival of the line-of-sight (non-reflected, also called "direct") radio link. In high-altitude receiving systems, it might be more convenient to use the first definition of delay, whereas using the second one has many advantages at lower altitudes. Among the GNSS community it is common to work with ranges or distances rather than the time lapses needed for the signal to travel them. The term "delay" is then used indistinctly for both concepts, and often expressed in units of length (as range/distance).

Regardless of which delay we are interested in, we need to determine the arrival time of the reflected signal. One might be tempted to think that this can be done the same way as a standard GNSS receiver determines the arrival time of the line-of-sight signal, that is, assuming that the signal arrives at the moment corresponding to the peak of its modulation correlation function (for example, peak of the triangle function in most of the currently available GNSS civil signals). As explained in Section IV, the reflection process is likely to deform the correlation function (waveform) because of scattering off surface elements around and even away from the specular point. For rough surfaces such as the ocean, the peak of the waveform is typically shifted from the specular delay caused by the surface roughness [28]. Signals reflected off a roughness-free surface (e.g., very calm waters or smooth sea ice) present a non-distorted correlation function, and the specular delay does correspond to the delay of its peak (as in standard line-of-sight GNSS). On the contrary, signal reflected off a rough surface is strongly distorted, with many contributions from off-specular reflectors, and the peak is delayed with respect to the specular arrival time. Then, the arrival time of the shortest—specular–delay corresponds to some point between the rising of signal power and its peak, an unknown point along the leading edge of the waveform. How can this point be determined?

Several approaches have been suggested. In the pioneering ground-based GNSS-R altimetric experiments, the delay of the peak was used, e.g., [24]. It did work because of the low altitude of the receiver and calm water conditions of the experiments. Subsequently, an alternative approach was suggested for altimetric processing of GNSS-R airborne experiments, consisting of fitting a theoretical model to the waveform, where the delay-shift was one of the parameters of the model, e.g., [26]. This is a suitable approach but it might depend on the goodness of the fit of the model and its potential sea surface roughness residual effects. To overcome this problem, [141] suggested and [142] showed that for an ideal receiver the maximum of the derivative of the waveform's leading edge corresponds to the specular ray-path delay. In a non-ideal receiver, its limited bandwidth filters the signal features and small biases can be introduced. Fig. 21 shows an example for a iGNSS-R type of waveform (see [142] for examples of derivatives of triangular-like correlation functions—cGNSS-R–and [122], [75] for their comparison with iGNSS-R).

The location of the specular ray-path arrival moment within the reflected waveform is not an absolute measure

**TABLE 3. SOME OF THE REMOTE SENSING APPLICATIONS OF GNSS-R AND THEIR FEASIBILITY FOR DIFFERENT RECEIVING SYSTEMS.**

| Application | G | A | S |
|---|---|---|---|
| Ocean altimetry | Y | Y | Y |
| Ocean roughness/scatterometry | Y | Y | Y |
| Ocean water permittivity[1] | U | U | U |
| Soil moisture and vegetation | Y | Y | U |
| Snow | Y | U | U |
| Sea ice | Y | Y | Y |
| Troposphere/ionosphere[1] | N | N | U |

G = ground-based GNSS-R; A = airborne GNSS-R;

S = spaceborne GNSS-R; Y = yes; N = no; U = uncertain

[1]Ocean water permittivity (salinity/temperature) and the atmospheric techniques based on GNSS reflectometry are immature, or not fully proven. Bibliographical references are [135], [136] for GNSS-R ocean water permittivity; [137], [138] for GNSS-R troposphere; and [139], [140] for GNSS-R ionospheric applications.

of its range or delay. It is a measure of the error made by the open-loop receiver when trying to align the reflected signal with the replica (or the reflected signal with the direct one in the iGNSS-R approach). Therefore, the proper delay is the sum of both terms: receiver range model plus location of the specular arrival time within the waveform. As in GNSS positioning and navigation techniques, these measured ranges do not correspond to true distances, because instrumental and environmental effects contribute to the signal propagation delay. For this reason they are called pseudoranges, $\rho$.

### 2) GENERAL ALTIMETRIC INVERSION

The approaches presented in the previous section result in pseudoranges for both the direct and reflected signals, $\rho^{\mathrm{d}}$ and $\rho^{\mathrm{r}}$, respectively. The line-of-sight pseudorange includes the geometric distance $\rho_{\mathrm{g}}^{\mathrm{d}}$, atmosphere-induced delays $\rho_{\mathrm{a}}^{\mathrm{d}}$, receiver and transmitter clock errors, $\rho_{\mathrm{R}}$ and $\rho_{\mathrm{T}}$, respectively, and unmodelled noise $\varepsilon^{\mathrm{d}}$:

$$\rho^{\mathrm{d}} = \rho_{\mathrm{g}}^{\mathrm{d}} + \rho_{\mathrm{a}}^{\mathrm{d}} + \rho_{\mathrm{R}} + \rho_{\mathrm{T}} + \varepsilon^{\mathrm{d}}. \tag{28}$$

The atmosphere-induced delays can be due to the ionosphere and to the troposphere (when the receiver platform is inside the troposphere). These effects will be addressed in Section VII.A.5. On the other hand, the reflected pseudorange includes the geometric reflected distance $\rho_{\mathrm{g}}^{\mathrm{r}}$, the atmosphere-induced delays $\rho_{\mathrm{a}}^{\mathrm{r}}$, receiver and transmitter clock errors, $\rho_{\mathrm{R}}$ and $\rho_{\mathrm{T}}$, respectively, a surface-roughness-induced term $\rho_{\mathrm{rough}}^{\mathrm{r}}$, possible other instrumental biases $\rho_{\mathrm{ins}}^{\mathrm{r}}$ (such as a residual bias due to the receiver bandwidth filtering), and unmodelled noise $\varepsilon^{\mathrm{r}}$:

$$\rho^{\mathrm{r}} = \rho_{\mathrm{g}}^{\mathrm{r}} + \rho_{\mathrm{a}}^{\mathrm{r}} + \rho_{\mathrm{R}} + \rho_{\mathrm{T}} + \rho_{\mathrm{rough}}^{\mathrm{r}} + \rho_{\mathrm{ins}}^{\mathrm{r}} + \varepsilon^{\mathrm{r}}. \tag{29}$$

Fig. 22 illustrates the meaning of some of these terms.

When both direct and reflected measurements have been conducted with the same receiver, or with receivers sharing a synchronous clock, it is advantageous to work with the differential delay to cancel the clock errors:

$$\Delta\rho = \rho^{\mathrm{r}} - \rho^{\mathrm{d}} = (\rho_{\mathrm{g}}^{\mathrm{r}} - \rho_{\mathrm{g}}^{\mathrm{d}}) + (\rho_{\mathrm{a}}^{\mathrm{r}} - \rho_{\mathrm{a}}^{\mathrm{d}}) + \rho_{\mathrm{rough}}^{\mathrm{r}} + \rho_{\mathrm{ins}}^{\mathrm{r}} + \varepsilon^{\mathrm{rd}} \tag{30}$$

Note that if the receiver platform is at low altitude, most of the atmospheric contributions to the delay will be common to both branches, and thus cancel one another out. In this case, only the troposphere below the receiver will contribute to this term. The geometric differential term $\Delta\rho_{\mathrm{g}}$ is a function of the unknown position of the specular point $\vec{S}$, and well-known positions of both the receiver $\vec{R}$ and transmitter $\vec{T}$:

$$\begin{aligned}\Delta\rho_g &= (\rho_g^r - \rho_g^d) = |\vec{S} - \vec{T}| + |\vec{R}' - \vec{S}| - |\vec{R} - \vec{T}| \\ &= |\vec{S} - \vec{T}| + |\vec{R} + \overrightarrow{\rho_{\mathrm{ant}}} - \vec{S}| - |\vec{R} - \vec{T}|,\end{aligned} \tag{31}$$

where $\vec{R}'$ is the location of the down-looking antenna, and $\overrightarrow{\rho_{\mathrm{ant}}}$ is the vector from the line-of-sight antenna phase center to the reflections' antenna phase center. According to Fermat's principle, the specular point has the property of corresponding to the path of shortest time propagation

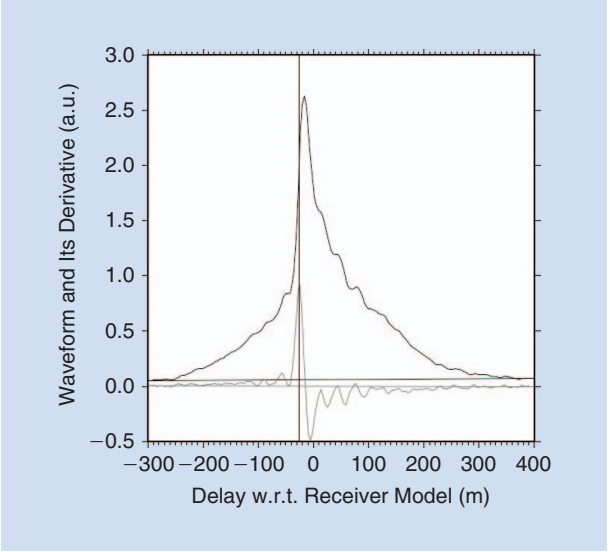


**FIGURE 21.** An example of iGNSS-R waveform (black line) and its derivative (grey line). The delay of the specular ray-path, as given by the peak of the derivative, is indicated by a dashed line. The peak of the waveform is delayed with respect to the specular arrival. Plot uses data from an ESA airborne experiment (information about this experiment can be found in [120], [122]; data available in [143]).

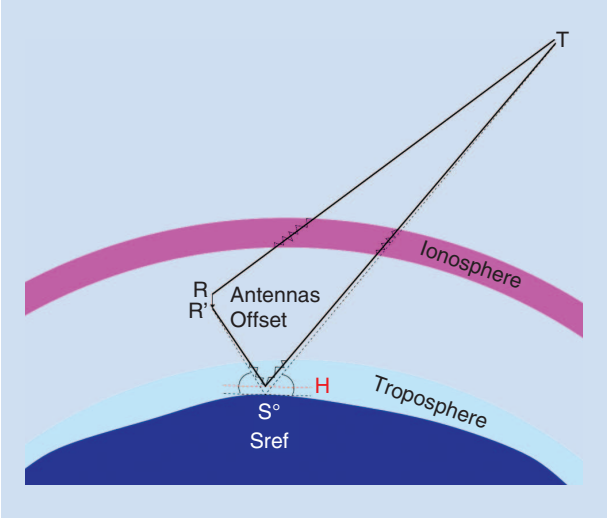


**FIGURE 22.** Non-scaled sketch of the bistatic altimetric geometry and inversion procedure, the pseudoranges involved, and some of their contributions. Ionospheric and tropospheric delays are symbolized as zig-zag lines. A surface reference $S_{\mathrm{ref}}(\mathrm{lon}, \mathrm{lat})$ is used to estimate an apriori location of the specular point $S^0$ (procedure in dashed lines). A correction of the vertical component of $S^0$ is then obtained from the corrected pseudoranges. Clock errors, surface roughness effects, and other instrumental effects are not pictured.

between the transmitter, the surface and the receiver, and its incident angle is equal to the reflected one. Then, with a good apriori knowledge of the Earth surface $S_{\text{ref}}(\text{lon}, \text{lat})$, such as the geoid or the mean sea surface, and both $\vec{R}$ and $\vec{T}$ positions, it is possible to have a good a-priori estimation of the specular point position $S^0$, and we can assume that only a small vertical correction needs to be adjusted: $\vec{S} = F(H; \vec{S^0}, \vec{T}, \vec{R}) = \vec{S^0}(S_{\text{ref}}, \vec{T}, \vec{R}) + H \cdot \hat{u}_v$ ($\hat{u}_v$ being a unitary vector pointing towards the local vertical direction) [75], [144].

Then, solving the bistatic altimetric solution is reduced to finding the vertical correction $H$ such that it better fits the corrected data $\Delta\rho'$:

$$\Delta\rho' = \Delta\rho - (\rho_a^r - \rho_a^d) - \rho_{\text{rough}}^r - \rho_{\text{ins}}^r$$
$$\Delta\rho' = \Delta\rho_g + \epsilon^{\text{rd}} = F\left(H; \vec{S^0}, \vec{T}, \vec{R}, \overrightarrow{\rho_{\text{ant}}}\right) + \epsilon^{\text{rd}} \quad (32)$$

The correction terms $\rho_a^r, \rho_a^d, \rho_{\text{rough}}^r$, and $\rho_{\text{ins}}^r$ are briefly commented on in Section VII.A.4), while $\epsilon^{\text{rd}}$ is unmodelled noise and residual errors.

### 3) FLAT EARTH APPROXIMATION ALTIMETRIC INVERSION

When the receiver platform is at a relatively low altitude above the surface, it is possible to assume that the Earth is locally flat. The altitude to which this condition holds depends on the incidence angle of the observation and the tolerance of the user to the errors this might induce. Fig. 23 shows the errors made in the vertical component of the specular point location when assuming a flat Earth, with respect to assuming a spherical Earth. Only incidence angles in up to 50° (down to 40° elevation) have been included; beyond these angles the error increases quickly. The horizontal errors are slightly larger (16% at 50° incidence, and increasing to more than 500% at an 80° incidence angle).

Under this assumption, the differential geometric term $\Delta\rho_g$ can be simplified to a function of the elevation angle of observation:

$$\Delta\rho_g = 2A\sin(e) - \rho_{\text{ant}}, \quad (33)$$

where $A$ is the altitude of the receiver above the reflecting surface. Because the precise positioning of the receiver is usually made with an up-looking antenna, here we assume that $A$ is the altitude of this antenna above the reflecting surface. The height of the surface with respect to a reference surface (ellipsoid, geoid, or other topographic models) can then be obtained with precise knowledge of the receiver's position: $H = R_v - A$ ($R_v$ being the vertical distance between the reference surface and the receiver). Note that $\rho_{\text{ant}}$ is not the antenna's offset vector itself, but its projection into the direction from where the signal reaches the receiver, $-\hat{k}_s = -\vec{k_s}/|\vec{k_s}|$ ($\vec{k_s}$ being the scattering wavenumber vector). Then, $\rho_{\text{ant}} = \overrightarrow{\rho_{ant}} \cdot (-\hat{k}_s)$. These concepts are illustrated in Fig. 24.

Equation (31) then can be directly inverted into

$$A = \frac{\Delta\rho' + \rho_{\text{ant}}}{2\sin(e)} + \epsilon. \quad (34)$$

### 4) PHASE-DELAY ALTIMETRY MEASUREMENTS

In precise GNSS positioning techniques, the accurate but not very precise group-delay pseudorange observables are complemented with the phase-delay ones, of much better precision but inaccurate. The phase-delay observables are very precise measures of range variations. If both transmitter and receiver were in static positions, the electromagnetic field would oscillate at the transmitted carrier frequency, as $\omega \cdot t$. This is usually fully or partially compensated in the receiving system (down-conversion to baseband or intermediate band). In transmitter and receiver static conditions, the phase term determined by $\vec{k} \cdot \vec{r}$ (being $\vec{k}$ and $\vec{r}$ propagation wavenumber and range vectors) does not change. However, as either/both the transmitter or/and receiver move, this term determines the phase at which the down-converted field is received: $\phi(t) = \phi(t_0) + e^{i\vec{k}\vec{\Delta r}(t)}(\vec{\Delta r}$ being the variation in $\vec{r}$ after $t_0$). This phase can also be expressed as a pseudorange $\rho_\phi(t) = (\lambda/2\pi)\phi(t)$. Note that this observable is very precise: for each full cycle variation of the phase, the pseudorange observable only changes one $\lambda$ (~20 cm in GNSS L-band frequencies). This information would be very valuable in GNSS-R altimetry, but unfortunately most of the GNSS-R observations correspond to diffuse scattering, in which the phase shifts and jumps randomly, impeding its use as range-change tracker. The exceptions are:

- very calm waters (it eventually might happen, not as a general case, but e.g., over lakes, ponds, harbors [23], [25], [145]);

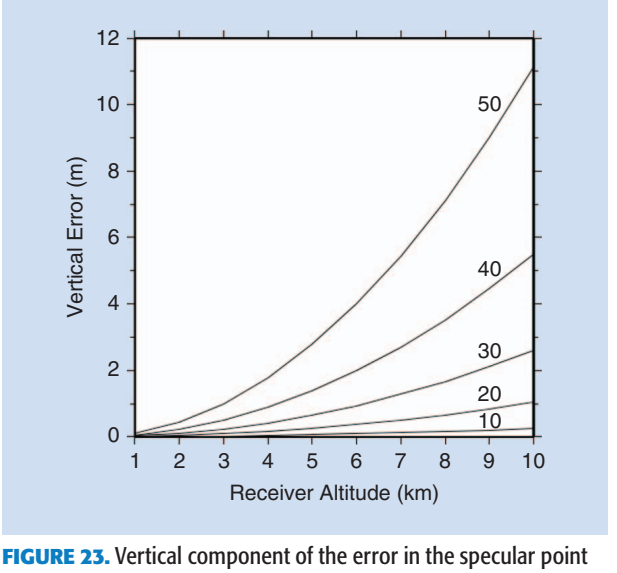


**FIGURE 23.** Vertical component of the error in the specular point location due to the assumption of local flat Earth, for different receiver altitudes (x-axis) and incidence angles (different curves).

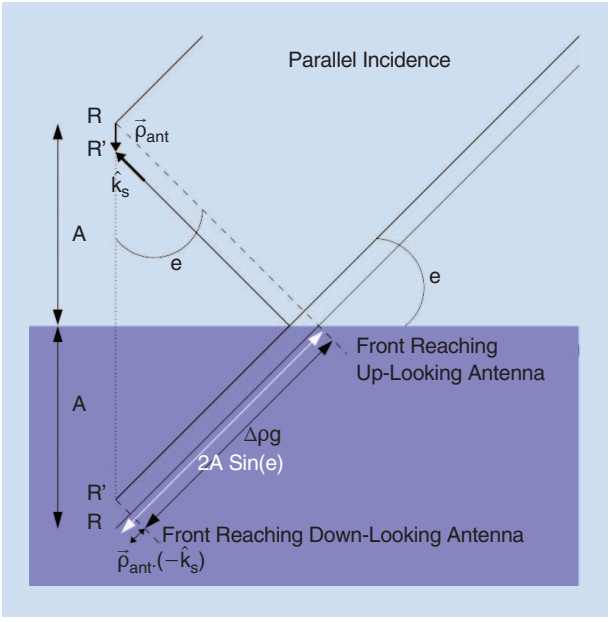


**FIGURE 24.** In low-altitude receiver scenarios, it is possible to assume a locally flat Earth and parallel incidence. Then, the geometrical range difference $\Delta\rho_s$ between the electromagnetic front reaching the down-looking antenna (reflected signal) and the front reaching the up-looking one (direct signal) is twice the altitude $A$ of the receiver $R$ above the surface, multiplied by the sine of the elevation angle, $e$.

- low elevation angles of observation (the effective roughness decreases with increasing incidence angle, e.g., [144], [146]);
- some sea-ice types [147], [148];
- sheltered waters and snow surfaces at very low receiver altitudes (ground-based stations, e.g., [39], [149]–[151].

In these latter cases the line-of-sight and reflected signals have a short relative delay, thus interfering with each other. The receiver then captures the interferometric patterns. These patterns are used to extract several parameters, among them the altimetric one. Details of this Interferometric Pattern Technique (IPT), also called Multipath Reflectometry (GNSS-MR) are given in Section VII.F. It should not be confused with the interferometric GNSS-R (iGNSS-R) technique explained in Section V.

In [146] it was demonstrated that scattering of GNSS over open sea waters at standard ocean-roughness conditions (not calm waters) and captured from a dynamic airborne platform presented sufficient signal coherence properties to enable phase-delay observations. This work also showed that this holds for elevation angles of observation below and up to approximately 30° elevation. Next, we present one of the algorithms that can be used for obtaining the phase-delay observables and infer from them the altimetric solution.

The in-phase and quadrature components of received fields permit one to define the complex reflected $E^r$ and direct $E^d$ fields. The argument of $I = E^r E^{d*}$ is

$$\arg\{I\} = \Delta\phi = \frac{2\pi}{\lambda}\Delta\rho_\phi, \tag{35}$$

where, $\Delta\rho_\phi$ has the same terms as in (30), plus a constant term $K$ that accounts for the unknown ranges of both direct and reflected signals at $t_0$:

$$\Delta\rho_\phi(t) = \Delta\rho_g(t) + (\rho_a^r - \rho_a^d)(t) + \rho^r_{\text{rough}}(t) + \rho^r_{\text{ins}}(t) + K + \epsilon(t). \tag{36}$$

This equation holds if the receiver has applied the same dynamic models to both line-of-sight and reflected signals; otherwise the phase shift must be compensated.

Note that it is possible to "stop" the phase of by counter-rotating it with a good model of $\Delta\rho_\phi$, including the geometric range and the delay-corrections,

$$\Delta\rho_\phi^{\text{mod}} = F(A, \text{atmosphere}, \text{roughness}, \ldots). \tag{37}$$

That is,

$$\arg\left\{I(t)\cdot e^{-\text{ik}\cdot\Delta\rho_\phi^{\text{mod}}(t)}\right\} = \text{const}. \tag{38}$$

The altimetric solution, thus, is the surface height $H$ (or receiver altitude $A$) such that "stops" the phase of $I$ field. Note that this approach does not require to "anchoring" the phase-delay observable (i.e., to explicitly solve for the $K$ term in (36)).

For static receivers at low altitude (ground-based platforms), when the flat-Earth assumption can be used, the evolution of these observables is only due to the movement of the GNSS transmitter, which gradually changes the elevation angle. Then, (34) applies. If the model $\Delta\rho_\phi^{\text{mod}}$ perfectly matches the real data, the signal is fully stopped and its derivative becomes zero; otherwise, the derivative is a measure of the error made in the model. Assuming that the rest of the terms are properly modeled and the error is only due to the surface level, then the derivative is a direct measure of this error:

$$\Delta A = \frac{1}{2}\frac{d\Delta\rho_{\phi-\text{not}-\text{fully}-\text{stopped}}}{d\sin(e)} + \epsilon. \tag{39}$$

### 5) SYSTEMATIC EFFECTS AND CORRECTIONS

As they propagate through the atmosphere, radio- and microwave signals experience extra delay relative to the propagation through a vacuum, and they can also curve their path because of the gradients in the refractive index, $n$ [152]. Given that the refractive index of the atmosphere mostly changes with altitude (vertical gradients), the more slant the propagation path, the more impact of the gradients and bending. The delay induced with respect to the vacuum propagation is given by

$$\rho_{\text{atm}} = \int N\cdot 10^{-6} dl, \tag{40}$$

where $N$ is called refractivity, defined as $N = 10^6(n-1)$. The refractivity of the neutral atmosphere (neglecting liquid water content) is a function of the partial pressures of dry air and water vapor, the temperature, and the compressibility

factors of these gases (e.g., [153], [154]). Note that for reflected signals, the integral along the ray in (35) includes the ray trajectory from the transmitter to the specular point, and from the specular point to the receiver.

Monostatic radar altimeter missions use microwave radiometers aboard the same platform to determine the tropospheric delay over the measurement area. This approach is complicated for spaceborne bistatic altimetric measurements because of their wide range of areas that should be monitored (very wide swath). Solutions are being investigated in the frame of ESA's PARIS-IoD and GEROS-ISS missions.

In GNSS-R at lower receiver platforms, for which experimental data exist, the differential delay cancels most of the atmospheric contribution, including the ionospheric one. Only the effect coming from the troposphere below the receiver needs to be corrected. Sometimes the GNSS receiving system is able to use direct signals to determine the zenith delay ($ZD$). $ZD$ is the atmospheric delay that would be induced in a zenith observation from a receiver at a given altitude $H$ $ZD(H) = \int_H^\infty N \cdot 10^{-6} dh$, and it can be estimated by combining information from different GNSS line-of-sight observations. The $ZD$ at the receiver's altitude does not solve for the tropospheric effect below the receiver, which is the one that does not cancel out in differential GNSS-R and needs to be corrected. A simple exponential model can then be used to extrapolate from the relatively low receiver altitude down to the reflecting surface. In [148] it is suggested that

$$ZD(h) = ZD(0)e^{-h/h_{\text{scale}}}, \tag{41}$$

where $h_{\text{scale}}$ is the vertical extent of the troposphere. If the GNSS-R observation were at the nadir, and the GNSS receiver could estimate $ZD(H_r)$, then the remaining tropospheric delay in the differential observable $\Delta\rho$ (line of sight propagation subtracted) would be

$$\begin{aligned}\rho_{\text{tropo}}^{\text{nadir}} &= 2 \cdot (ZD(0) - ZD(H_r)) \\ &= 2 \cdot D(H_r)(e^{H_r/h_{\text{scale}}} - 1).\end{aligned} \tag{42}$$

Generally, the observations are not at nadir, therefore the equation above needs to be corrected with global mapping functions, $m$. This is an approximation used in Very Long Baseline Interferometry (VLBI) and GNSS geodesy, for which the tropospheric delay at a given elevation $e$ is a function of the zenith delay: $\rho_{\text{tropo}}(e) = m(e, \text{lon}, \text{lat}, \text{time}) \cdot ZD$. These global mapping functions depend on the elevation angle, the geo-location and time [155]. A more rigorous development of these terms separates the hydrostatic from the wet component of the tropospheric delay (and their corresponding mapping functions). The hydrostatic one is a result of the induced dipole moment, and it has a typical value of approximately 2.3 meters at sea level. The wet component is associated with the atmospheric water vapor, it is due to the permanent dipole moment of the molecules of water vapor, and has smaller values (0–0.3 m) but larger variability in time and space.

Equation (40) includes the ionospheric effect. This effect is usually separated from the tropospheric one because of the dispersive nature of the ionospheric plasma. Then, the combination of the observables at different GNSS transmitted frequencies are used to either mitigate or to isolate the ionospheric effect. The ionospheric delay for a given carrier frequency $f$ is proportional to the integrated electron density along the propagation path, $I$, and the inverse square of the frequency [156]: $\rho_{\text{iono}}(f) \propto I/f^2$ (the first-order approximation). The ionospheric effect, even in standard GNSS applications, is one of the effects that is more difficult to model accurately.

The ionospheric-free combination is one that eliminates (or highly mitigates) its effects:

$$\rho_{\text{iono-free}} = \frac{f_1^2 \rho_1 - f_2^2 \rho_2}{f_1^2 - f_2^2}, \tag{43}$$

where $\rho_{i=1,2}$ are the observables as measured at $f_{i=1,2}$. The disadvantage of using a linear combination of observables is that the noise of the combination increases.

Other systematic effects are those induced by the surface roughness and the instrument itself, currently under investigation. The electromagnetic bias (offset introduced because of non-Gaussian surface elevation distribution within the measurement zone) is now being modeled and assessed [157], [158]. While on the instrumental side, the bandwidth effect has been inspected in simulated data for the PARIS IoD instrumental configuration [132].

#### 6) ALTIMETRIC PERFORMANCES

Table 4 compiles the precision achieved in GNSS-R experiments using both group-delay and phase-delay techniques. The table compiles data from [75] and [159].

Various studies based on theoretical models have analyzed the expected altimetric performance of the In Orbit Demonstrator for PARIS iGNSS-R spaceborne altimeter [74]. The resulting expected precision corresponding to observations at nadir and integrated for 100 km along the track are 13 cm, 17 cm, and 16 cm at GPS L1 band [74], [122], and [132], respectively. In [132] other bands are also investigated resulting in an expected precession in 30 cm at GPS L5, 13 cm, and 8 cm at GALILEO E1 and E5, respectively, for observations at nadir and integrated for 100 km along the track.

### *B. WINDS AND WAVES*

The use of GNSS reflected signals as wind scatterometers was first suggested in [10]. In fact, both GNSS reflectometry and wind scatterometers measure surface roughness, not wind speed directly, and it is generally assumed that surface roughness is more closely correlated with the wind stress on the sea surface rather than with wind speed measured at some altitude above the ocean surface (typically at 10 m). Many ocean applications require the wind stress, while meteorological applications often prefer the effective wind at a certain altitude. The relationship between both parameters, linked to the drag coefficient, is currently the

**TABLE 4. GROUP-DELAY AND PHASE-DELAY ALTIMETRIC PERFORMANCE AS OBTAINED IN GNSS-R EXPERIMENTS SORTED BY THEIR RECEIVERS' ALTITUDE. ADAPTED AND EXTENDED FROM [75], [159].**

| DATA-ACQUISITION TECHNIQUE | RECEIVER ALTITUDE (m) | DYNAMIC OR STATIC PLATFORM | REFLECTING SURFACE | EQUIVALENT 1-SECOND NSS ALTIMETRIC PRECISION (m) | REFERENCE |
|---|---|---|---|---|---|
| **GROUP-DELAY ALTIMETRY** | | | | | |
| cGNSS-R C/A code | 4.76 | static | ocean | 0.45 | [160] |
| | 20 | static | estuary | 7 | [24] |
| | 65 | static | pond | 0.08 | [160] |
| | ~330 | airborne | ocean | 1 | [161] |
| | 1000 | airborne | ocean | 1.5 | [29] |
| | 3000 | airborne | ocean | 1.4 | [142] |
| | 3000 | airborne | ocean | 1.2 | [122] |
| cGNSS-R P(Y) code | 1500–3000 | airborne | ocean | 1.7 | [26] |
| iGNSS-R | 18 | static | estuary | 0.08 | [160] |
| | 3000 | airborne | ocean | 0.58 | [122] |
| rGNSS-R | 4.76 | static | ocean | 0.2 | [160] |
| | 65 | static | pond | 0.04 | |
| | 1500–3000 | airborne | ocean | N/A, SNR better than iGNSS-R | [126] |
| **PHASE-DELAY ALTIMETRY** | | | | | |
| cGNSS-R | 8 | static | pond | 0.003 | [25] |
| | 480 | static | lake | 0.02 | [23] |
| | 700 | static | ocean | 0.5 | [163] |
| | 700 | static | ice | 0.6 | [148] |
| | 1000 | static | lake | 0.02 | [145] |
| | 35000 | airborne | ocean | > = 0.8 (elevation dependent) | [164], [146] |
| | 400 km | LEO | ice | 0.1 (slant eflections, in radio-occultation geometry) | [144] |

focus of intense research activity (e.g., there is a dedicated working group within the Ocean Vector Wind Science Team—OVWST [165], [166]).

The selection of microwave bands for wind scatterometers is based on their sensitivity to the wind-generated capillary-gravity waves on the sea surface. The sensitivity increases as the wavelength of the microwave approaches the wavelength of the wind-generated ripples, amplified by resonance effects. Unlike dedicated wind radar-scatterometers, the wavelength of the carrier signal cannot be selected in GNSS-R: it is given by the GNSS transmitters. The GNSS L-band signals have electromagnetic carrier wavelengths longer than the fine surface ripples generated by instantaneous winds. In principle, only surface features of typical length longer than the electromagnetic carrier wavelength can be sensed, meaning that L-band signals have less optimal frequency for wind monitoring compared to typical scatterometric Ku-, or C-bands. At the same time L-band signals are not significantly attenuated by rain, so this makes them invaluable for wind monitoring in tropical cyclones.

As the wind blows, it transfers energy to the ocean, increasing the waves' height and length, changing their spectra and surface slopes' statistics. This is used in some studies to adjust or calibrate the apparent ocean surface slopes at L-band, in the form of a modified relationship between the variance of the slopes and the wind (see (3) in [21]), and valid for a wide range of wind speeds. Some other studies present the L-band roughness parameter as a product by itself (e.g. [167], [168]), although it is not the oceanographic standard one.

The advantage of taking this approach is its complementarity to wind information, because the L-band-filtered variance of the surface slopes (mean square slopes, MSS) strongly depends on the stage of development of the sea. This opens potential inversion schemes, closer to data- assimilation approaches, in which independent wind information could be combined with GNSS-R observations of the L-band roughness to infer information about wave age or dragging-related parameters. The L-band roughness parameters might also be suitable sea-surface descriptors to provide roughness corrections to L-band radiometric missions for improving their sea-surface salinity measurements. The L-band radiometric measurements of the surface salinity have a major systematic effect given by the surface roughness, in particular, to the portion of the spectrum to which L-band signals are sensitive. There is a set of promising studies along these lines, such as [169]–[172].

### 1) RETRIEVAL ALGORITHMS

Several algorithms have been implemented to extract ocean surface roughness and wind state from the GNSS-R

observables. Brief summaries of the algorithms and techniques are compiled below, together with their range of applicability. Only the main principles behind each of the techniques are presented, and bibliographic references are given to the source documents. Some of them are shown in Fig. 25.

### *(A) FITTING THEORETICAL MODELS*

After renormalizing and realigning the delay-waveform, the best fit against a theoretical model gives an estimate for the geophysical and instrumental-correction parameters. As seen in Section IV, the geophysical parameters typically are the 10-meter altitude wind speed, or isotropic sea-surface slopes' variance (mean square slopes–MSS). Some of the work done with this methodology include: (e.g., [17], [18], [20], [167], [173]). The fit also can be constrained to the trailing edge of the waveform, as suggested in [19], and implemented in [17]. This technique works best for airborne altitudes and is not feasible for ground-based receivers because the effect of waveform spreading due to roughness is diminished for low altitudes.

It can be extended to a multi-satellite common inversion using several GNSS reflections arriving from close areas characterized by the same surface roughness state. This approach estimates wind direction (or roughness anisotropy) with 180° residual ambiguity. It was suggested and tested in airborne campaigns in [16], [18]. It is rather straightforward for the case of a single airborne platform, when different satellite reflections arrive to the receiver from relatively close surface areas with the presumably same surface roughness state. For spaceborne receiving systems, this method would lose spatial resolution because the trailing edge of the reflected waveform originates from a very large glistening zone. Instead, one can look into the change of the peak power as suggested in [52]. The CYGNSS mission baseline retrieval algorithms will be mainly based on this approach [116]. In order to estimate wave anisotropy (wind direction) from space a multi-satellite constellation would be required to invert simultaneously (or close in time) several GNSS reflections assuming they all sense the same surface roughness at different angles.

Alternatively, a possibility for obtaining wave anisotropy information from a single GNSS reflection observation by using the Doppler domain of the signal, that is, the delay-Doppler map, was discussed in [168], [49]. Then, the applicability extends to spaceborne systems (in addition to airborne scenarios).

### *(B) DDM METRICS*

The sea-surface roughness information can also be obtained from the "size" of the waveform. The "size" can be defined in different ways, such as the extension of its delay and/or Doppler spread, or its area and/or volume within a given threshold. These techniques can be applied from airborne and spaceborne platforms, but they lose sensitivity at low altitudes.

A stochastic theory that results in two algorithms to retrieve surface winds was developed in [174]. They relate the sea roughness conditions to both the Doppler spread and the delay spread of the reflected signals. For example, the bandwidth at 3-dB level of the cumulative Doppler values is proportional to the roughness MSS and the elevation angle:

$$B_{3dB} \propto \mathrm{MSS}\sin(e). \tag{44}$$

The volume under the normalized or calibrated DDM, or the area under the normalized waveform up to a predetermined threshold change depending on the surface roughness. This hypothesis was first suggested and tested in simulated data by [169] and experimentally confirmed in [172]. This approach might be valuable for potential use of GNSS-R observations in support of oceanic L-band radiometric missions, such as SMOS [175].

Recently, more elaborate DDM metrics have been proposed to retrieve ocean wind speed [176] and wind vector [177] from GNSS-R experiments onboard a high-altitude jet aircraft. The wind-speed retrieval based on the "taxicab distance" from the DDM center of the mass to the DDM maximum position gave the best result. It was found that wind-speed retrievals based on "distance"-related observables provide more accurate wind-speed estimates compared to the retrieval based on the DDM-area metrics. The reason is

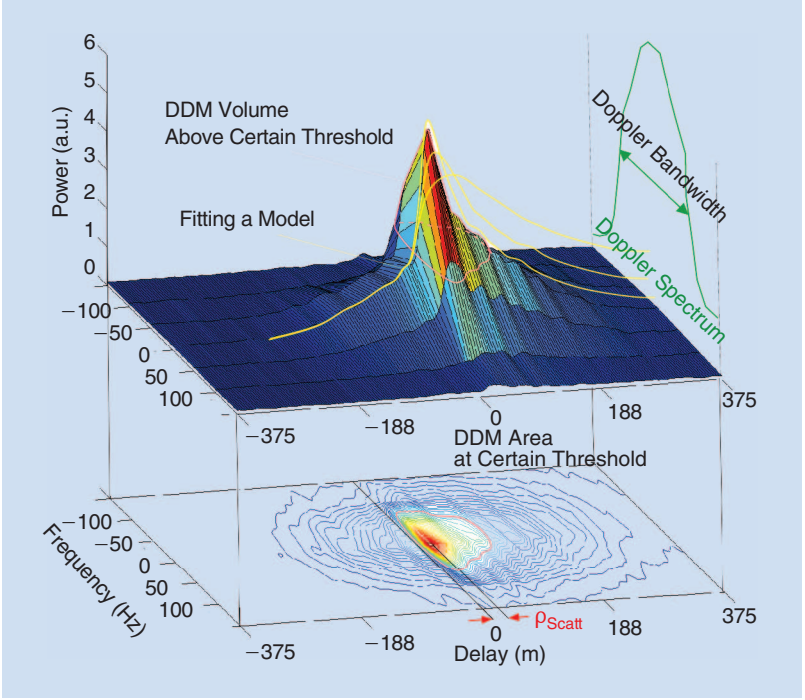


**FIGURE 25.** Several of the roughness/wind-retrieval algorithms are sketched here, using as an example an iGNSS-R DDM obtained from a real experimental flight. The data are available in [143].

that the "distance"-related observables are more sensitive to wind speed and less sensitive to variations of the elevation angle [176]. A new descriptor based on the DDM was proposed for wind-direction retrieval in [177]. This descriptor, designated as the skewness angle, measures the asymmetry in the DDM power distribution along the Doppler frequency axis, and it was modeled as a function of wind direction by means of a simulation study. Then that model was validated using real GNSS-R data from an airborne experiment. After validation, the DDM skewness model was successfully used for wind-direction retrieval with a resulting RMS error on the order of 20°.

#### *(C) SCATTEROMETRIC-DELAY*

As seen in Section VII.A.1, the arrival time of the waveform's peak does not correspond to the arrival time of the specular reflection. We can define the range between both arrivals as the scatterometric delay: $\rho_{\text{scatt}} = \rho_{\text{peak}} - \rho_{\text{spec}}$. For a given geometry, this delay is nearly linear with MSS [28]. This fact is applied to airborne-acquired data to retrieve the surface's slope variances, MSS [142], [178]. This technique can be applied to airborne and high-altitude ground-based experiments, but it is likely that the scatterometric delay would quickly saturate in spaceborne scenarios.

#### *(D) LINEAR OR DECONVOLUTION APPROACHES*

A set of approaches attempts to untangle geophysical information from the radar equation by its reorganization in sets of linear equations or deconvolution. In general, these approaches are suited for airborne and spaceborne scenarios. For example, if the GNSS bistatic radar equation is re-organized in a series of terms, each depending on the surface slope, the system is linear with respect to the Probability Density Function (PDF) of the slopes. Discrete values of the PDF(s) are therefore obtained. This retrieval does not require an analytical model for the PDF (no particular statistics assumed), thus enabling one to obtain non-Gaussian features of the PDF (such as up/down-wind separation [108]).

A similar approach permits 2-D mapping of the normalized radar cross section (NRCS) over the glistening zone, directly inverted from the DDMs [179]. Accumulation of information from either combining several overlapping glistening zones or from time series of a single satellite DDM to linearly invert the sea roughness over a fixed 2-D grid was also suggested in [180] (where it was misnamed tomographic approach). The potential outcome of this latter technique to the CYGNSS mission is being investigated (N. Rodriguez-Alvarez and J.L. Garrison, personal communication).

#### *(E) COHERENCE-TIME*

When the specular component of the scattering is significant (very low-altitude observations, very slant geometries, or relatively calm waters), the coherence time of the interferometric complex field depends on the sea state. It is then possible to develop the algorithms to retrieve significant wave height [181], [182]. This approach is suitable for ground-based scenarios.

#### 2) SCATTEROMETRIC PERFORMANCE

The first analysis of the scatterometric performances expected from spaceborne GNSS-R based on UK-DMC data was investigated in [52]. The performance obtained was 1.8 m/s rms error for weak and moderate winds. The most recent re-validation study of the UK-DMC results is presented in [116]. It is based on wind retrieval that combines five different GNSS-R observables applied to UK-DMC low-Earth orbiter GNSS-R data, and compares the inferred values to collocated buoy information.

The performance obtained is of the order of 1.7 m/s error in a range of winds from 2.4 to 10.7 m/s, which very close to the results obtained in [52]. This is also consistent with former estimates of the scatterometric performance for airborne platforms such as in [10] and [167]. The wind-speed uncertainties found in [167], using stratospheric GNSS-R data, resulted in precision from 0.1 to 2 m/s in a range of wind speeds from 1 to 8 m/s. And in [10], the precision achieved from aircraft altitudes is of the order of 1 m/s.

An intense experimental work on wind retrieval under hurricane-like conditions, achieving ~4 m/s precision in retrievals of high winds was compiled in [20]–[22], [183].

There is a general agreement that GNSS-R is sensitive to anisotropies and wind direction with 180° ambiguity [16], [18], [168], [177], [180]. However, more recent data analysis strategies permitted inferring non-Gaussian features of the surface slopes statistics, including the sense (up- or down-wind) direction, and breaking the 180° ambiguity [108]. The inhomogeneities of the wave field within the glistening zone can also be explored, as explained above in this Section. (see, e.g., [179]).

### *C. SOIL MOISTURE AND VEGETATION*

As described in Section IV, the permittivity of the reflecting surface has direct impact on the received power, through the Fresnel reflection coefficient (see (12)). In its turn, the permittivity of the soil depends on its moisture content and vegetation cover (e.g., [76]). Being L-band signals, GNSS reflections are mostly sensitive to the upper 1–2 cm layer of the soil [34], [40]. When the soil is covered with dense vegetation, the bistatic scattering around the specular direction is essentially influenced by the attenuation [184], so that the reflection power decreases with increasing plant biomass.

The use of GNSS signal surface multipath interference for ground dielectric permittivity monitoring data of GNSS ground-based stations was first proposed in [185], [186]. To mitigate an adverse effect of the surface roughness in GNSS-R moisture retrievals, a reception of the scattered signal at two orthogonal linear polarizations with analyzing their ratio was suggested in [187]. A simpler approach was examined experimentally for which only the circular cross-polar component of the reflected field was acquired

[33], [34], often normalized by the direct co-polar signal. The technique recently has been extended to include both circular components in [188], [189].

Over bare soil, and if the reflection process were perfectly coherent, the ratio between the reflected and the line-of-sight electromagnetic fields would be directly proportional to the Fresnel reflection coefficient, together with a geometric factor due to the longer path trajectory of the reflected signal, and instrumental factors (the antenna pattern). Due to incoherent scattering, the scattered peak power is also a function of the surface roughness. On top of this, the vegetation canopy also affects the bistatic scattering. Then, the separation between the vegetation, the roughness, and the soil moisture effects onto the total power must be carefully tackled, and for which it is important to properly model the relative contribution of the coherent and incoherent scattering.

The strategy in [189] is to isolate the coherent component by subtracting the incoherent one (based on temporal integration methods). Alternatively, forward models can help in the inversion of mixed (coherent and incoherent) observations, taking into account that the radar equation (11) assumes incoherent scattering solely. An implementation of the complete model that accounts for both coherent and incoherent components of the scattering, soil roughness, and vegetation canopy is presented in [80].

From static ground-based stations, the multi-path reflectometry and interferometric pattern techniques (which will be explained in Section VII.F) have shown robust evidence of their capabilities to sense soil moisture (e.g., [38], [40], [43], [46], [190]), and vegetation (e.g., [44]–[45]). Currently, thanks to the initiative of the EarthScope Plate Boundary Observatory (PBO), soil moisture and vegetation products obtained with these techniques are available from the PBO $H_2O$ network of more than 100 (soil moisture) and 360 (vegetation) GNSS geodetic stations across the western USA [191], [192]. The retrieval error of the bare soil moisture due to surface roughness in these interferometric techniques has been reported at 3–4% level [46].

Observations of soil moisture spatial variations from space using UK-DMC data were discussed in [48], [50].

### D. SNOW

Continental snow is currently being monitored with GNSS reflectometry as it occurs in geodetic GNSS stations. The multi-path reflectometry technique analyzes the interferometric pattern to infer the depth of the snow. The measurement principle is based on the frequency of the interference to measure snow depth variations (e.g., [39], [193]), or on both its frequency and amplitude to solve for snow thickness and equivalent water content [194], [195]. As in the case of soil moisture, the PBO $H_2O$ network monitors continental snow cover over more than 150 GNSS geodetic stations across the western USA [191], [196]–[198].

The estimated precision of these measurements is at a few cm level. Linear polarization antennas can also be used to quantify the number and location of the interference notches and solve for the thickness of the snow layer [199]. These sets of algorithms are based on the interferometric pattern technique described in Section VII.F.

An extreme case of interferences can be found in reflections off thick dry snow, such as the snow cover in continental polar sheets (Greenland and Antarctica). The upper layers of some of these thick layers of snow are very dry and light, for which L-band signals can penetrate down to a few hundreds of meters. Then, multiple reflections off different sub-surface snow layers might occur. The scattering components originated from these snow layers are essentially coherent, interfering with each other. It is then possible to separate these different reflections by means of radio-holographic analysis: applying spectral techniques to the complex field after subtracting a complex reference field (e.g., the line-of-sight signal) [115], [200]. Reflections off snow sub-surface layers down to almost 300 meters have been reported in Concordia Station (Dome C, Antarctica).

### E. SEA ICE

Because the sea-ice surface can be relatively smooth, especially at its earlier stages of development, L-band signals reflect coherently. Then, phase-delay altimetry (Section VII.A.4) can be feasible in this case, as was proved in [147], [148], and [200]. Such measurements can be related to the ice thickness or free-board level. The fact that dry snow is essentially transparent for L-band signals, makes measurements of ice thickness using this technique less contaminated by snow piling up over sea ice.

Besides altimetric measurements, GNSS reflectometry has been used to characterize Arctic sea ice. A correlation between the peak power of the GPS returns and RADARSAT backscattered measurements over such surfaces has been shown in the aircraft experiment [35]. A demonstration of technical feasibility of obtaining sea-ice information from space using UK-DMC data was presented in [51].

Both permittivity (temperature and brine) and sea-ice surface roughness retrievals were achieved by analyzing the shape of GPS waveforms and comparing it to a model [36], [37]. Alternatively, the ratio between the amplitudes of both circular (cross- and co-) polarizations has shown sensitivity to variations in the permittivity of the sea ice, especially at relatively low elevation angles of observation, around the pseudo-Brewster angle [200].

### F. INTERFEROMETRIC PATTERN TECHNIQUE (IPT) AND MULTIPATH-REFLECTOMETRY (GNSS-MR)

In the context of this tutorial, the interferometric pattern technique and multi-path reflectometry will be understood as the techniques that use the interference between the line-of-sight signal and the Earth-surface reflected one when the receiving system is at low altitude and under static conditions (left panel in Fig. 26). Strictly speaking, using the interferometric fringes to extract information about the reflecting surface can also be used under other conditions (e.g., [144] from a LEO). Under our restricted definition, many

aspects are simplified: most of the systematic effects cancel out, and the geometry variations at observation time scales come solely from the movement of the transmitter. Both IPT and multipath reflectometry are based on the same principle, but for historical reasons the multipath-reflectometry term is often applied to those "accidental" or undesirable reflections such as in GNSS geodetic stations. In this case, the interfering signals are co-polar (RHCP) only. The IPT has been used often in dedicated experiment, often using dedicated equipment and sometimes in other polarization basis.

The measurement principle of this technique is explained in the central panel of Fig. 26. The coherent component of the signal scattered on the ground surface, around the GNSS antenna, has a different ray path with respect to the direct one (changing as the transmitter moves across the sky), and it will be affected by the permittivity of the reflecting media, or even by secondary reflection in layers of a third type of media (e.g. vegetation layer). The frequency of the oscillations depends on the altitude of the receiver above the reflecting surface: every time the reflected ray path increases/reduces its range with respect to the direct signal by one electromagnetic wavelength $\lambda$, the total received power goes through one interferometric oscillation. The amplitude of the oscillations relates to different factors. Some are instrumental, such as the antenna patterns and polarization characterization. Others are related to the reflecting surface, such as the roughness of the reflecting surface (incoherent contribution) and its reflectivity (Fresnel coefficient, in turn linked to the permittivity of the medium). The permittivity of the medium also modifies the phase of the scattered signal, and thus the phase of the interferometric oscillation. This effect is used to extract soil moisture products [191], [192]. It is modeled in [201], and the open-source software is available [202].

The right panel in Fig. 26 sketches the behavior of the interferometric pattern when observed with a vertically-polarized antenna. Then, around the pseudo-Brewster angle, the fading V-pol-reflected signal creates a distinct minimum ("notch") accompanied by the interferometric oscillation (leaving only the power from the direct signal). Because the pseudo-Brewster angle is a function of the propagation and reflecting media complex permittivities, the location of the minimum and its amplitude provides useful information to invert these observations into the parameters that drive the permittivity of the reflecting medium. If another layer is present, secondary minima appear, permitting its characterization. [190] contains the model for a three-medium scenario (air, one surface layer, one sub-surface layer). The model, initially implemented for soil moisture layers, later proved applicable to other layering, such as vegetation [46] and snow [199].

## VIII. CURRENT AND FUTURE SPACE-BASED MISSIONS

### A. TechDemoSat-1

Following the success of the UK-DMC experiment, Surrey Satellite Technology Limited in the U.K. embarked on the development of a more advanced autonomous GNSS remote sensing instrument which was successfully launched on July 8, 2014 onboard the TechDemoSat-1 satellite [53]. This instrument will provide the baseline instrument which the CYGNSS mission will carry and will operate for approximately every two days out of 14 (due to time-sharing arrangements with other new technologies being tested). In addition to tracking L1 C/A code reflections from space and generating delay Doppler maps of surface reflections onboard, it will also detect and map reflections from the GPS L2 signals from space for the first time. This mission and instrument will provide a key demonstration of maturing GNSS technology, moving several applications well beyond the raw data sampling and ground-processing demonstrations that were performed on the UK-DMC experiment nearly a decade earlier.

### B. CYGNSS

The capabilities of GNSS-R ocean wind remote sensing were clearly recognized by NASA when it selected the University

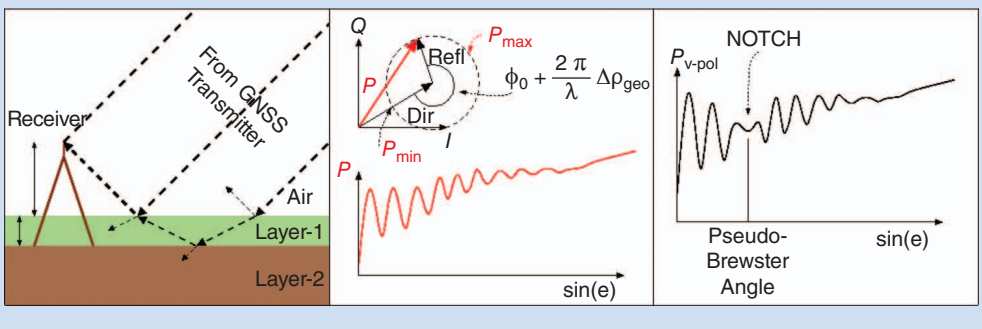


**FIGURE 26.** Sketch of the IPT and GNSS-MR for ground-based scenarios. (Left) a static receiver at low altitude that can capture both direct and reflected signals through the same antenna. In some cases, reflections from interfaces of different layers might occur. (Center) Example of coherent summation of the direct signal and a reflected one on the In-phase and Quadrature space. The total power oscillates, providing the interferometric pattern. The phase of these oscillations relates to the changing geometry, their amplitude to the permittivities of the media and incoherent scattering. (Right) Same pattern but for the V-component of the polarization. Around the pseudo-Brewster angle, the V-polarization of the fading reflected signal forms a notch as it does the oscillation. Reflections off secondary layers introduce secondary notches.

of Michigan led proposal for the Cyclone GNSS (CYGNSS) mission for the Earth Ventures 2 call [54]. CYGNSS consists of a constellation of eight satellites in an equatorial orbit, each carrying a delay-Doppler mapping receiver. CYGNSS's primary mission goal is to sense ocean wind and wave conditions in the inner core of tropical cyclones to improve intensity forecasting. Additionally, the ocean wind measurements provided by CYGNSS over its lifetime are expected to prove very valuable to the wider physical oceanography community, providing a wealth of measurements to study the Earth's global climate. CYGNSS is scheduled for launch in 2016 and will generate measurements at approximately five hour intervals in the Earth's equatorial regions (see coverage simulation in this tutorial). As an added bonus, it will also generate measurements over land surfaces allowing further validation of GNSS-R land-sensing techniques such as the estimation of near surface soil moisture.

### C. $^3$CAT-2

$^3$Cat-2 is a $3 \times 2$ unit CubeSat-based GNSS-R/-RO research/demonstration mission carried out by the Remote Sensing Lab and the NanoSat Lab at the Universitat Politècnica de Catalunya-Barcelona Tech. It is supported by a Spanish Research grant for the payload and platform, by an FP7 EU project for the launch, and by the Institut d'Estudis Espacials de Catalunya (IEEC) for some of personnel costs. Its launch is scheduled for the end of 2015 [55], [56].

$^3$Cat-2's main payload is PYCARO: the P(Y) and C/A ReflectOmeter [124]. It includes two receiving channels, and two dual-frequency (L1+L2) and dual-polarization (switchable) antennas: the zenithal antenna, a single microstrip patch, and the nadir-looking antenna, a $3 \times 2$ array of microstrip patches with ~13 dB gain. An additional Software Defined Radio will compute complete Delay Doppler Maps over selected targets (ocean, land, ice, and boreal forests). In nadir-pointing mode, it will perform GNSS-R observations, and in selected orbits it will be oriented in limb-pointing mode to perform polarimetric radio occultations (secondary objective). PYCARO has been tested in two stratospheric balloon experiments (October 2013 and October 2014) supported by ESA's Educational Office within the REXUS/BEXUS program. During the second flight on October 8th, 2014, PYCARO collected for the first time ever—to authors' knowledge—GPS, GLONASS and Galileo reflected signals over land from ~30 km height at both LHCP and RHCP, and at both L1 and L2 bands (see the cover page).

### D. PARIS-IoD

The concept of Passive Reflectometry and Interferometry System (PARIS) using GNSS reflected signals for ocean altimetry was proposed by ESA in 1993 [6]. Recently, ESA has initiated a study of an in-orbit demonstration mission named the PARIS In-orbit Demonstrator, (PARIS IoD) [74]. Its goal is to demonstrate that accurate mesoscale altimetry using a GNSS reflections is feasible. The required accuracy should be achieved by using GNSS bandwidth of all available signals ($3 \times 40$ MHz) by performing the direct correlation between up- and down-looking signals. As of the end of 2012 the mission has concluded its Phase-A (feasibility) studies.

### E. GEROS

GEROS-ISS stands for GNSS REflectometry, Radio Occultation and Scatterometry onboard the International Space Station. It is a scientific experiment, proposed to the European Space Agency (ESA) in 2011 for installation onboard the ISS. The main focus of GEROS is the dedicated use of signals from the currently available Global Navigation Satellite Systems (GNSS) for remote sensing of the Earth system with focus to climate change studies [57]. The primary mission objectives of GEROS are: (1) to measure the altimetric sea-surface height of the ocean using reflected GNSS signals to allow methodology demonstration, establishment of error budget, and resolutions and comparison/synergy with results of satellite-based nadir-pointing altimeters, and (2) to retrieve scalar ocean surface mean square slope (MSS), which is related to sea roughness, wind speed and direction, with a GNSS spaceborne receiver to allow methodology testing, establishment of error budget and resolutions. The mission entered into Phase-A (feasibility studies) during the fourth quarter of 2014.

## IX. SUMMARY

In this tutorial, we covered numerous techniques and applications of remote sensing using GNSS bistatic radar of opportunity. We presented a short history of the subject, described basic physical principles of this technique and related signal processing methods, introduced various remote sensing application areas, and concluded with brief accounts of current and planned space-based missions. More than 25 years ago, it was first suggested for scatterometry, and a few years later, as a new tool for ocean altimetry. Soon after that, the first airborne experiments were conducted by small groups of enthusiasts to prove the feasibility of the GNSS reflectometry to do altimetry, measure ocean winds and soil moisture. All these experiments used dedicated GNSS receivers specially designed to single out surface reflections in order to further extract geophysical information. Later researchers found that geodetic GNSS instruments also can be used to measure soil moisture, snow depth, and vegetation growth in the vicinity of their antennas from the interference pattern created by multipath.

While the airborne GNSS-R bistatic systems has received appreciation among U.S. and European researchers in the field of remote sensing, the ultimate goal was to fly those sensors in low Earth's orbit. A first such attempt was made in 2003 with the UK-DMC satellite and GNSS-R experiment. Using it, researchers collected short data sets with signals reflected of the ocean surface, the land, and sea ice. The first delay-Doppler maps were obtained from space and analyzed on the ground. Eleven years later another UK satellite, TechDemoSat-1, was successfully launched in

July 2014. Now, both in Europe and in the U.S., researchers are planning new missions that will continue further use of the GNSS-R technique for remote sensing purposes. The launch of a demonstration GNSS-R instrument will be conducted in 2015 onboard the European 3Cat-2 satellite. The NASA CYGNSS constellation is planned for launch in October 2016. It will consist of eight small satellite observatories. The goal of the proposed mission is to provide researchers with ocean surface winds throughout the life cycle of hurricanes for better weather forecasting.

These days we are witnessing how the GNSS-R remote sensing is coming out of its infancy and heading toward a more mature state. There are a number of challenges ahead that need to be addressed, but a vision for GNSS-R remote sensing looks promising both for airborne and spaceborne systems. They can nicely complement existing radar and radiometer remote sensing, and in some situations can provide unique opportunities and capabilities that cannot be achieved by existing traditional remote sensing tools.

## REFERENCES


[1] A. S. Gurvich and T. G. Krasil'nikova, "Navigation satellites for radio sensing of the Earth' atmosphere," (in Russian), *Issled. Zemli Kosmosa (Sov. J. of Remote Sensing, Engl. Transl.)*, vol. 6, pp. 1124–1131, 1990.

[2] T. P. Yunck, G. F. Lindal, and C.-H. Liu, "The role of GPS in precise Earth observation," presented at IEEE Position Location Navigation Symp., Orlando, FL, 1988.

[3] R. Ware, C. Rocken, F. Solheim, D. Feng, B. Herman, M. Gorbunov, S. Sokolovskiy, K. Hardy, Y.-H. Kuo, X. Zou, K. Trenberth, T. Meehan, W. Melbourne, and S. Businger, "GPS sounding of the atmosphere from low Earth orbit: Preliminary results," *Bull. Amer. Meteorol. Soc.*, vol. 77, no. 1, pp. 19–40, 1996.

[4] E. R. Kursinski, G. A. Hajj, W. I. Bertiger, S. S. Leroy, T. K. Meehan, L. J. Romans, J. T. Schofield, D. J. McCleese, W. G. Melbourne, C. L. Thornton, T. P. Yunck, J. R. Eyre, and R. N. Nagatani, "Initial results of radio occultation observations of Earth's atmosphere using the Global Positioning System," *Science*, vol. 271, no. 5252, pp. 1107–1110, 1996.

[5] C. Hall and R. Cordy, "Multistatic scatterometry," in *Proc. IEEE Int. Geoscience Remote Sensing Symp.*, Edinburgh, Scotland, July 1988.

[6] M. Martin-Neira, "A passive reflectometry and interferometry system (PARIS): Application to ocean altimetry," *Ecol. Soc. Amer. J.*, vol. 17, no. 4, pp. 331–355, Dec. 1993.

[7] G. L. Tyler and H. T. Howard, "Dual-frequency bistatic radar investigation of the moon with Apollos 14 and 15," *J. Geophys. Res.*, vol. 78, no. 23, pp. 4852–4874, 1973.

[8] A. G. Pavel'ev, M. A. Kozlov, O. I. Yakovlev, A. I. Kucheryavenkov, Y. P. Molotov, and O. Y. Milekhin, "The study of Venus by means of the bistatic radar method," *Radio Eng. Electron. Phys.*, vol. 23, pp. 1–8, Oct. 1978.

[9] A. I. Kucheryavenkov, O. E. Milekhin, and A. G. Pavel'ev, "Bistatic radar Earth remote sensing," *Sov. J. Remote Sens.*, vol. 6, no. 4, pp. 628–643, 1990.

[10] J. L. Garrison, S. J. Katzberg, and M. I. Hill, "Effect of sea roughness on bistatically scattered range coded signals from the Global Positioning System," *Geophys. Res. Lett.*, vol. 25, no. 13, pp. 2257–2260, July 1998.

[11] B. Lin, S. J. Katzberg, J. L. Garrison, and B. Wielicki, "The relationship between the GPS signals reflected from sea surface and the surface winds: Modeling results and comparisons with aircraft measurements," *J. Geophys. Res.*, vol. 104, no. C9, pp. 20713–20728, 1999.

[12] G. Beyerle and K. Hocke, "Observation and simulation of direct and reflected GPS signals in radio occultation experiments," *Geophys. Res. Lett.*, vol. 28, no. 9, pp. 1895–1898, May 2001.

[13] G. Beyerle, K. Hocke, J. Wickert, T. Schmidt, C. Marquardt, and C. Reigber, "GPS radio occultations with CHAMP: A radio holographic analysis of GPS signal propagation in the troposphere and surface reflections," *J. Geophys. Res.*, vol. 107, no. D24, p. 4802, 2002.

[14] S. Lowe, J. L. LaBrecque, C. Zuffada, L. J. Romans, L. E. Young, and G. A. Hajj, "First spaceborne observation of an Earth-reflected GPS signal," *Radio Sci.*, vol. 37, no. 1, pp. 1–28, 2002.

[15] A. Komjathy, V. U. Zavorotny, P. Axelrad, G. H. Born, and J. L. Garrison, "GPS signal scattering from sea surface: Wind speed retrieval using experimental data and theoretical model," *Remote Sens. Environ.*, vol. 73, no. 1, pp. 162–174, 2000.

[16] M. Armatys, "Estimation of sea surface winds using reflected GPS Signals," Ph.D. dissertation, Univ. Colorado, Boulder, CO, 2001.

[17] J. L. Garrison, A. Komjathy, V. U. Zavorotny, and S. J. Katzberg, "Wind speed measurements using forward scattered GPS signals," *IEEE Trans. Geosci. Remote Sensing*, vol. 40, no. 1, pp. 50–65, Jan. 2002.

[18] A. Komjathy, M. Armatys, D. Masters, P. Axelrad, V. Zavorotny, and S. Katzberg, "Retrieval of ocean surface wind speed and wind direction using reflected GPS signals," *J. Atmos. Ocean. Technol.*, vol. 21, no. 3, pp. 515–526, 2004.

[19] V. U. Zavorotny and A. G. Voronovich, "Scattering of GPS signals from the ocean with wind remote sensing application," *IEEE Trans. Geosci. Remote Sensing*, vol. 38, no. 1, pp. 951–964, Mar. 2000.

[20] S. J. Katzberg, R. A. Walker, J. H. Roles, T. Lynch, and P. G. Black, "First GPS signals reflected from the interior of a tropical storm: Preliminary results from hurricane Michael," *Geophys. Res. Lett.*, vol. 28, no. 10, pp. 1981–1984, 2001.

[21] S. J. Katzberg, O. Torres, and G. Ganoe, "Calibration of reflected GPS for tropical storm wind speed retrievals," *Geophys. Res. Lett.*, vol. 33, p. L18602, Sept. 2006.

[22] S. J. Katzberg and J. Dunion, "Comparison of reflected GPS wind speed retrievals with drop-sondes in tropical cyclones," *Geophys. Res. Lett.*, vol. 36, pp. 95–109, Sept. 2009.

[23] R. N. Treuhaft, S. T. Lowe, C. Zuffada, and Y. Chao, "Two-cm GPS altimetry over Crater Lake," *Geophys. Res. Lett.*, vol. 28, no. 23, pp. 4343–4346, 2001.

[24] M. Martín-Neira, M. Caparrini, J. Font-Rosselló, S. Lannelongue, and C. S. Vallmitjana, "The PARIS concept: An experimental demonstration of sea surface altimetry using GPS reflected signals," *IEEE Trans. Geosci. Remote Sensing*, vol. 39, no. 1, pp. 142–149, 2001.

[25] M. Martín-Neira, P. Colmenarejo, G. Ruffini, and C. Serra, "Altimetry precision of 1 cm over a pond using the wide-lane carrier phase of GPS reflected signals," *Can. J. Remote Sens.*, vol. 28, no. 3, pp. 394–403, June 2002.

[26] S. T. Lowe, C. Zuffada, Y. Chao, P. Kroger, L. E. Young, and J. L. LaBrecque, "5-cm precision aircraft ocean altimetry using GPS reflections," *Geophys. Res. Lett.*, vol. 29, no. 10, p. 1375, 2002.

[27] S. T. Lowe, P. M. Kroger, G. W. Franklin, J. L. LaBrecque, J. Lerma, M. F. Lough, M. R. Marcin, D. J. Spitzmesser, and L. E. Young, "A delay/Doppler-mapping receiver system for GPS-reflection remote sensing," *IEEE Trans. Geosci. Remote Sensing*, vol. 40, no. 5, pp. 1150–1163, 2002.

[28] A. Rius, J. M. Aparicio, E. Cardellach, M. Martin-Neira, B. Chapron, "Sea surface state measured using GPS reflected signals," *Geophys. Res. Lett.*, vol. 29, no. 23, pp. 37-1–37-4, Dec. 2002.

[29] G. Ruffini, F. Soulat, M. Caparrini, O. Germain, and M. Martin-Neira, "The eddy experiment: Accurate GNSS-R ocean altimetry from low altitude aircraft," *Geophys. Res. Lett.*, vol. 31, no. 2, p. L12306, June 2004.

[30] V. Zavorotny, D. Masters, A. Gasiewski, B. Bartram, S. Katzberg, P. Axelrad, and R. Zamora, "Seasonal polarimetric measurements of soil moisture using ground-based GPS bistatic radar," in *Proc. IEEE Int. Geoscience Remote Sensing Symp.*, Toulouse, France, 2003, pp. 781–783.

[31] V. Zavorotny, F. Lalezari, A. Gasiewski, T. Boone, D. Masters, S. Esterhuizen, E. McIntyre, B. Bartram, R. Zamora, P. Axelrad, and S. Katzberg, "Measurements of soil moisture using stationary GPS bistatic radar and L-band radiometry," in *Proc. IEEE Int. Geoscience Remote Sensing Symp.*, Anchorage, AK, 2004.

[32] D. Masters, "Surface remote sensing applications of GNSS bistatic radar: Soil moisture and aircraft altimetry," Ph.D. dissertation, Univ. Colorado, Boulder, CO, 2004.

[33] D. Masters, P. Axelrad, and S. Katzberg, "Initial results of land-reflected GPS bistatic radar measurements in SMEX02," *Remote Sens. Environ.*, vol. 92, no. 4, pp. 507–520, 2004.

[34] S. J. Katzberg, O. Torres, M. S. Grant, and D. Masters, "Utilizing calibrated GPS reflected signals to estimate soil reflectivity and dielectric constant: Results from SMEX02," *Remote Sensing Environ.*, vol. 100, pp. 17–28, 2005.

[35] A. Komjathy, J. Maslanik, V. U. Zavorotny, P. Axelrad, and S. J. Katzberg, "Sea ice remote sensing using surface reflected GPS signals," in *Proc. IEEE Int. Geoscience Remote Sensing Symp.*, Honolulu, HI, July 2000, pp. 2855–2857.

[36] M. Belmonte, "Bistatic scattering of global positioning system signals from Arctic sea ice," Ph.D. dissertation, Univ. Colorado, Boulder, CO, 2007.

[37] M. Belmonte, J. A. Maslanik, and P. Axelrad, "Bistatic scattering of GPS signals off Arctic sea ice," *IEEE Trans. Geosci. Remote Sensing*, vol. 48, no. 3, pp. 1548–1553, 2009.

[38] K. M. Larson, E. E. Small, E. D. Gutmann, A. D. Bilich, J. J. Braun, and V. U. Zavorotny, "Use of GPS receivers as a soil moisture network for water cycle studies," *Geosci. Res. Lett.*, vol. 35, no. 24, p. L24405, 2008.

[39] K. M. Larson, E. D. Gutmann, V. U. Zavorotny, J. J. Braun, M. W. Williams, and F. G. Nievinski, "Can we measure snow depth with GPS receivers?" *Geosci. Res. Lett.*, vol. 36, p. L17502, Sept. 2009.

[40] K. M. Larson, J. Braun, E. E. Small, V. Zavorotny, E. Gutmann, and A. Bilich, "GPS multipath and its relation to near-surface soil moisture content," *IEEE J. Select. Topics Appl. Earth Observ. Remote Sensing*, vol. 3, no. 1, pp. 91–99, 2010.

[41] V. U. Zavorotny, K. M. Larson, J. J. Braun, E. E. Small, E. D. Gutmann, and A. L. Bilich, "A physical model for GPS multipath caused by land reflections: Toward bare soil moisture retrievals," *IEEE J. Select. Topics Appl. Earth Observ. Remote Sensing*, vol. 3, no. 1, pp. 100–110, 2010.

[42] E. D. Gutmann, K. M. Larson, M. W. Williams, F. G. Nievinski, and V. Zavorotny, "Snow measurement by GPS interferometric reflectometry: An evaluation at Niwot Ridge, Colorado," *Hydrol. Process.*, vol. 26, no. 19, pp. 2951–2961, Sept. 15, 2012.

[43] C. C. Chew, E. E. Small, K. M. Larson, and V. U. Zavorotny, "Effects of near-surface soil moisture on GPS SNR data: Development of a retrieval algorithm for soil moisture," *IEEE Trans. Geosci. Remote Sensing*, vol. 52, no. 1, pp. 537–543, Jan. 2014.

[44] K. M. Larson and E. E. Small, "Normalized microwave reflection index: A vegetation measurement derived from GPS Networks," *IEEE J. Select. Topics Appl. Earth Observ. Remote Sensing*, vol. 7, no. 5, pp. 1501–1511, May 2014.

[45] E. E. Small, K. M. Larson, and W. K. Smith, "Normalized microwave reflection index: Validation of vegetation water content estimates from Montana grasslands," *IEEE J. Select. Topics Appl. Earth Observ. Remote Sensing*, vol. 7, no. 5, pp. 1512–1521, May 2014.

[46] N. Rodriguez-Alvarez, A. Camps, M. Vall-llosera, X. Bosch-Lluis, A. Monerris, I. Ramos-Perez, E. Valencia, J. F. Marchan-Hernandez, J. Martinez-Fernandez, G. Baroncini-Turricchia, C. Pérez-Gutiérrez, and N. Sánche, "Land geophysical parameters retrieval using the interference pattern GNSS-R technique," *IEEE Trans. Geosci. Remote Sensing*, vol. 32, no. 1, pp. 47–61, Jan. 2011.

[47] S. T. Gleason, S. Hodgart, S. Yiping, C. Gommenginger, S. Mackin, M. Adjrad, and M. Unwin, "Detection and processing of bistatically reflected GPS signals from low Earth orbit for the purpose of ocean remote sensing," *IEEE Trans. Geosci. Remote Sensing*, vol. 43, no. 6, pp. 1229–1241, June 2005.

[48] S. Gleason, "Remote sensing of ocean, ice and land surfaces using bistatically scattered GNSS signals from low earth orbit," Ph.D. dissertation, Univ. Surrey, Guildford, U.K., 2006.

[49] M. P. Clarizia, C. Gommenginger, S. Gleason, M. Srokosz, C. Galdi, and M. di Bisceglie, "Analysis of GNSS-R delay-Doppler maps from the UK-DMC satellite over the ocean," *Geophys. Res. Lett.*, vol. 36, p. L02608, Jan. 2009.

[50] S. Gleason, S. Lowe, and V. Zavorotny, "GNSS applications and methods," in *Remote Sensing with Bistatic GNSS Reflections*, S. Gleason and D. Gebre-Egziabher, Eds. Norwood, MA: Artech House, 2009, pp. 399–436.

[51] S. Gleason, "Towards sea ice remote sensing with space detected GPS signals: Demonstration of technical feasibility and initial consistency check using low resolution sea ice information," *Remote Sens.*, vol. 2, no. 8, pp. 2017–2039, 2010.

[52] S. Gleason, "Space based GNSS scatterometry: Ocean wind sensing using empirically calibrated model," *IEEE Trans. Geosci. Remote Sensing*, vol. 51, no. 9, pp. 4853–4863, 2013.

[53] M. Unwin, S. Duncan, P. Jales, P. Blunt, and M. Brenchley, "Implementing GNSS reflectometry in space on the TechDemoSat-1 mission," in *Proc. Institute Navigation*, Sept. 2014.

[54] C. S. Ruf, S. Gleason, Z. Jelenak, S. Katzberg, A. Ridley, R. Rose, J. Scherrer, and V. Zavorotny, "The CYGNSS nanosatellite constellation hurricane mission," in *Proc. IEEE Int. Geoscience Remote Sensing Symp.*, Munich, Germany, 2012, pp. 214–216.

[55] H. Carreno-Luengo, A. Camps, I. Perez-Ramos, G. Forte, R. Onrubia, R. Diez, "3Cat-2: A P(Y) and C/A GNSS-R experimental nano-satellite mission," in *Proc. IEEE Int. Geoscience Remote Sensing Symp.*, Melbourne, Australia, 2013, pp. 843–846.

[56] H. Carreno-Luengo, A. Camps, R. Jove-Casulleras, A. Alonso-Arroyo, R. Olive, A. Amezaga, D. Vidal, J. F. Munoz, "The 3Cat-2 project: GNSS-R in-orbit demonstrator for Earth observation," in *Proc. Small Satellites Services 4S Symp.*, Porto Petro, Majorca, Spain, 2014.

[57] J. Wickert, O. Andersen, G. Beyerle, E. Cardellach, B. Chapron, C. Gommenginger, J. Hatton, P. Høeg, A. Jäggi, N. Jakowski, M. Kern, T. Lee, M. Martin-Neira, O. Montenbruck, N. Pierdicca, A. Rius, C. K. Shum, and C. Zuffada, "Innovative remote sensing using the International Space Station: GNSS reflectometry with GEROS," in *Proc. IEEE Int. Geoscience Remote Sensing Symp.*, Québec City, QC, Canada, 2014.

[58] B. Hofmann-Wellenhof, H. Lichtenegger, and E. Wasle, *GNSS—Global Navigation Satellite Systems: GPS, GLONASS, Galileo, and More*. Wien and NewYork: Springer, 2008.

[59] [Online]. Available: http://en.wikipedia.org/wiki/Beidou_Navigation_Satellite_System

[60] [Online]. Available: http://en.wikipedia.org/wiki/Quasi-Zenith_Satellite_System

[61] [Online]. Available: http://en.wikipedia.org/wiki/Indian_Regional_Navigation_Satellite_System

[62] R. Shah, J. L. Garrison, and M. S. Grant, "Demonstration of bistatic radar for ocean remote sensing using communication satellite signals," *IEEE Geosci. Remote Sensing Lett.*, vol. 9, no. 4, pp. 619–623, July 2012.

[63] R. Shah and J. L. Garrison, "Correlation properties of direct broadcast signals for bistatic remote sensing," in *Proc. IEEE Int. Geoscience Remote Sensing Symp.*, Munich, Germany, 2012.

[64] R. Shah and J. L. Garrison, "Application of the ICF coherence time method for ocean remote sensing using digital communication satellite signals," *IEEE J. Select. Topics Appl. Earth Observ. Remote Sensing*, vol. 7, no. 5, pp. 1584–1591, May 2014.

[65] J. B.-Y. Tsui, *Fundamentals of Global Positioning System Receivers: A Software Approach*. New York: Wiley, 2000.
[66] R. Fontana, W. Cheung, and T. Stansell, "The modernized L2 civil signal: Leaping forward into the 21st century," *Global Position. Syst. World*, vol. 12, no. 9, pp. 28–34, 2000.
[67] P. Misra and P. Enge, *Global Positioning System: Signals, Measurements, and Performance*. Lincoln, MA: Ganga-Jamuna, 2001.
[68] New civil signals. [Online]. Available: http://www.gps.gov/systems/gps/modernization/civilsignals/#L5
[69] A. Egido. (2013). GNSS reflectometry for land remote sensing applications. Ph.D. dissertation, Univ. Politècnica de Catalunya-Barcelona Tech. [Online]. Available: http://hdl.handle.net/10803/129090
[70] (2010, Sept.). Galileo open service, signal in space interface control document. Issue 1, Revision 1. European Space Agency, Galileo Joint Undertaking. [Online]. Available: http://ec.europa.eu/enterprise/policies/satnav/galileo/files/galileo-os-sis-icd-issue1-revision1_en.pdf
[71] J. W. Betz, "Binary offset carrier modulations for radio navigation," *J. Inst. Navig.*, vol. 48, no. 4, pp. 227–246, Winter 2001–2002.
[72] D. Pascual, A. Camps, F. Martin, H. Park, A. A. Arroyo, and R. Onrubia, "Precision bounds in GNSS-R ocean altimetry," *IEEE J. Select. Topics Appl. Earth Observ. Remote Sensing*, vol. 7, no. 5, pp. 1416–1423, May 2014.
[73] (2011, Sept.). Navstar GPS Space Segment—User Segment L5 Interfaces, Interface Specification (IS-GPS-705). Revision B. Global Positioning System Wing (GPSW) Systems Engineering & Integration. [Online]. Available: http://www.gps.gov/technical/icwg/IS-GPS-705B.pdf
[74] M. Martin-Neira, S. D'Addio, C. Buck, N. Floury, and R. Prieto-Cerdeira, "The PARIS ocean altimeter in-orbit demonstrator," *IEEE Trans. Geosci. Remote Sensing*, vol. 49, no. 6, pp. 2209–2237, June 2011.
[75] S. G. Jin, E. Cardellach, and F. Xie, *GNSS Remote Sensing: Theory, Methods and Applications*. New York, London: Springer, 2014.
[76] F. T. Ulaby, R. K. Moore, and A. K. Fung, *Microwave Remote Sensing: Active and Passive*, vols. 1, 2 and 3. Norwood, MA: Artech House.
[77] J. C. Curlander and R. N. McDonough, *Synthetic Aperture Radar*, New York: Wiley Interscience, 1991.
[78] D. E. Barrick, "Relationship between slope probability density function and the physical optics integral in rough surface scattering," *Proc. IEEE (Lett.)*, vol. 56, pp. 1728–1729, Oct. 1968.
[79] F. G. Bass and I. M. Fuks, *Wave Scattering from Statistically Rough Surfaces*. New York: Pergamon, 1979.
[80] N. Pierdicca, L. Guerriero, R. Giusto, M. Brogioni, A. Egido, "SAVERS: A simulator of GNSS reflections from bare and vegetated soils," *IEEE Trans. Geosci. Remote Sensing*, vol. 52, no. 10, pp. 6542–6554, 2014.
[81] C. Zuffada and V. Zavorotny, "Coherence time and statistical properties of the GPS signal scattered off the ocean surface and their impact on the accuracy of remote sensing of sea surface topography and winds," in *Proc. IEEE Int. Geoscience Remote Sensing Symp.*, Sydney, Australia, 2001, pp. 3332–3334.
[82] H. You, G. Heckler, J. L. Garrison, and V. U. Zavorotny, "Stochastic voltage model and experimental measurement of ocean-scattered GPS signal statistics," *IEEE Trans. Geosci. Remote Sensing*, vol. 42, no. 10, pp. 2160–2169, 2004.
[83] H. You, J. L. Garrison, G. Heckler, and D. Smajlovic, "The autocorrelation of waveforms generated from ocean-scattered GPS signals," *IEEE Geosci. Remote Sensing Lett.*, vol. 3, no. 1, pp. 78–82, Jan. 2006.
[84] T. Elfouhaily and C. A. Guérin, "A critical survey of approximate scattering wave theories from random rough surfaces," *Waves Random Media*, vol. 14, no. 4, pp. R1–R40, 2004.
[85] A. K. Fung, *Microwave Scattering and Emission Models and Their Applications*. Norwood, MA: Artech House, 1994.
[86] A. G. Voronovich, "Small-slope approximation in wave scattering from rough surfaces," *Sov. Phys.—JETP*, vol. 62, no. 1, pp. 65–70, 1985.
[87] A. G. Voronovich, "Small-slope approximation for electromagnetic wave scattering at a rough interface of two dielectric half-spaces," *Waves Random Media*, vol. 4, no. 3, pp. 337–367, July 1994.
[88] A. G. Voronovich, *Wave Scattering from Rough Surfaces*, 2nd edn. Berlin, Germany: Springer, 1999.
[89] J. T. Johnson, "A study of ocean-like surface thermal emission and reflection using Voronovich's small slope approximation," *IEEE Trans. Geosci. Remote Sensing*, vol. 43, no. 2, pp. 306–314, Feb. 2005.
[90] C. Bourlier, N. Déchamps, and G. Berginc, "Comparison of asymptotic backscattering models (SSA, WCA, and LCA) from one-dimensional Gaussian ocean-like surfaces," *IEEE Trans. Antennas Propag.*, vol. 53, no. 5, pp. 1640–1653, May 2005.
[91] J. T. Johnson and T. M. Elfouhaily, "Computation of oceanlike surface thermal emission and bistatic scattering with the reduced local curvature approximation," *IEEE Trans. Geosci. Remote Sensing*, vol. 45, no. 7, pp. 2108–2115, July 2007.
[92] T. M. Elfouhaily and J. T. Johnson, "A new model for rough surface scattering," *IEEE Trans. Geosci. Remote Sensing*, vol. 45, no. 7, pp. 2300–2308, July 2007.
[93] G. Soriano and C.-A. Guérin, "A cutoff invariant two-scale model in electromagnetic scattering from sea surfaces," *IEEE Geosci. Remote Sensing Lett.*, vol. 5, no. 2, pp. 199–203, Apr. 2008.
[94] C.-A. Guérin, G. Soriano, and B. Chapron, "The weighted curvature approximation in scattering from sea surfaces," *Waves Random Complex*, vol. 20, no. 3, pp. 364–384, Aug. 2010.
[95] R. N. Treuhaft, S. T. Lowe, and E. Cardellach, "Formulating a vector wave expression for polarimetric GNSS surface scattering," *Progress Electromagn. Res. B*, vol. 33, pp. 257–276, 2011.
[96] M. P. Clarizia, C. Gommenginger, M. D. Bisceglie, C. Galdi, and M. A. Srokosz, "Simulation of L-band bistatic returns from the ocean surface: A facet approach with application to ocean GNSS reflectometry," *IEEE Trans. Geosci. Remote Sensing*, vol. 50, no. 3, pp. 960–971, 2012.
[97] G. R. Valenzuela, "Theories for the interaction of electromagnetic and oceanic waves—A review," *Boundary-Layer Meteorol.*, vol. 13, nos. 1–4, pp. 61–85, Jan. 1978.
[98] G. Brown, "Backscattering from a Gaussian distributed perfectly conducting rough surface," *IEEE Trans. Antennas Propag.*, vol. AP-26, no. 3, pp. 472–482, May 1978.
[99] A. G. Voronovich and V. U. Zavorotny, "Ocean-scattered polarized bistatic radar signals modeled with small-slope approximation," in *Proc. IEEE Int. Geoscience Remote Sensing Symp.*, Munich, Germany, July 2012, pp. 3415–3418.
[100] A. K. Fung, C. Zuffada, and C. Y. Hsieh, "Incoherent bistatic scattering from the sea surface at L-band," *IEEE Trans. Geosci. Remote Sensing*, vol. 39, no. 5, pp. 1006–1012, May 2001.
[101] C. Zuffada, A. K. Fung, J. Parker, M. Okolicanyi, and E. Huang, "Polarization properties of the GPS signal scattered off a wind driven ocean," *IEEE Trans. Antennas Propag.*, vol. 52, no. 1, pp. 172–187, Jan. 2004.
[102] D. R. Thompson, T. M. Elfouhaily, and J. L. Garrison, "An improved geometrical optics model for bistatic GPS scattering from the ocean surface," *IEEE Trans. Geosci. Remote Sensing*, vol. 43, no. 12, pp. 2810–2821, 2005.
[103] A. G. Voronovich and V. U. Zavorotny, "Full-polarization modeling of monostatic and bistatic radar scattering from a rough sea surface," *IEEE Trans. Antennas Propag.*, vol. 62, no. 3, pp. 1363–1371, Mar. 2014.
[104] J. T. Johnson and J. Ouellette, "A study of polarization features in bistatic scattering from rough surfaces," *IEEE Trans. Geosci. Remote Sensing*, vol. 52, no. 3, pp. 1616–1626, Mar. 2014.

[105] T. Elfouhaily, B. Chapron, K. Katsaros, and D. Vandemark, "A unified directional spectrum for long and short wind-driven waves," *J. Geophys. Res.*, vol. 102, pp. 15781–15796, July 1997.

[106] O. M. Phillips, "Spectral and statistical properties of the equilibrium range in the wind-generated gravity waves," *J. Fluid Mech.*, vol. 156, pp. 505–531, 1985.

[107] H. L. Tolman, B. Balasubramaniyan, L. D. Burroughs, D. V. Chalikov, Y. Y. Chao, H. S. Chen, and V. M. Gerald, "Development and implementation of wind generated ocean surface wave models at NCEP," *Weather Forecasting*, vol. 17, no. 12, pp. 311–333, 2002.

[108] E. Cardellach and A. Rius, "A new technique to sense non-Gaussian features of the sea surface from L-band bi-static GNSS reflections," *Remote Sens. Environ.*, vol. 112, no. 6, pp. 2927–2937, June 2008.

[109] A. Darawankul and J. T. Johnson, "Band-limited exponential correlation function for rough-surface scattering," *IEEE Trans. Geosci. Remote Sensing*, vol. 45, no. 5, pp. 1198–1206, May 2007.

[110] J. T. Johnson, K. F. Warnick, and P. Xu, "On the geometrical optics and physical optics approximations for scattering from exponentially correlated surfaces," *IEEE Trans. Geosci. Remote Sensing*, vol. 45, no. 8, pp. 2619–2629, 2007.

[111] L. A. Klein and C. T. Swift, "An improved model for the dielectric constant of sea water at microwave frequencies," *IEEE Trans. Antennas Propag.*, vol. 25, no. 1, pp. 104–111, Jan. 1977.

[112] M. T. Hallikainen, F. T. Ulaby, M. C. Dobson, M. A. El-Rayes, and L.-K. Wu, "Microwave dielectric behavior of wet soil—Part I: Empirical model and experimental observations," *IEEE Trans. Geosci. Remote Sensing*, vol. 23, no. 1, pp. 25–34, Jan. 1985.

[113] M. C. Dobson, F. T. Ulaby, M. T. Hallikainen, and M. A. El-Rayes, "Microwave dielectric behavior of wet soil—Part II: Dielectric mixing models," *IEEE Trans. Geosci. Remote Sensing*, vol. 23, no. 1, pp. 35–46, Jan. 1985.

[114] N. R. Peplinski, F. T. Ulaby, and M. C. Dobson, "Dielectric properties of soils in the 0.3–1.3-GHz range," *IEEE Trans. Geosci. Remote Sensing*, vol. 33, no. 5, pp. 803–807, May 1995.

[115] E. Cardellach, F. Fabra, A. Rius, S. Pettinato, and S. D'Addio, "Characterization of dry-snow sub-structure using GNSS reflected signals," *Remote Sensing Environ.*, vol. 124, pp. 122–134, Sept. 2012.

[116] M. P. Clarizia, C. S. Ruf, P. Jales, and C. P. Gommenginger, "Spaceborne GNSS-R minimum variance wind speed estimator," *IEEE Trans. Geosci. Remote Sensing*, vol. 52, no. 11, pp. 6829–6843, 2014.

[117] S. M. Kay, *Fundamentals of Statistical Signal Processing: Estimation Theory*. Upper Saddle River, NJ: Prentice Hall, 1993.

[118] A. Camps, F. Martin, H. Park, E. Valencia, A. Rius, and S. D'Addio, "Interferometric GNSS-R achievable altimetric performance and compression/denoising using the wavelet transform: An experimental study," in *Proc. IEEE Int. Geoscience Remote Sensing Symp.*, Munich, Germany, July 2012, pp. 7512–7515.

[119] A. Camps, D. Pascual, H. Park, and F. Martin, "PARIS IoD: ID-16A contribution to performance and error budgets," *Report PARIS-PhA-IEEC-UPC-TN-008*, rev 3.0, Nov. 14, 2012.

[120] A. Rius, F. Fabra, S. Ribo, J. C. Arco, S. Oliveras, E. Cardellach, A. Camps, O. Nogues-Correig, J. Kainulainen, E. Rohue, and M. Martin-Neira, "PARIS Interferometric Technique proof of concept: Sea surface altimetry measurements," in *Proc. IEEE Int. Geoscience Remote Sensing Symp.*, Munich, Germany, 2012, pp. 7067–7070.

[121] S. D'Addio and M. Martin-Neira, "Comparison of processing techniques for remote sensing of earth-exploiting reflected radio-navigation signals," *Electron. Lett.*, vol. 49, no. 4, pp. 292–293, 2013.

[122] E. Cardellach, A. Rius, M. Martín-Neira, F. Fabra, O. Nogués-Correig, S. Ribó, J. Kainulainen, A. Camps, and S. D'Addio, "Consolidating the precision of interferometric GNSS-R ocean altimetry using airborne experimental data," *IEEE Trans. Geosci. Remote Sensing*, vol. 52, no. 8, pp. 4992–5004, 2014.

[123] H. Park, D. Pascual, A. Camps, F. Martin, A. Alonso-Arroyo, and H. Carreno-Luengo, "Analysis of spaceborne GNSS-R delay-Doppler tracking," *IEEE J. Select. Topics Appl. Earth Observ. Remote Sensing*, vol. 7, no. 5, pp. 1481–1492, May 2014.

[124] H. Carreno-Luengo, A. Camps, I. Perez-Ramos, and A. Rius, "Pycaro's instrument proof of concept," in *Proc. Workshop Reflectometry Using GNSS Other Signals Opportunity (GNSS+R)*, West Lafayette, IN, 2012, pp. 1–4.

[125] H. Carreno-Luengo, A. Camps, I. Ramos-Perez, and A. Rius, "Experimental evaluation of GNSS-reflectometry altimetric precision using the P(Y) and C/A signals," *IEEE J. Select. Topics Appl. Earth Observ. Remote Sensing*, vol. 7, no. 5, pp. 1493–1500, May 2014.

[126] S. T. Lowe, T. Meehan, and L. Young, "Direct signal enhanced semicodeless processing of GNSS surface-reflected signals," *IEEE J. Select. Topics Appl. Earth Observ. Remote Sensing*, vol. 7, no. 5, pp. 1469–1472, May 2014.

[127] W. Li, D. Yang, S. D'Addio, and M. Martin-Neira, "Partial interferometric processing of reflected GNSS signals for ocean altimetry," *IEEE Geosci. Remote Sensing Lett.*, vol. 11, no. 9, pp. 1509–1513, Sept. 2014.

[128] A. A. Arroyo, A. Camps, A. Aguasca, G. F. Forte, A. Monerris, C. Rudiger, J. P. Walker, H. Park, D. Pascual, and R. Onrubia, "Dual-polarization GNSS-R interference pattern technique for soil moisture mapping," *IEEE J. Select. Topics Appl. Earth Observ. Remote Sensing*, vol. 7, no. 5, pp. 1533–1544, May 2014.

[129] F. Martin, S. D'Addio, A. Camps, and M. Martin-Neira, "Modeling and analysis of GNSS-R waveforms sample-to-sample correlation," *IEEE J. Select. Topics Appl. Earth Observ. Remote Sensing*, vol. 7, no. 5, pp. 1545–1559, May 2014.

[130] J. L. Garrison, "Modeling and simulation of bin-bin correlations in GNSS-R waveforms," in *Proc. IEEE Int. Geoscience Remote Sensing Symp.*, Munich, Germany, 2012, pp. 7079–7081.

[131] F. Martin, A. Camps, H. Park, S. D'Addio, M. Martin-Neira, and D. Pascual, "Cross-correlation waveform analysis for conventional and interferometric GNSS-R approaches," *IEEE J. Select. Topics Appl. Earth Observ. Remote Sensing*, vol. 7, no. 5, pp. 1560–1572, May 2014.

[132] A. Camps, H. Park, E. Valencia, D. Pascual, F. Martin, A. Rius, S. Ribo, J. Benito, A. Anders-Beivide, P. Saameno, G. Staton, M. Martin-Neira, S. D'Addio, and P. Willemsen, "Optimization and performance analysis of interferometric GNSS-R altimeters: Application to the PARIS IoD Mission," *IEEE J. Select. Topics Appl. Earth Observ. Remote Sensing*, vol. 7, no. 5, pp. 1436–1451, May 2014.

[133] S. Jin and A. Komjathy, "GNSS reflectometry and remote sensing: New objectives and results," *Adv. Space Res.*, vol. 46, pp. 111–117, July 2010.

[134] S. Jin, G. P. Feng, and S. Gleason, "Remote sensing using GNSS signals: Current status and future directions," *Adv. Space Res.*, vol. 47, pp. 1645–1653, 2011.

[135] V. U. Zavorotny and A. G. Voronovich, "Bistatic radar scattering from an ocean surface in the small-slope approximation," in *Proc. IEEE Int. Geoscience Remote Sensing Symp.*, Hamburg, Germany, 1999, pp. 2419–2421.

[136] E. Cardellach, S. Ribó, and A. Rius, "Technical note on POlarimetric phase interferometry (POPI)," CSIC-IEEC, arXiv:physics/0606099v2, June 2006.

[137] E. Cardellach, S. Oliveras, and A. Rius. (2008, June). Applications of the reflected signals found in GNSS radio occultation events. in *Proc. ECMWF/GRAS SAF Workshop Applications GPSRO Measurements*. Reading, U.K. [Online]. Available: http://old.ecmwf.int/publications/library/ecpublications/_pdf/workshop/2008/gras_saf/Cardellach.pdf

[138] K. Boniface, J. M. Aparicio, and E. Cardellach, "Meteorological information in GPS-RO reflected signals," *Atmos. Meas. Tech.*, vol. 4, pp. 1397–1407, July 2011.
[139] G. Ruffini, M. Caparrini, F. Soulat, M. Martin-Neira, P. Silvestrin, and K. Sharman, "Using GNSS reflections for ionospheric studies," in *Proc. Space Weather Workshop: Looking Towards European Space Weather Programme, ESTEC*, Noordwijk, The Netherlands, 2001, pp. 159–168.
[140] J. M. Pallares, G. Ruffini, and L. Ruffini, "Ionospheric tomography using GNSS reflections," *IEEE Trans. Geosci. Remote Sensing*, vol. 43, no. 2, pp. 321–326, Feb. 2005.
[141] G. A. Hajj and C. Zuffada, "Theoretical description of a bistatic system for ocean altimetry using the GPS signal," *Radio Sci.*, vol. 38, no. 5, p. 1089, 2003.
[142] A. Rius, E. Cardellach, and M. Martín-Neira, "Altimetric analysis of the sea-surface GPS-reflected signals," *IEEE Trans. Geosci. Remote Sensing*, vol. 48, no. 4, pp. 2119–2127, 2010.
[143] [Online]. Available: http://www.ice.csic.es/research/gold_rtr_mining/
[144] E. Cardellach, C. O. Ao, M. de la T. Juárez, and G. A. Hajj, "Carrier phase delay altimetry with GPS-reflection/occultation interferometry from low earth orbiters," *Geophys. Res. Lett.*, vol. 31, p. L10402, May 2004.
[145] A. Helm, G. Beyerle, and M. Nitschke. (2004). Detection of coherent reflections with GPS bipath interferometry. [Online]. Available: http://arxiv.org/pdf/physics/0407091v1.pdf
[146] A. M. Semmling, J. Beckheinrich, J. Wickert, G. Beyerle, S. Schön, F. Fabra, H. Pflug, K. He, J. Schwabe, and M. Scheinert, "Sea surface topography retrieved from GNSS reflectometry phase data of the GEOHALO flight mission," *Geophys. Res. Lett.*, vol. 41, no. 3, pp. 954–960, Feb. 2014.
[147] A. M. Semmling, G. Beyerle, R. Stosius, G. Dick, J. Wickert, F. Fabra, E. Cardellach, S. Ribó, A. Rius, A. Helm, S. B. Yudanov, and S. d'Addio, "Detection of Arctic Ocean tides using interferometric GNSS-R signals," *Geophys. Res. Lett.*, vol. 38, no. 4, p. L04103, Feb. 2011.
[148] F. Fabra, E. Cardellach, A. Rius, S. Ribó, S. Oliveras, O. Nogués-Correig, M. B. Rivas, A. M. Semmling, and S. D'Addio,"Phase altimetry with dual polarization GNSS-R over sea ice," *IEEE Trans. Geosci. Remote Sensing*, vol. 50, no. 6, pp. 2112–2121, 2012.
[149] J. S. Löfgren, R. Haas, and J. M. Johansson, "Monitoring coastal sea level using reflected GNSS signals," *Adv. Space Res.*, vol. 47, no. 2, pp. 213–220, 2011.
[150] K. M. Larson, R. D. Ray, F. G. Nievinski, and J. T. Freymueller, "The accidental tide gauge: A GPS reflection case study from kachemak bay, Alaska," *IEEE Geosci. Remote Sens. Lett.*, vol. 10, no. 5, pp. 1200–1204, Sept. 2013.
[151] J. S. Löfgren, R. Haas, and H.-G. Scherneck, "Sea level time series and ocean tide analysis from multipath signals at five GPS sites in different parts of the world," *J. Geodynamics*, vol. 80, pp. 66–80, Oct. 2014.
[152] M. Bevis, S. Businger, T. A. Herring, C. Rocken, R. A. Anthes, and R. H. Ware, "GPS meteorology: Remote sensing of atmospheric water vapor using the Global Positioning System," *J. Geophys. Res.*, vol. 97, pp. 15787–15801, Oct. 1992.
[153] A. R. Thompson, J. M. Moran, and G. W. Swenson, *Interferometry and Synthesis in Radio Astronomy*. New York: Wiley, 1986.
[154] E. R. Kursinski, "The GPS radio occultation concept: Theoretical performance and initial results," Ph.D. dissertation, California Inst. Technol., Long Beach, CA, 1997.
[155] A. Niell, "Global mapping functions for the atmospheric delay at radio wavelengths," *J. Geophys. Res.*, vol. 101, no. B2, pp. 3227–3246, Feb. 1996.
[156] O. J. Sovers and J. L. Fanselow, "Observation model and parameter partials for the JPL VLBI parameter estimation software MASTERFIT-1987," Jet Propulsion Lab. Publication, California Inst. Technol., Pasadena, CA, Tech. Rep. NASA CR-182524, 1987.
[157] J. Park, J. T. Johnson, and S. T. Lowe, "A study of the electromagnetic bias in GNSS-R altimetry," in *Proc. IEEE Int. Geoscience Remote Sensing Symp.*, Québec City, QC, Canada, 2014.
[158] A. Ghavidel, D. Schiavulli, and A. Camps, "A numerical simulator to evaluate the electromagnetic bias in GNSS-R altimetry," in *Proc. IEEE Int. Geoscience Remote Sensing Symp.*, Québec City, QC, Canada, 2014, pp. 4066–4069.
[159] E. Cardellach, T. Peres, R. Castro, N. Catarino, L. Guerriero, and N. Pierdicca. (2014). E-GEM state of the art description document. *Deliverable D4.1 of European FP7 Project E-GEM*. [Online]. Available: www.e-gem.eu
[160] H. Carreño-Luengo, A. Camps, I. Ramos-Perez, and A. Rius, "Experimental evaluation of GNSS-reflectometry altimetric precision using the P(Y) and C/A signals," *IEEE J. Select. Topics Appl. Earth Observ. Remote Sensing*, vol. 7, no. 5, pp. 1493–1500, May 2014.
[161] K. Yu, C. Rizos, and A. Dempster, "GNSS-based model-free sea surface height estimation in unknown sea state scenarios," *IEEE J. Select. Topics Appl. Earth Observ. Remote Sensing*, vol. 7, no. 5, pp. 1424–1435, May 2014.
[162] A. Rius, O. Nogués-Correig, S. Ribó, E. Cardellach, S. Oliveras, E. Valencia, H. Park, J. M. Tarongi, A. Camps, H. van der Marel, R. van Bree, B. Altena, and M. Martin-Neira, "Altimetry with GNSS-R interferometry: First proof of concept experiment," *GPS Solut.*, vol. 16, pp. 231–241, Apr. 2012.
[163] A. M. Semmling, T. Schmidt, J. Wickert, S. Schön, F. Fabra, E. Cardellach, and A. Rius, "On the retrieval of the specular reflection in GNSS carrier observations for ocean altimetry," *Radio Sci.*, vol. 47, p. RS6007, Dec. 2012.
[164] A. M. Semmling, J. Wickert, S. Schön, R. Stosius, M. Markgraf, T. Gerber, M. Ge, and G. Beyerle, "A zeppelin experiment to study airborne altimetry using specular global navigation satellite system reflections," *Radio Sci.*, vol. 48, no. 4, pp. 427–440, 2013.
[165] IOVWST Climate Working Group. (2014, Apr.). Charter for IOVWST climate working group. [Online]. Available: http://coaps.fsu.edu/scatterometry/meeting/docs/2014/ClimateWorkingGroup/OVWST%20Climate%20Working%20Group%20Charter_Apr14.pdf
[166] (2014, May). IOVWST Wind Stress Working Group. [Online]. Available: http://coaps.fsu.edu/scatterometry/meeting/docs/2014/Stress/OVWST%20Wind%20Stress%20Working%20Group%20Charter_May29.pdf
[167] E. Cardellach, G. Ruffini, D. Pino, A. Rius, A. Komjathy, and J. L. Garrison, "Mediterranean balloon experiment: Ocean wind speed sensing from the stratosphere using GPS reflections," *Remote Sensing Environ.*, vol. 88, no. 3, pp. 351–362, 2003.
[168] O. Germain, G. Ruffini, F. Soulat, M. Caparrini, B. Chapron, and P. Silvestrin, "The eddy experiment: GNSSR speculometry for directional sea roughness retrieval from low altitude aircraft," *Geophys. Res. Lett.*, vol. 31, p. L21307, 2004.
[169] J. Marchan-Hernandez, N. Rodriguez-Alvarez, A. Camps, X. Bosch-Lluis, I. Ramos-Perez, and E. Valencia, "Correction of the sea state impact on the L-band brightness temperature by means of delay-Doppler maps of global navigation satellite signals reflected over the sea surface," *IEEE Trans. Geosci. Remote Sensing*, vol. 46, no. 10, pp. 2914–2923, 2008.
[170] E. Valencia, J. F. Marchan-Hernandez, A. Camps, N. Rodriguez-Alvarez, J. M. Tarongi, M. Piles, I. Ramos-Perez, X. Bosch-Lluis, M. Vall-llossera, and P. Ferre, "Experimental relationship between the sea brightness temperature changes and the GNSS-R delay-Doppler maps: Preliminary results of the albatross field experiments," in *Proc. IEEE Int. Geoscience Remote Sensing Symp.*, Cape Town, South Africa, 2009, pp. III-741–III-744.
[171] A. Camps, J. F. Marchan, E. Valencia, I. Ramos, X. Bosch-Lluis, N. Rodriguez, H. Park, A. Alcayde, A. Mollfulleda, J. Galindo,

P. Martinez, S. Chavero, M. Angulo, and A. Rius, "PAU instrument aboard INTA MicroSat-1: A GNSS-R demonstration mission for sea state correction in L-band radiometry," in *Proc. IEEE Int. Geoscience Remote Sensing Symp.*, Vancouver, BC, Canada, 2011, pp. 4126–4129.

[172] E. Valencia, A. Camps, X. Bosch-Lluis, N. Rodriguez-Alvarez, I. Ramos-Perez, F. Eugenio, and J. Marcello, "On the use of GNSS-R data to correct L-band brightness temperatures for sea-state effects: Results of the ALBATROSS field experiments," *IEEE Trans. Geosci. Remote Sensing*, vol. 49, no. 9, pp. 3225–3235, Sept. 2011.

[173] C. Zuffada, T. Elfouhaily, and S. Lowe, "Sensitivity analysis of wind vector measurements from ocean reflected GPS signals," *Remote Sens. Environ.*, vol. 88, no. 3, pp. 341–350, 2003.

[174] T. Elfouhaily, D. R. Thompson, and L. Linstrom, "Delay-Doppler analysis of bistatically reflected signals from the ocean surface: Theory and application," *IEEE Trans. Geosci. Remote Sensing*, vol. 40, no. 3, pp. 560–573, 2002.

[175] A. Camps, M. Caparrini, R. Sabia, and G. Ruffini, "Sea surface salinity retrieval from space: Potential synergetic use of GNSS-R signals to improve the sea state correction and application to the SMOS mission," in *Proc. IEEE Microwave Radiometry Remote Sensing Environment (MicroRad)*, San Juan, Puerto Rico, 2006.

[176] N. Rodriguez-Alvarez, D. M. Akos, V. U. Zavorotny, J. A. Smith, A. Camps, and C. W. Fairall, "Airborne GNSS-R wind retrievals using delay-Doppler maps," *IEEE Trans. Geosci. Remote Sensing*, vol. 51, no. 1, pp. 626–641, Jan. 2013.

[177] E. Valencia, V. U. Zavorotny, D. M. Akos, and A. Camps, "Using DDM asymmetry metrics for wind direction retrieval from GPS ocean-scattered signals in airborne experiments," *IEEE Trans. Geosci. Remote Sensing*, vol. 52, no. 7, pp. 3924–3936, 2014.

[178] O. Nogués-Correig, E. C. Galí, J. S. Campderrós, and A. Rius, "A GPS-reflections receiver that computes Doppler/delay maps in real time," *IEEE Trans. Geosci. Remote Sensing*, vol. 45, no. 1, pp. 156–174, 2007.

[179] G. Schiavulli, D. Nunziata, F. Pugliano, and M. Migliaccio, "Reconstruction of the normalized radar cross section field from GNSS-R delay-Doppler map," *IEEE J. Select. Topics Appl. Earth Observ. Remote Sensing*, vol. 7, no. 5, pp. 1573–1583, May 2014.

[180] E. Cardellach, (2002). Sea surface determination using GNSS reflected signals. Ph.D. dissertation. Univ. Politècnica de Catalunya. Barcelona, Spain. [Online]. Available: https://www.ice.csic.es/files/estel/Cardellach_PhD.pdf

[181] F. Soulat, M. Caparrini, O. Germain, P. Lopez-Dekker, M. Taani, and G. Ruffini, "Sea state monitoring using coastal GNSS-R," *Geophys. Res. Lett.*, vol. 31, p. L21303, June 2004.

[182] E. Valencia, A. Camps, J. F. Marchan-Hernandez, N. Rodriguez-Alvarez, I. Ramos-Perez, and X. Bosch-Lluis, "Experimental determination of the sea correlation time using GNSS-R coherent data," *IEEE Geosci. Remote Sensing Lett.*, vol. 7, no. 4, pp. 675–679, 2010.

[183] S. J. Katzberg, J. Dunion, and G. Ganoe, "The use of reflected GPS signals to retrieve ocean surface wind speed in tropical cyclones," *Radio Sci.*, vol. 48, no. 4, pp. 371–387, July/Aug. 2013

[184] P. Ferrazzoli, L. Guerriero, and D. Solimini, "Simulating bistatic scatter from surfaces covered with vegetation," *J. Electromagn. Waves Applicat.*, vol. 14, no. 2, pp. 233–248, 1995.

[185] A. Kavak, G. Xu, and W. J. Vogel, "GPS multipath fade measurements to determine L-band ground reflectivity properties," in *Proc. 20th NASA Propagation Experimenters Meeting*, 1996.

[186] A. Kavak, W. J. Vogel, and G. Xu, "Using GPS to measure ground complex permittivity," *Electron. Lett.*, vol. 34, no. 3, pp. 254–255, Feb. 1998.

[187] V. U. Zavorotny and A. G. Voronovich, "Bistatic GPS signal reflections at various polarizations from rough land surface with moisture content," in *Proc. IEEE Int. Geoscience Remote Sensing Symp.*, Honolulu, HI, 2000, vol. 7, pp. 2852–2854.

[188] A. Egido, M. Caparrini, G. Ruffini, S. Paloscia, E. Santi, L. Guerriero, N. Pierdicca, and N. Floury, "Global Navigation Satellite Systems reflectometry as a remote sensing tool for agriculture," *Remote Sensing*, vol. 4, no. 8, pp. 2356–2372, 2012.

[189] A. Egido, S. Paloscia, E. Motte, L. Guerriero, N. Pierdicca, M. Caparrini, E. Santi, G. Fontanelli, and N. Floury, "Airborne GNSS-R soil moisture and above ground biomass observations," *IEEE J. Select. Topics Appl. Earth Observ. Remote Sensing*, vol. 7, no. 5, pp. 1522–1532, May 2014.

[190] N. Rodriguez-Alvarez, X. Bosch-Lluis, A. Camps, M. Vall-llossera, E. Valencia, J. F. Marchan-Hernandez, and I. Ramos-Perez, "Soil moisture retrieval using GNSS-R techniques: Experimental results over a bare soil field," *IEEE Trans. Geosci. Remote Sensing*, vol. 47, no. 11, pp. 3616–3624, Nov. 2009.

[191] [Online]. Available: http://xenon.colorado.edu/portal/

[192] K. M. Larson, E. E. Small, J. J. Braun, and V. U. Zavorotny, "Environmental sensing: A revolution in GNSS applications," *Inside GNSS*, vol. 9, no. 4, pp. 36–46, July/Aug. 2014.

[193] E. D. Gutmann, K. M. Larson, M. W. Williams, F. G. Nievinski, and V. Zavorotny, "Snow measurement by GPS interferometric reflectometry: An evaluation at Niwot Ridge, Colorado," *Hydrol. Process.*, vol. 26, pp. 2951–2961, Sept. 2012.

[194] M. D. Jacobson, "Inferring snow water equivalent for a snow-covered ground reflector using GPS multipath signals," *Remote Sensing*, vol. 2, no. 10, pp. 2426–2441, 2010.

[195] M. D. Jacobson, "Snow-covered lake ice in GPS multipath reception—Theory and measurement," *Adv. Space Res.*, vol. 46, no. 2, pp. 221–227, 2010.

[196] K. M. Larson and F. G. Nievinski, "GPS snow sensing: Results from the EarthScope plate boundary observatory," *GPS Solut.*, vol. 17, no. 1, pp. 41–52, Jan. 2013.

[197] F. G. Nievinski and K. M. Larson, "Inverse Modeling of GPS multipath for snow depth estimation—Part I: Formulation and simulations," *IEEE Trans. Geosci. Remote Sensing*, vol. 52, no. 10, pp. 6555–6563, Oct. 2014.

[198] F. G. Nievinski and K. M. Larson, "Inverse modeling of GPS multipath for snow depth estimation—Part II: Application and validation," *IEEE Trans. Geosci. Remote Sensing*, vol. 52, no. 10, pp. 6564–6573, Oct. 2014.

[199] N. Rodriguez-Alvarez, A. Aguasca, E. Valencia, X. Bosch-Lluis, A. Camps, I. Ramos-Perez, H. Park, and M. Vall-llossera, "Snow thickness monitoring using GNSS measurements," *IEEE Geosci. Remote Sensing Lett.*, vol. 9, no. 6, pp. 1109–1113, Nov. 2012.

[200] F. Fabra, "GNSS-R as a source of opportunity for remote sensing of the cryosphere," Ph.D. dissertation, Univ. Politècnica de Catalunya, Barcelona, Spain, 2013.

[201] F. Nievinski and K. Larson, "Forward modeling of GPS multipath for near-surface reflectometry and positioning applications," *GPS Solut.*, vol. 18, no. 2, pp. 309–322, 2014.

[202] F. Nievinski and K. Larson, "An open source GPS multipath simulator in Matlab/Octave," *GPS Solut.*, vol. 18, pp. 473–481, 2014.

***GRS***